Vapor Synthesis and Thermal Evolution of Supportless, Metal Nanotubes and Application as Electrocatalysts

A Dissertation Presented for the
Doctor of Philosophy
Degree
The University of Tennessee, Knoxville

Robert William Atkinson
August 2015

Copyright © 2015 by Robert William Atkinson.

All rights reserved.

ACKNOWLEDGMENTS

I would first like to thank Dr. Thomas Zawodzinski for providing me with such a great opportunity to work in this research group. I would like to thank my co-advisor, Dr. Alex Papandrew, for the knowledge that he has shared with me about materials science and electrochemistry, for the example that he has set as a driven researcher, for helping me to mature as a scientist, and for constantly challenging me. Dr. Papandrew has been a better resource for my career than I could have ever imagined and I will forever be grateful for his guidance. I would like to thank my committee members, Dr. Siris Laursen and Dr. Craig Barnes, for their suggestions and advice on my research and my presentation of it. I would also like to thank Dr. Gabriel Goenaga and Dr. Samuel St. John for their assistance with my work and for their support. For the last five years I have been surrounded by a supportive and encouraging group of labmates and friends that have positively influenced this work and my development as a researcher. I would not be where I am today without the love and support of my parents, Will and Sandy, my sister, Caroline, and Meaghan Ramos.

I thank the TN-SCORE program of the National Science Foundation for their financial support of this work (EPS-1004083). Use of the National Synchrotron Light Source, Brookhaven National Laboratory, was supported by the U.S. Department of Energy, Office of Science, Office of Basic Energy Sciences, under Contract No. DE-AC02-98CH10886. This research also used

resources of the Advanced Photon Source, a U.S. Department of Energy (DOE) Office of Science User Facility operated for the DOE Office of Science by Argonne National Laboratory under Contract No. DE-AC02-06CH11357. A portion of this research was conducted as part of a user proposal at the Center for Nanophase Materials Sciences (CNMS), which is sponsored at Oak Ridge National Laboratory by the Scientific User Facilities Division, Office of Basic Energy Sciences, U.S. Department of Energy. I thank Dr. Raymond R. Unocic and Dr. Kinga A. Unocic for microscopy done at CNMS. I thank Dr. Gabriel M. Veith for assistance with XPS experiments, which were supported by the U.S. Department of Energy (DOE), Basic Energy Sciences (BES), Materials Sciences and Engineering Division. I also thank Dr. Ondrej Dyck (UTK) for collecting TEM images.

ABSTRACT

One of the major limitations of proton exchange membrane fuel cells (PEMFCs) is the high cost and poor durability of the currently preferred catalyst design, small Pt nanoparticles supported on high surface area carbon (Pt/C). Unsupported, high-aspect ratio nanostructured catalysts, or extended surface catalysts, are a promising paradigm as electrocatalysts for a number of electrochemical reactions. These extended surface catalysts generally exhibit higher specific activities compared to carbon-supported nanoparticle counterparts that have been ascribed to the unique electronic, surface and structural properties of these materials. Extended surface catalysts frequently maintain enhanced durability over supported catalysts during fuel cell operation because these materials are not susceptible to the same modes of degradation inherent to small supported nanoparticles.

Considering the promise of extended surfaces as catalysts, we have synthesized metallic, mixed-phase, and alloyed bimetallic nanotubes by a chemical vapor deposition (CVD) technique to catalyze a number of reactions relevant for fuel cells. In this CVD process, metalorganic precursors, namely metal-acetylacetonates, are decomposed by a mild thermal treatment and deposited as conformal nanoparticulate layers within a sacrificial anodic alumina template. Following vapor deposition, the nanotube samples may be annealed while still in the template to induce a series of changes with implications on

electrocatalysis, including porosity, alloying, and increases in surface coordination. The metallic nanotubes prepared by this method are highly active catalysts for a host of electrochemical reactions that are promising for fuel cell applications. The effects of composition, heat treatment temperature and gas environment on the activity and durability of these materials have been studied for oxygen reduction, methanol oxidation, formic acid oxidation, and hydrogen oxidation.

PREFACE

My co-advisors, Dr. Zawodzinski and Dr. Papandrew, who have backgrounds in electrochemistry and materials science, have had major influence on this dissertation. As a result, the terminology and nomenclature found within this work may be native to one of these fields. Additionally, there may be other misleading instances of shorthand resulting from this. For example, the bulk alloy composition of a nanotube is described herein as $Pt_xRu_{(1-x)}NT$. In this case, the subscripts are used to describe the alloy composition.

TABLE OF CONTENTS

Chapter 1 Introduction 1

Proton Exchange Membrane Fuel Cells 2

Alkaline Anion Exchange Membrane Fuel Cells 3

Fuel Cell Electrocatalysts 4

Nanostructured Electrocatalysts and the Motivation for Restricting Size to the Nanoscale 5

Extended Surface Catalysts: Durability and Specific Activity Enhancements 7

Extended Surface Catalysts: Platinum Group Metal Nanotubes 10

Modified Chemical Vapor Deposition for the Development of Platinum Group Metal Nanotubes 11

Optional Thermal Annealing Process for Structural and Chemical Evolutions 13

Structural Changes in Annealed Nanotubes: Grain Growth 14

Structural Changes in Annealed Nanotubes: Alloy Formation 17

Structural Changes in Annealed Nanotubes: Chemical Phase Transition ... 18

Chapter 2 Oxygen Reduction Activity of Vapor-Grown Platinum Nanotubes 19

Abstract 20

Introduction 21

Experimental 23

Results and Discussion 26
Conclusion 40
Chapter 3 Vapor Synthesis and Thermal Modification of Supportless Platinum-Ruthenium Nanotubes and Application as Methanol Electrooxidation Catalysts 42
Abstract 43
Introduction 44
Experimental 49
Results and Discussion 54
Conclusion 80
Chapter 4 Supportless, Bismuth-Modified Palladium Nanotubes with Improved Activity and Stability for Formic Acid Oxidation 82
Abstract 83
Introduction 83
Experimental 87
Results and Discussion 91
Conclusion 116
Chapter 5 Platinum and Palladium Overlayers Dramatically Enhance the Activity of Ruthenium Nanotubes for Alkaline Hydrogen Oxidation 119
Abstract 120
Introduction 120
Experimental 124

Results and Discussion 127
Conclusion 157
Chapter 6 Computational Framework for Calculating Hamaker Coefficients and Interaction Energies for Fuel Cell Electrode Materials 158
Abstract 159
Introduction 159
Experimental Measurements of Optical Properties for Calculating Hamaker Coefficients 160
Computational Methods 162
Results and Discussion 171
Suggested Future Work 174
Chapter 7 Conclusion 177
References 183
Appendix 202
Vita 207

LIST OF TABLES

Table 2.1. Lattice Parameter, a, and Crystallite Size, L, of Platinum Nanotubes Before and After Annealing. 29

Table 2.2. ORR activity at 0.9 V and electrochemical surface area for PtNTs and baseline samples in ionomer-free electrodes. Measured in 0.1 M $HClO_4$ at room temperature and corrected to 100 kPa oxygen partial pressure. 33

Table 3.1. Location of Pt(111) peak, crystallite size (L) measured by Scherrer analysis of the Pt(111) peak, electrode loading, electrochemical surface area (ECSA), MOR Mass and Specific Activities and MOR Pt mass and Pt specific activities at 0.65 V vs. RHE. 76

Table 4.1**.** Location of Pd(111) peak, grain size (L) measured by Scherrer analysis of the Pd(111) peak, electrode loading, electrochemical surface area (ECSA), and FAO Mass and Specific Activities at 0.3 V vs. RHE. 103

Table 5.1. Scherrer analysis of all Ru hcp peaks of the X-ray diffraction patterns for pure RuNT, PtRuNTs and PdRuNTs annealed at 500°C in 4% H_2 133

Table 5.2. EXAFS fits for PtRuNTs, PdRuNTs and monometallic nanotube controls. 139

Table 5.3. Performance characteristics for HOR electrochemical analyses. Parameters based off of kinetic currents were not able to be determined for the Ru nanotube because it did not reach the mass transport limited current density 148

Table 6.1. Comparison of measured Hamaker coefficients with literature values for common material standards. 171

LIST OF FIGURES

Figure 2.1. SEM micrographs of (a) Pt nanotubes as-synthesized and (b) after annealing in flowing N_2 at 500°C. 27

Figure 2.2. TEM micrographs of Pt nanotubes (a) as-synthesized and (b) after annealing in flowing N_2 at 500°C. Selected-area diffraction patterns for each sample are inset. 28

Figure 2.3. Cu Kα x-ray diffraction patterns of (a) as-synthesized PtNTs and (b) PtNTs annealed in flowing N_2 at 500°C. 30

Figure 2.4. Representative cyclic voltammograms for the (a) Nafion-free Pt/HSC control electrode and (b) Nafion-free annealed, porous PtNTs recorded at 25°C and 20 mV/s in 0.1 M $HClO_4$. (c) Shows the current density of (b) multiplied by a factor of 10 to emphasize the features in the voltammogram. 32

Figure 2.5. Representative Tafel plots for the (a) Nafion-free Pt/HSC control electrode and (b) Nafion-free annealed, porous PtNTs recorded at 25°C, 20 mV/s and 1600 rpm electrode rotation rate in 0.1 M $HClO_4$. 34

Figure 2.6. Summary of experiments conducted at 25°C in 0.1 M $HClO_4$ to determine specific activity and mass activity of porous PtNTs annealed at 500°C.....36

Figure 2.7. Rotating disc electrode cyclic voltammograms of annealed PtNTs recorded at 20 mV/s in 0.1 M HClO4 at 25°C at regular intervals during

cycling from 0.6 V to 1.0 V at 50 mV/s. Inset shows ECA plotted against cycle number. 37

Figure 2.8. The effects of Nafion addition on specific activity and ECA of porous PtNTs annealed at 500°C. 39

Figure 3.1. SEM images of as-synthesized $PtRu(O_xH_y)$NTs (a) 10% Pt, (b) 17% Pt, (c) 38% Pt, (d) 64% Pt, and PtRuNTs annealed at 750°C in 4% H_2 (e) 9% Pt, (f) 20% Pt, (g) 47% Pt, (h) 60% Pt. 55

Figure 3.2. HAADF STEM and EDS elemental mapping of (a-f) as-synthesized $Pt_{58}Ru_{42}(O_xH_y)$NTs and (g-l) annealed, alloyed $Pt_{58}Ru_{42}$NTs at 750ºC in 4% H_2 for 1 hour. Cross sections were observed by leaving the nanotubes embedded within the sacrificial AAO template. 57

Figure 3.3. TEM images of the (a-b) as-synthesized $Pt_{58}Ru_{42}(O_xH_y)$NTs showing the amorphous $Ru(O_xH_y)$ layer on nanocrystalline Pt lining the Al_2O_3 pore walls. FFT analysis from the boxed regions in (b) correspond to (c) amorphous $Ru(O_xH_y)$ and (d) crystalline Pt. The TEM images in (e-f) are from the annealed $Pt_{58}Ru_{42}$NTs and show PtRu nanocrystals. FFT analyses from the boxed regions in (f) correspond to (g) a PtRu crystal oriented along the [011] zone-axis and (h) (111) lattice planes. 59

Figure 3.4. Cu Kα X-ray diffraction patterns of as-synthesized (a) $Pt_{64}Ru_{36}(O_xH_y)$NT, annealed (b) $Pt_{60}Ru_{40}O_x$NT at 750°C in N_2, and annealed

at 750°C in H_2 (c) PtNT, (d) $Pt_{80}Ru_{20}$NT, (e) $Pt_{64}Ru_{36}$NT, (f) $Pt_{60}Ru_{40}$NT, (g) $Pt_{43}Ru_{57}$NT, (h) $Pt_{38}Ru_{62}$NT, (i) Pt_7Ru_{93}NT, (j) RuNT. 61

Figure 3.5. Cu Kα X-ray diffraction patterns of as-synthesized Ru(O_xH_y)NTs and as-synthesized PtRu(O_xH_y)NTs with variable Pt content. 63

Figure 3.6. High resolution XPS spectra of the Pt 4f doublet (a-c) and the Ru $3p_{3/2}$ peak (d-f) for (a, d) 750°C, 4% H_2-annealed $Pt_{59}Ru_{41}$NTs (b, e) as-synthesized $Pt_{59}Ru_{41}(O_xH_y)$NTs, and (c, f) PtRu black. 65

Figure 3.7. XANES data at the Ru K edge of selected synthesis products and commercial PtRu black. 67

Figure 3.8. Cyclic voltammograms recorded in 0.5 M H_2SO_4 at 20 mV s^{-1}. In (A), pure and metallic RuNTs (dashed black line) which are reduced at 750°C in 4% H_2 are compared to as-synthesized PtRu(O_xH_y)NTs with variable Pt content. In (B), as-synthesized (a) PtRu(O_xH_y)NTs, (b) 750°C N_2-annealed $PtRuO_2$NTs, and (c) 750°C, 4% H_2-annealed PtRuNTs with similar Pt content are compared. 70

Figure 3.9. Scatter plot of specific activity vs. Pt content measured at 0.65 V vs. RHE for as-synthesized PtRu(O_xH_y)NTs (red squares) and alloyed PtRuNTs (black circles) recorded in 0.5 M CH_3OH and 0.1 M H_2SO_4. 71

Figure 3.10. CO stripping voltammograms recorded in 0.5 M H_2SO_4 at 20 mV s^{-1} normalized to (A) total electrode mass and (B) ECSA. CO was adsorbed at 0.1 V vs. RHE. 74

Figure 3.11. Linear sweep voltammograms recorded in 0.5 M CH_3OH and 0.1 M H_2SO_4 at 20 mV s^{-1}. Voltammograms are normalized to (A) total electrode mass and (B) ECSA.....78

Figure 4.1**.** HAADF STEM and EDS elemental mapping of the templated (a-d) as-synthesized PdNTs and (e-h) PdNTs annealed at 500°C.....91

Figure 4.2**.** High-resolution transmission electron microscopy (HRTEM) images of PdNTs (a,b) as-synthesized and after heat treatments in 4% H_2 for 1 hr at (c,d) 300°C, (e,f) 400°C, and (g,h) 500°C. FFT analysis from the boxed region in (h) corresponds to crystalline, FCC Pd oriented along the [110] zone axis.....93

Figure 4.3**.** Scanning electron microscopy (SEM) images of PdNTs (a) as-synthesized and after heat treatments in 4% H_2 for 1 hr at (b) 300°C, (c) 400°C, and (d) 500°C. Increases in grain size are observed with increasing heat treatment temperature. Grain size estimates are provided in the text using XRD data.....95

Figure 4.4**.** Cu Kα X-ray diffraction patterns for as-synthesized PdNTs and after annealing in 4% H_2 at 300°C, 400°C and 500°C for 1 hour. Dashed line corresponds to Pd(111) peak (PDF: 00-005-0681).....97

Figure 4.5**.** (A) Normalized XANES patterns for the as-synthesized and heat-treated PdNT samples, as well as commercial Pd/C compared to foil at the Pd K edge. (B) Forward Fourier transforms of the EXAFS at the Pd K edge.

Gray line indicates Pd-Pd radial position. The lattice expansion due to carbon absorption in the as-synthesized sample is reflected in EXAFS as a shift to larger Pd-Pd radial position. The shift in the Pd peak of the commercial Pd/C to lower radial position reflects its high degree of oxidation and the smaller atomic size of Pd^{2+} (here observed as PdO).[175] 99

Figure 4.6**.** (A) Baseline cyclic voltammograms and (B) CO stripping voltammograms recorded in 0.5 M H_2SO_4 for the PdNTs annealed at (a) 300°C, (b) 400°C, (c) 500°C, (d) 500°C with 80% Bi surface coverage (Bi~PdNT), and (e) carbon-supported Pd. The inset in (A) highlights the Pd oxide reduction region. The inset in (B) magnifies the CO stripping peaks. 101

Figure 4.7**.** Area-normalized cyclic voltammograms recorded at 20 mV/s in 0.5 M H_2SO_4 and 0.5 M HCOOH for (a) PdNTs annealed at 500°C prior to Bi coverage, and with (b) 42% Bi and (c) 80% Bi coverage. Voltammograms are normalized to available Pd area. Labels point to forward scans of voltammograms. The inset plots the potential of the peak current in the anodic scan as a function of Bi coverage. 105

Figure 4.8**.** Scatter plot of specific activity of PdNTs as a function of their surface Bi coverage (in percent). The specific activity is reported at 0.3 V vs. RHE from voltammograms recorded in 0.5 M H_2SO_4 and 0.5 M HCOOH at 20 mV/s. The orange dashed line corresponds to the specific activity of

unmodified, 500°C PdNTs and the gray dash-dot line represents the specific activity of Pd/C, both also reported at 0.3 V vs. RHE. Specific activity is normalized to available Pd area.....107

Figure 4.9. Scatter plot of mass activity of PdNTs as a function of their surface Bi coverage (in percent). The mass activity is reported at 0.3 V vs. RHE from voltammograms recorded in 0.5 M H_2SO_4 and 0.5 M HCOOH at 20 mV/s. The blue dashed line corresponds to the mass activity of Bi-free, 500°C PdNTs and the gray dash-dot line represents the specific activity of Pd/C, both also reported at 0.3 V vs. RHE. 109

Figure 4.10. Area-normalized cyclic voltammograms recorded at 20 mV/s in 0.5 M H_2SO_4 and 0.5 M HCOOH for (a) commercial, carbon-supported Pd (20 wt% Pd), PdNTs annealed at (b) 300°C, (c) 400°C, (d) 500°C, and (e) Bi-decorated PdNTs annealed at 500°C. Voltammograms are normalized to available Pd area. Labels point to anodic scans of voltammograms.....111

Figure 4.11. Chronoamperometric hold at 0.2 V vs. RHE in 0.1 M $HClO_4$ and 1.0 M HCOOH without rotation. The current is normalized by the sample ECSA, which refers to available Pd. 113

Figure 4.12. Cyclic voltammograms recorded in 0.1 M $HClO_4$ electrolyte at 20 mV/s for (A) Bi-modified PdNTs (80% Bi), (B) 500°C PdNT, and (C) Pd/C immediately before and after a 24 hour chronoamperometric hold at 0.2 V in 0.1 M $HClO_4$ and 1.0 M HCOOH. 115

Figure 5.1. Synthesis scheme illustrating the sequence of precursor deposition used to make bi-metallic nanotubes. Following the annealing, the nanotubes are separated from the template in 30% KOH, then analyzed using microscopic, spectroscopic, and electrochemical techniques. 123

Figure 5.2. HAADF S/TEM and EDS map images of FIB cross-sections of (top) PtRuNTs (19% Pt) and (bottom) PdRuNTs (22% Pd) in the anodic alumina template. 128

Figure 5.3. SEM images of PtRuNTs with (a) 4% Pt, (b) 7% Pt, (c) 10% Pt, and (d) 19% Pt, and PdRuNTs with (e) 7.5% Pd, (f) 18% Pd, (g) 19% Pd, and (h) 22% Pd after heat treatment. 129

Figure 5.4. SEM images of the monometallic nanotubes used as controls: (a) PtNT, (b) RuNT, (c) PdNT. All samples are annealed at 500°C in 4% H_2. . 130

Figure 5.5. Cu Kα XRD patterns for the (a) PtRuNTs and (b) PdRuNTs with reference spectra for the monometallic RuNT, PtNT, and PdNT included. Above the respective spectra, the nominal composition is reported on the left while composition determined using Vegard's law is given on the right. Pure metal peak positions with relative intensities (gray sticks) are included for reference (Ru: PDF 00-006-0663; Pt: PDF 00-004-0802; Pd: PDF 00-005-0681). 131

Figure 5.6. Normalized XANES spectra for the PtRuNTs (a,c,e) and PdRuNTs (b,d,f) nanotubes at the Ru K (a-b), Pt L_3, (c, e) and Pd K (d, f) edges. Gray

lines (dashed) in (c) and (d) are to guide the eye to the center of the white line peak. Data for the reference foils (black •••) and the respective pure metal nanotubes (red) are included in each figure for comparison. Key: $Ru_{0.93}Pt_{0.07}$ (orange), $Ru_{0.87}Pt_{0.13}$ (green), $Ru_{0.69}Pt_{0.31}$ (blue); $Ru_{0.93}Pd_{0.07}$ (orange), $Ru_{0.85}Pd_{0.15}$ (green), $Ru_{0.80}Pd_{0.20}$ (blue), $Ru_{0.77}Pd_{0.23}$ (violet). Gray arrows indicate increasing Pt (e) or Pd (f) composition and increased peak broadening in the enlarged pre-edge XANES spectra for the Pt L_3 and Pd K edges, respectively. 135

Figure 5.7. Forward Fourier transforms of the EXAFS for the PtRuNTs (a,c) and PdRuNTs (b,d) at the Ru K (a-b), Pt L_3, (c) and Pd K (d) edges. Data for the reference foils (black •••) and the respective pure metal nanotubes (red) are included in each figure for comparison. The gray guides in (a, b, d) are guides to the center of the first-shell scattering path. The transform magnitude related to the 2 paths present in (c) are indicated by the gray guides. Key: $Ru_{0.93}Pt_{0.07}$ (orange), $Ru_{0.87}Pt_{0.13}$ (green), $Ru_{0.69}Pt_{0.31}$ (blue); $Ru_{0.93}Pd_{0.07}$ (orange), $Ru_{0.85}Pd_{0.15}$ (green), $Ru_{0.80}Pd_{0.20}$ (blue), $Ru_{0.77}Pd_{0.23}$ (violet). 137

Figure 5.8. k^2-weighted EXAFS at the Pt L3 edge for the Pt foil (a) and the PtRu nanotubes (b-d). The data (black •••) and the fits (red) are represented. The same ordinate limits have been used for all plots to demonstrate the relative scattering amplitude in the EXAFS region for the nanotubes vs. foil. 138

Figure 5.9. Electrochemical data collected in static, N_2-saturated, 0.1M KOH at 50 mV/s for the (a) PtRuNTs and (b) PdRuNTs. Charging currents indicate a composition-dependent reduction in the double-layer charging current for the PtRuNTs and a shift of the surface oxide reduction peak for both the PtRuNTs and the PdRuNTs. Key: a) RuNT (black), PtNT (red), $Pt_{0.04}Ru_{0.96}$NT (green), $Pt_{0.07}Ru_{0.93}$NT (blue), $Pt_{0.10}Ru_{0.90}$NT (purple), $Pt_{0.19}Ru_{0.81}$NT (magenta); b) RuNT (black), PdNT (red), $Pd_{0.07}Ru_{0.93}$NT (green), $Pd_{0.15}Ru_{0.85}$NT (blue), $Pd_{0.20}Ru_{0.80}$NT (purple), $Pd_{0.23}Ru_{0.77}$NT (magenta). 141

Figure 5.10. Positive-going scans in H_2-saturated, 0.1M KOH at 1600 rpm and at 10 mV/s (c-d) for the (a) PtRuNTs and (b) PdRuNTs. HOR performance of PtRuNTs and PdRuNTs are enhanced in comparison to pure Pt, Pd, or Ru nanotubes and approach the mass-transport-limited current.....143

Figure 5.11. HOR specific activity of the various experimental nanotube samples. The Pt (or Pd) monolayer thickness is given on the bars for the bi-metallic nanotubes. There are significant improvements in specific activity vs. the constituent monometallic nanotubes, and the optimum performance is achieved at ~0.5-0.8 overlayer coverage for the PdRuNTs and the PtRuNTs. 145

Figure 5.12. Tafel slope analysis for HOR/HER in H_2-saturated, 0.1M KOH obtained at 10 mV/s and 1600 rpm for (a) PtRuNTs and (b) PdRuNTs.

Butler-Volmer equation fits (solid) to the kinetic currents (symbols) are illustrated for the samples indicated in the legends. 147

Figure 5.13. Schematic of Pt atoms (green) on Ru atoms (blue) comprising a PtRuNT showing active sites composed only of Pt atoms (left), as well as active sites of both Pt and Ru atoms (right). Electronic effects from the subsurface Ru reduce H-binding energy on both surfaces. On Pt atoms with adjacent OH, the electron transfer step is faster and the bi-functional active site clears the Pt atoms for slower H_2 dissociative adsorption (Tafel rds)..150

Figure 5.14. Electrochemical oxygen reduction data collected in O_2-saturated electrolyte at 1600 rpm and 10 mV/s. Oxygen reduction currents have been normalized to the transport limited currents and comparisons have been made using the respective half-wave potentials (dotted). 154

Figure 5.15. HOR exchange current density with respect to the half-wave potential for ORR in O_2-saturated, 0.1M KOH for the RuNT (square), PdRuNTs (diamond), PtRuNTs(circle), and the PtNT (plus). Dashed guides are for the eye only. The *d*-band center scale was determined using calculated values for the monometallic RuNTs and PtNTs.[226] Interpolated *d*-band centers are similar to calculated values for fractional overlayers of Pt or Pd on Ru (see text). Pd samples that formed Pd-H during HOR (as determined by the ~0.25 anodic transfer coefficient) exhibited an unusually

low activity because of hydride formation[54] and have been left off of the chart for clarity. 156

Figure 6.1. Illustration of the geometry described in equation 7.15: an interacting sphere and cylinder. 168

Figure 6.2. Illustration of geometry modeled by Equation 6.16: two infinite, parallel cylinders. 169

Figure 6.3. Illustration of the interaction system geometry modeled by Equations 6.18 and 6.19: perpendicular cylinders with equal radii. 170

Figure 6.4. Hamaker coefficients (H) and interaction energies (U) as a function of separation distance across water between the centers of two spheres of identical material: TKK Pt black (blue) and PtNTs (red). Thermal energy units are used for the Hamaker coefficient (H, right axis) and interaction energy (U, left axis) for compactness; kT_{room}=1.3807 x 10^{23}(J/K) x 293.15 K = 4.05 zJ, where 1 zJ = 10^{-21} J. 172

Figure A.1. Linear sweep voltammograms recorded in 0.5 M CH_3OH and 0.1 M H_2SO_4 at 20 mV s^{-1}. 203

Figure A.2. TGA profiles as a function of temperature ramp rate of platinum(II)-2,4-pentanedionate, Pt-$(acac)_2$. 204

Figure A.3. TGA profiles as a function of temperature ramp rate of palladium(II)-2,4-pentanedionate, Pd-$(acac)_2$. 205

Figure A.4. TGA profiles as a function of temperature ramp rate of ruthenium(III)-2,4-pentanedionate, Ru-(acac)$_3$. 206

CHAPTER 1

INTRODUCTION

Proton Exchange Membrane Fuel Cells

Proton exchange membrane fuel cells (PEMFCs) are electrochemical devices that have long been considered a promising technology for the generation of clean, renewable energy, particularly for portable and automotive applications, because the devices are capable of electrochemically converting the energy stored in fuels into electrical energy with high efficiency.[1–4] Unlike the internal combustion engines presently used to power most automobiles, fuel cell efficiency is not limited by the Carnot cycle and these electrochemical devices do not produce emissions that are harmful to the environment.[4] Considering also that hydrogen fuels may be obtained from renewable sources, PEMFCs are highly attractive power sources for automotive and portable applications.[1] However, widespread fuel cell deployment still faces significant challenges including electrocatalyst activity and durability, fuel feed and storage issues, and the necessity for a hydrogen distribution infrastructure.

The distinction between a PEMFC and other types of fuel cells usually lies in its electrolyte—in this case, a solid polymer membrane serves as the electrolyte barrier between the cell anode and cathode. The membrane dictates fuel cell operating conditions in order to remain operational.[5] It is designed to permit the flow of protons, generated at the anode, to the cathode while limiting the crossover of reactants. The membrane can be the source of many device problems, as it must be properly hydrated in order to maintain high levels of

conductivity.[5] The issue of membrane hydration necessitates the relatively low operating temperatures of PEMFCs in relation to other fuel cells. As a result of these lower operating temperatures, expensive precious metal catalysts are usually required to achieve acceptable levels of energy production.[1]

PEMFCs are capable of harvesting energy from a number of different fuels. From a performance perspective, the use of pure hydrogen at the anode would be most desirable, as hydrogen-fed fuel cells can achieve high efficiency due to the facile kinetics of the hydrogen oxidation reaction (HOR).[6,7] However, difficulty associated with the production, storage and handling of gaseous hydrogen has limited its commercialization.[8] Considering these shortcomings, liquid fuels are attractive alternatives fed to the anode of direct liquid fuel cells (DLFCs). Promising examples of DLFCs include direct methanol fuel cells (DMFCs) and direct formic acid fuel cells (DFAFCs). The liquid fuels, methanol and formic acid, can be fed directly to the anode without the need for a reformer, reducing device complexity and weight, simplifying storage and handling, and maintaining a higher volumetric energy density than pure hydrogen.[2,4,9]

Alkaline Anion Exchange Membrane Fuel Cells

An alternative to PEMFCs, AAEMFCs have recently garnered increased interest following the development of stable and conductive, polymer anion exchange membranes.[10] Unlike in a PEMFC, the polymer electrolyte of the AAEMFC conducts hydroxide ions from the cathode to the anode, where the ions

react with hydrogen to produce water and release electrons. AAEMFCs hold considerable promise because the oxygen reduction reaction (ORR) kinetics in alkaline electrolyte is more facile compared to the ORR in acid. This is expected to allow for the replacement of Pt catalysts at the cathode with cheaper alternatives without the same stability concerns as in acid, to reduce overall device cost. A major problem with these systems is that kinetics of the HOR is considerably less facile than in acid.[11] Overcoming the issue of slow anode kinetics by the design of active alkaline HOR catalysts is still required before these devices may be considered for widespread commercial use.

Fuel Cell Electrocatalysts

Electrocatalysts are essential components of the fuel cell and are located in the two electrodes that are separated by the polymer electrolyte membrane, the anode and cathode. Platinum and platinum alloys are generally the most active choices for the electrocatalyst in low temperature fuel cells.[2,12,13] However, the limited availability and high cost of this and other preferred precious metals have hindered the widespread commercialization of fuel cells as power sources. Additionally, the highly active, commercially available catalysts typically lack the durability required to justify their high cost. These commercial supported catalysts are typically fine metallic nanoparticles that are well dispersed on a high surface area, electron-conducting support, like carbon, which allows for high utilization of the catalyst. However, the catalyst nanoparticles are weakly

adsorbed to the carbon support in this catalyst design, and this catalyst-support interaction is largely responsible for their associated durability issues during fuel cell operation.

Nanostructured Electrocatalysts and the Motivation for Restricting Size to the Nanoscale

In addition to the unique material properties that arise from the reduction of size to the nanoscale, nanostructured materials have a large surface-area-to-volume ratio and an inherently high density of atoms at the catalytic interface. One of the driving forces for decreasing the size of electrocatalysts is a need to reduce their cost, as the size reduction of nanoparticle catalysts leads to a higher utilization of the precious metals and maximum activity per catalyst mass, or mass activity. Many other concurrent benefits arise from the confinement of these materials to the nanoscale.

Recently, one-dimensional (1D) nanostructures have gained increased interest as fuel cell electrocatalysts. By definition, 1D nanostructures have two of their dimensions restricted to the nanoscale, while the third dimension may extend into the microscale. Some examples of 1D nanostructures include nanotubes, nanowires or nanorods, and nanodendrites.[14–16] These 1D nanostructures have a high aspect ratio, and their structural anisotropy has been observed to promote a number of unique properties from the bulk, making them

interesting to a number of research fields beyond electrocatalysis as supercapacitors,[17] battery electrodes,[18] thermoelectrics,[19] and photovoltaics.[20]

One-dimensional nanostructures have proven highly active and durable in applications as electrocatalysts with these performance improvements usually attributed to morphology-dependent properties that are suggested to arise from their anisotropy. There have been several studies that have attempted to directly correlate activity improvements in 1D nanostructures to their structural morphology by comparing these extended surface catalysts to 0D analogs, supported nanoparticles, using the same metals for oxygen reduction,[21,22] methanol oxidation,[23,24] ethanol oxidation,[25] and formic acid oxidation.[26] Relative to 0D structures, the extended nature of the surfaces of 1D nanostructures promotes surface expression of low energy, extended crystalline planes and a reduction in the density of under-coordinated sites.[27] In some of the synthesis techniques used to form platinum group metal 1D nanomaterials, the thermodynamics of the synthesis or the use of shape-directing agents can cause the materials to preferentially grow along a particular axis,[15] expressing higher densities of active, low energy facets at the catalyst surface that can enhance activity for alcohol oxidation and oxygen reduction.[28,29] It has also been suggested that the structural anisotropy of ultrathin nanostructures causes reductions in the metal d-band center, weakening the adsorption of reactants and

intermediates to the extended catalyst surface that may otherwise adsorb more strongly to the surfaces of 0D spherical nanoparticles.[25,30]

Distinct from anisotropic 1D nanostructures, two-dimensional (2D) nanostructures are defined by having only one dimension confined to the nanoscale with examples including nanotubes, nanodisks, nanoplates, and nanosheets, or extended surface planes. Many of the advantageous properties of 1D nanostructures that result from their extended and more coordinated surfaces also apply to 2D nanostructures. For example, these extended surfaces typically feature a reduction in crystal defect populations, minimizing their surface energies.[14–16] As mentioned previously in regard to 1D nanostructures, this means that 2D nanostructure surfaces favor low energy, extended crystal planes and terraces over the under coordinated corners and edges that dominate the surfaces of 0D nanoparticles because of their small size.[31,32] This is a major advantage of extended surface catalysts, as 0D nanoparticle surfaces are rich in under coordinated atoms[32–34] that are more vulnerable to corrosion and irreversible oxidation[35] and are more oxophilic than highly coordinated atoms.[30]

Extended Surface Catalysts: Durability and Specific Activity Enhancements

Extended surface catalysts are a promising alternative to potentially replace supported nanoparticles as electrocatalysts in fuel cells that can circumvent some of the major shortcomings that arise in weakly interacting metallic nanoparticles with carbon support materials. Supported platinum

nanoparticles are known to lose active surface area during fuel cell operation by three main degradation modes: dissolution from small crystallites and redeposition at the surfaces of larger particles (Ostwald ripening), agglomeration of mobile nanoparticles along the carbon support to form larger nanoparticles, and detachment of nanoparticles after corrosion of the carbon support to agglomerate and form larger particles.[35–38] Additionally, large particles of unreactive Pt, no longer electronically connected, can also be recovered from a membrane or cathode ionomer phase after fuel cell operation that results from Pt dissolution and chemical reduction by hydrogen that has crossed over the membrane from the anode of the cell.[39]

Extended surface catalysts, alternatively, could potentially circumvent the need for a carbon support,[40] owing to high aspect ratios of the already aggregated catalyst. This would mean that devices based on extended surface catalysts would not be constrained by some of the common degradation problems for supported nanoparticles related to carbon support corrosion or oxidation.[23,40,41] In supported catalysis where there is a motivation to reduce the particle size to increase the dispersion and electrocatalytically active surface area (ECSA), and ultimately the mass activity, there is a concomitant increase in the density of low-coordination edge sites, corners, and less active (for ORR) crystal faces.[42] Extended surface catalysts, on the other hand, generally have increased coordination of surface atoms and reduced surface energies, making

them less disposed to dissolution and ripening than is common in small, supported nanoparticles.[14,15,35,36] This shortcoming of 0D catalysts is highlighted in experiments on Nanostructured Thin Films (NSTFs), where a thin film of metal was sputter-coated onto a polymer whisker by physical vapor deposition (PVD).[43] After accelerated durability cycling experiments, carbon-supported Pt was observed to lose 90% of its ECSA after 2500 cycles due to agglomeration, while the Pt-NSTF lost only 20% of its ECSA after 4225 cycles.[44]

Extended surface catalysts frequently demonstrate significantly higher specific activities, the reaction rate normalized to ECSA, than 0D counterparts as a result of unique surface and electronic properties and high aspect ratio morphology. The NSTFs mentioned previously are no exception, as these high-aspect ratio catalyst-polymer composites are capable of producing specific activities for ORR comparable to polycrystalline Pt in monometallic Pt-NSTFs.[45] Using this same catalyst architecture, a number of bimetallic and ternary metallic alloy NSTFs were similarly prepared, with a $PtNi_2$-NSTF electrocatalyst maintaining a specific activity an order of magnitude higher than the commercial supported Pt, and a mass activity nearly 2.5 times higher.[45] Later work by this group led to the design of a new class of catalysts, mesostructured thin films, using the same PVD technique to sputter Ni, followed by Pt, on polymer whiskers.[31] After thermal annealing, the as-deposited nanograins at the whisker surface were observed to coalesce, forming larger crystalline grains with reduced

surface energies and smoother surfaces without compromising the original gross morphology. These non-alloyed, Pt-Ni electrocatalysts were found to be 8 times as active as polycrystalline Pt for the ORR.[31] However, despite removing the inert supporting polymer from the mesostructured catalyst's interior, the interior surfaces of these structures were found to be inaccessible for catalysis, as measured ECSA values did not reflect the availability of the interior surface.[31]

Extended Surface Catalysts: Platinum Group Metal Nanotubes

In an effort to respond to the deficiencies of the nanoparticle supported catalysts currently preferred in fuel cells, platinum group metal nanotubes have been synthesized by a modified chemical vapor deposition technique. The nanotube morphology is obtained by the deposition of conformal metal coatings along the interior channels of a porous, sacrificial, anodic alumina membrane. Other groups have synthesized PGM nanotubes using different methods and have shown that these materials demonstrate promise as electrocatalysts for a number of reactions.[40,46–49] The hollow nature of these nanotubes can be advantageous for catalysis and methanol oxidation experiments summarized in Figure A.1 in the Appendix indicate that the nanotube interiors are in fact active. In addition to accessible exterior surfaces, hollow nanotubes offer a second active interior surface, unlike with nanorods or NSTFs, which have inaccessible cores that are filled with metal or an inert polymer, respectively. Additionally, the geometry of a hollow cylinder suggests that there is a potential for increasing the

surface-area-to-volume ratio by reducing the cylinder wall thickness. This implies that carefully reducing the wall thickness can lead to significant enhancements in the ECSA and mass activity of a nanotube despite the relatively large size (250 nm diameter). The hollow interior also allows the possibility of creating a bi-functional nanotube, where two different materials could be layered and serve unique functions within a desired application. For example, a layered Pt-Ru nanotube could oxidize methanol on Pt sites at its exterior surface while forming oxygenated species on the interior Ru surface that may lead to improvements in methanol oxidation activity. This vapor synthesis method and optional thermal treatment offer flexibility for the design of highly active and durable electrocatalysts.

Modified Chemical Vapor Deposition for the Development of Platinum Group Metal Nanotubes

In light of the discussed limitations of some other techniques used to synthesize extended surface nanostructures, we have developed a method for synthesizing monometallic, discretely layered bimetallic, and alloyed bimetallic nanotubes based on a modified chemical vapor deposition (CVD) method. This CVD technique does not require the expensive instrumentation normally associated with conventional CVD, and it utilizes slow temperature ramp rates, which favor the precursor sublimation at relatively low temperatures.[50–52] Thermogravimetric Analysis (TGA) analyses at various ramp rates for precursors

used in this work are presented in the Appendix in Figures A.2, A.3 and A.4. In this vapor deposition technique, metalorganic precursors are decomposed by mild heat treatment in a vacuum oven below 250°C to deposit conformal coatings of nanoparticulate films on the surfaces of a selected substrate. In addition to the vapor growth of platinum group metal nanotubes, this technique has also been used to synthesize highly-dispersed, metallic nanoparticles on high surface area carbon supports.[50,53,54] This technique allows for a high degree of customization because there are a number of parameters that may be adjusted in order to synthesize materials with desired properties. For example, where the use of galvanic displacement necessitates the ordering of materials based on metal nobility in the galvanic series, this modified CVD technique may be used to deposit multiple metals in any order. The 3-5 nm nanoparticles that are deposited using an application of this technique, whether supported on carbon or in a sacrificial template, are situated in a size range preferred for many applications in catalysis, from hydrogen oxidation in alkaline electrolyte to oxygen reduction in acidic electrolyte.[55–57] Finally, because the synthesis products are conformal in nature, sacrificial and temporary supports of arbitrary shape may be coated and later removed to form a metal network or nanostructure of nearly any shape desirable.

Optional Thermal Annealing Process for Structural and Chemical Evolutions

In addition to the advantageous chemical vapor deposition technique described here for the synthesis of highly active extended surfaces, templating with a thermally stable material like anodic alumina allows for post-synthesis thermal annealing. Heat treatment of these conformal coatings is often not possible with other surfactant and solutions-based chemistry techniques or soft polymer template methods, where the template has a low melting point or glass transition temperature, like with polycarbonates.[14,15] These commercial aluminum oxide templates are stable to at least 750°C, a temperature high enough to observe major structural evolutions in these metallic thin films despite being considerably lower than the melting points of the respective bulk metals, since there is a greater proportion of surface atoms and reduced coordination compared to bulk materials.[58–60]

During heat treatment, nanotubes observe a number of structural changes that have considerable implications on catalysis. The most noticeable effects of the heat treatment are related to evolutions in the nanotube structure and are based on grain growth that follows increases in temperature. As the temperature is increased, small nanoparticle crystallites coalesce to form larger grains, there is a subsequent reduction in the density of low coordination sites at the surface, the nanotube wall thickness decreases, and nanoscale wall porosity forms. In

certain cases the nanotubes may be annealed in reducing or oxidizing environments to induce chemical phase transitions or to remove any impurities that may form during synthesis. Finally, in bimetallic nanotubes at certain compositions, high temperature annealing treatments can provide the driving force for homogeneous or multi-phase alloy formation. Each of these consequences of the optional heat treatment allows tailoring the material properties of the catalyst in order to influence the activity for the various reactions studied in this work.

Structural Changes in Annealed Nanotubes: Grain Growth

A supported nanoparticle is not the most accurate representation of the coarse grains that compose the walls of annealed, metallic nanotubes. However, general particle size trends reported in the literature could still guide the development of platinum group metal nanotubes. Increasing the grain size in extended metal surfaces can lead to similar behavioral trends observed in larger metal crystallites supported on carbon. There are a number of reports on particle size effects of nanoparticulate catalysts for electrochemical reactions, the result of changes in the expression of certain crystal planes at the catalytic interface as a function of the nanoparticle size.[55–57,61–74] In an early study of the oxygen reduction reaction, Kinoshita reported a maximum mass activity for Pt/C with 3.5 nm Pt crystallites.[55] However, these experiments were conducted in sulfuric acid; the strong sulfate adsorption on Pt (111)[74] led Kinoshita to initially suggest that

the (100) plane was more active for ORR.[55] More recent reports have indicated that ORR mass activity increases with the catalyst dispersion and is independent of the electrolyte—as the particle size decreases, the active surface area and mass activity increase.[68] The opposite correlation with particle size and activity is true for ORR specific activity, where the specific activity was observed to increase directly with particle size from a minimum in 1-5 nm supported Pt nanoparticles to unsupported Pt black (30 nm) to a maximum specific activity in polycrystalline Pt. The size dependency of ORR specific activity was attributed to delayed surface oxidation and increased site availability with increasing grain size.[42,68]

The design of an active catalyst requires balancing low activation energy for oxygen adsorption and the rapid release of products.[75] Platinum nanoparticles dissociate molecular oxygen easily but can overbind atomic oxygen, which is thought to be responsible for observed reductions in activity for the ORR.[75–77] The stronger adsorption of oxygenated species on the surfaces of smaller nanoparticles has been suggested to be a result of the increase in under coordinated atoms at the surface of the small nanoparticle.[32–34,71] This observation is considered responsible for decreases in ORR specific activity with decrease in particle size, as active sites on smaller nanoparticles are more easily covered by OH_{ads}.[78] Extended surfaces of Pt generally form surface oxides at higher potentials than supported nanoparticles,[79] offering greater site availability

that translates to improvements in oxygen reduction activity.[80] This delay of surface oxidation was similarly observed by Mayrhofer et al. for Pt nanoparticles with increasing grain size; the larger nanoparticles also demonstrated the highest specific activity for ORR.[66]

The changes in coordination that accompany changes in particle size have been reported to affect other reactions, like the oxidation of carbon monoxide.[73] Increasing nanoparticle size has been shown to result in improved CO tolerance, and larger Pt crystallites oxidize CO_{ads} at reduced potentials compared to smaller nanoparticles.[62,70,73,81,82] This result has been attributed to the weaker interaction of CO_{ads} on more coordinated surfaces[62,70,73,81–83] and the concomitant increase in CO_{ads} diffusion across the catalyst surface in order to be oxidized by OH_{ads} via a phenomenon first described by Cherstiouk and Savinova.[81] At high oxidation potentials, the OH_{ads} needed to oxidize CO_{ads} from the catalyst surface adsorbs at specific active sites—reported to be nanoparticle vertices or edges[70]—and CO_{ads} adjacent to this OH_{ads} is oxidized first.[81] The remaining, more distant, CO_{ads} on the surface is suggested to be oxidized once it has diffused to sites adjacent to those occupied by OH_{ads}.[81] Therefore, small nanoparticles that bind CO_{ads} more strongly, and therefore, have slower CO_{ads} diffusion across the catalyst surface to OH_{ads}, are less active for CO_{ads} oxidation.[64,65,81] This result has significant implications for the oxidation of

alcohols like methanol and formic acid, where CO_{ads} can form as a reaction intermediate that blocks the surface and deactivates the catalyst.

The grain growth observed in these metallic nanotubes during heat treatment also promotes the formation of nanoscale porosity in the nanotube walls. Nanoscale porosity has been shown to improve the mass transport properties of a catalyst and improve its activity because in addition to the open ends of the nanotube, reactants and desorbed products can also diffuse through the pores in the walls.[41,84,85]

Structural Changes in Annealed Nanotubes: Alloy Formation

The ability to introduce a second metal to the nanotubes during synthesis can allow for a significant change in electronic properties, whether by alloying or by strain from applying thin overlayers of one material on the surface of another material with a different lattice parameter.[86] Use of a second metal can also allow for replacing some of the precious metal with a less expensive base metal with potential for activity improvements. There have been numerous reports in the literature of alloyed, extended surface catalysts that outperform monometallic counterparts for a number of electrochemical reactions, normally attributed to an electronic effect from the second metal.[22,31,45,87–90] Additionally, there has been a push in the extended surface catalyst literature towards monolayer or overlayer coated surfaces that can maximize the utilization of expensive catalysts despite

using a relatively low surface area structure, while the less expensive metal is assigned to the subsurface as the support.[24,46,49,91–93]

Structural Changes in Annealed Nanotubes: Chemical Phase Transition

For the deposition of some materials using this modified CVD technique, the synthesis products may be amorphous or crystalline oxides. In some applications, these metal oxides may be advantageous. For example, researchers have found that the amorphous form of ruthenium oxide has specific capacitance values that are orders of magnitude higher than the anhydrous, crystalline ruthenium oxide.[94] There is also a distinct advantage from using hydrated ruthenium oxides exclusively as the ruthenium species in Pt-Ru catalysts for the methanol oxidation reaction, as it has been found to promote the methanol oxidation reaction activity of platinum by 2 orders of magnitude over the crystalline ruthenium oxide or metallic ruthenium species.[95] Though in these specific examples involving ruthenium, the hydrous oxide phase is preferred, this is not always the case. By thermal annealing treatments in an inert or reducing environment, these oxides may be dehydrated or reduced to a metallic phase, respectively. This ability to control the material phase by adjusting the gas environment and temperature of the heat treatment allows considerable flexibility for tuning the properties of these nanotubes for the selected application.

CHAPTER 2

OXYGEN REDUCTION ACTIVITY OF VAPOR-GROWN PLATINUM NANOTUBES

A version of this chapter was originally published in the Journal of the Electrochemical Society:

Papandrew, A. B.; Atkinson III, R. W.; Goenaga, G. A.; Kocha, S. S.; Zack, J. W.; Pivovar, B. S.; Zawodzinski Jr., T. A. Oxygen Reduction Activity of Vapor-Grown Platinum Nanotubes. *J. Electrochem. Soc.* **2013**, *160*, F848–F852.

Abstract

Supportless platinum nanotubes (PtNTs) were synthesized by the decomposition of platinum acetylacetonate vapor within anodic alumina templates at 210°C. As synthesized, the nanotubes are nanoparticulate aggregates composed of Pt crystallites approximately 3 nm in diameter and with a range of lengths from 1 μm to 20 μm. Annealing treatments result in crystallite growth and morphological evolution of the tubular nanostructures including the development of nanoscale porosity. In rotating disc electrode measurements carried out in 0.1 M $HClO_4$, porous PtNTs annealed at 500°C exhibited a specific activity for oxygen reduction of 2390 $\mu A/cm^2_{Pt}$ at 0.9 V, comparable to bulk polycrystalline Pt. The electrochemical surface area of the annealed structures was a relatively low 10 m^2/g, resulting in a moderate overall mass activity of 240 ± 41 mA/mg_{Pt}.

Introduction

Carbon-supported metal electrocatalysts remain the dominant paradigm in low-temperature fuel cell systems, but are not without significant shortcomings.[38] Carbon in contact with precious metal catalysts is vulnerable to oxidation[96] at anodic potentials, and supported catalysts with acceptably small particle sizes are predisposed to dissolution[36] that can result in coarsening of existing particles or precipitation of metal within the polymer membrane.[39] Additionally, a correlation between particle size and specific activity has been established,[42,66,68,97] and surface area gains achieved by reductions in particle size are partially offset by a loss of specific activity.

In response to these deficiencies, an alternative to the established supported catalyst approach has emerged in the form of extended thin film electrocatalyst structures (ETFECS). The concept guiding the development of these materials is the adoption of high-aspect ratio morphologies to achieve high specific ORR activity while limiting sacrifices in electrochemical surface area (ECA). The progenitor of the current crop of ETFECS is the nanostructured-thin film (NSTF) electrocatalyst[98] developed by 3M. Synthesized via a physical vapor deposition (PVD) route (sputtering), NSTF electrodes are defined by thin films of polycrystalline Pt coating an array of high-aspect ratio, non-conductive polymer whiskers.[43] NSTF electrocatalysts exhibit higher specific activity[99] and better voltage stability[44] than standard carbon-supported architectures in PEMFC

architectures with cathode Pt loadings as low as 0.10 mg/cm^2. Conversely, electrochemical surface areas for NSTF structures are low (10 m^2/g$_{Pt}$),[98] and the thin electrodes present difficulties for water management.[100]

A range of additional extended metal structures has been developed in recent years. These include platinum nanowires[79] and nanotubes[40,101] synthesized via galvanic displacement, and meso-structured platinum materials made via templating methods.[31,102] Hollow tubular nanostructures are of particular interest, due to the prospect of accessing the inner Pt surface, which does not exist in a nanowire and is inaccessible in the NSTF composite structure.

Given the success of vapor deposition in the case of NSTF, we sought an alternate route to high-aspect polycrystalline Pt ETFECS using a modified form of metalorganic chemical vapor deposition (CVD). CVD methods have the potential to bypass the line-of-sight restrictions of PVD to produce conformal films on arbitrary three-dimensional structures.

In this contribution, we describe the use of the metalorganic platinum acetylacetonate [Pt(acac)$_2$] to deposit conformal Pt nanoparticle films within the pores of anodic alumina (AAO) templates via a heat treatment at 210°C. After Pt deposition, the Pt-decorated templates were subjected to annealing treatments to induce particle growth and meso-structural evolution. Finally, the templates were etched away to liberate freestanding Pt nanotubes (PtNTs). By adopting a sacrificial template, rather than a retained template (as in the case of NSTF), we

sought materials suitable for developing highly dispersed, ink-based electrodes that can address difficulties with water management associated with highly active, ultrathin electrodes.

Experimental

Platinum nanotubes were synthesized by the deposition of platinum within the pores of a porous template and subsequent template dissolution. A powder of platinum(II)(2,4)-pentanedionate [$Pt(acac)_2$] (Alfa Aesar) was applied to the surface of an anodic alumina membrane (Whatman Anodisc, 13 mm diameter, 200 nm nominal pore size). The amount of platinum deposited was tuned by adjusting the precursor dose. In this study doses of 100 mg or 75 mg were used. The powder-covered disc was transferred to a vacuum oven containing 2.3 mL of de-ionized water in a glass vial. The oven was evacuated with a rotary vane vacuum pump and purged with dry N_2 several times, then evacuated to 0.3 bar and sealed. The oven thermostat was set to a calibrated value of 210°C. After vaporization of the liquid water, equilibrium was reached after approximately 75 minutes at a total pressure of 0.8 bar, as measured by a Bourdon gauge. After fifteen hours at 210°C, the oven was evacuated, flushed with dry N_2, and cooled to room temperature.

The Pt-coated template was then heat-treated or immediately dissolved. Heat treatments were performed on sample discs in a quartz tube furnace under flowing dry N_2. After purging the tube at room temperature for 1 hour, samples

were held at 500°C for 1 hour, and then allowed to cool passively to room temperature.

Templates were dissolved by magnetic stirring of the discs in 30% KOH solution at room temperature for 96 hours. The supernatant solution was then decanted and replaced with de-ionized water, a process repeated until the pH of the supernatant solution was neutral.

Samples of as-synthesized and heat-treated nanotubes were analyzed by scanning electron microscopy (SEM), transmission electron microscopy (TEM), and x-ray diffraction (XRD).

Samples for microscopy and diffraction analysis were prepared by drop-casting methods. A pipette was used to extract a small amount of water-dispersed solids from the bottom of each sample container, and a drop was applied directly to either an aluminum SEM stub, copper TEM grid, or a zero-background Si XRD sample platen.

SEM imaging was performed with a ZEISS 1525 FESEM at an accelerating voltage of 3 kV using the in-lens electron detector. TEM imaging was conducted with a ZEISS Libra 200MC operating at an accelerating voltage of 200 kV. XRD was conducted with a Philips X'Pert x-ray diffractometer with Cu Kα radiation (λ = 0.1541874 nm, 45 kV, 40 mA, 0.04° step, 2.0 s/step) and a graphite monochromator in the diffracted beam. Peak width analysis of these patterns was performed using the Philips X'Pert Highscore Plus software.[103]

The initial concentration of as-prepared PtNT-H_2O suspensions (in mg/mL) was measured with a nanobalance after evaporating a small aliquot at 60°C. Concentrations in the range of 1.27-2.07 mg_{Pt}/mL were found. Electrode inks were made by dilution of the PtNT-H_2O suspensions with additional water. In our initial studies, no alcohol or ionomer was added to the inks, as is common for high surface area catalysts.[104] Later investigations of the most active samples focused on the effect of ionomer addition on catalyst activity.

Rotating-disc electrode (RDE) and cyclic voltammetry (CV) measurements were performed in a custom-designed electrochemical cell with a glassy carbon (GC) working electrode, Pt gauze counter electrode, and a reversible hydrogen reference electrode (RHE). Before addition to the GC electrode, sample inks were sonicated in an ice bath for 20 minutes to disperse solids. The working electrode was prepared by a 10 µL dose of the electrode ink dried in air at 40°C.

The 0.1 M $HClO_4$ electrolyte (GFS Chemicals) was deoxygenated by sparging with ultrahigh purity N_2 gas for at least 30 minutes prior to all electrochemistry experiments. The electrodes were then conditioned with 50 cycles at 100 mV/sec from 0.025 V to 1.2 V. Subsequent to conditioning, three additional cycles were performed at 20 mV/sec from 0.025 V to 1.0 V. The charge under the hydrogen underpotential deposition peaks in these three cycles was used to compute the electrochemical surface area (ECA) of the PtNTs. After determination of ECA, the electrolyte was saturated with oxygen by sparging for

5 to 10 minutes with ultrahigh purity O_2. Linear sweep voltammetry (LSV) at 1600 rpm electrode rotation rate and a sweep rate of 20 mV/s was used to determine the oxygen reduction reaction activity of the electrode. In each experiment, the anodic potential sweep (i.e. a sweep towards more positive potentials) was from -0.01 V to 1.0 V. Measurements were made at room temperature and ambient pressure (83 kPa); the reported results are corrected to 100 kPa as detailed previously.[105] Corrections in the kinetic regime were made with a total reaction order of m=0.85,[105] and limiting currents were corrected to account for the lower solubility of oxygen at 83 kPa. To ensure statistically significant results, multipled trials were performed with both experimental and control sample inks. Eleven samples spread across two different inks were used for the most active PtNT sample.

Results and Discussion

Scanning electron micrographs of high-uptake [100 mg $Pt(acac)_2$ precursor dose; 12 mg_{Pt}/template] as-synthesized and low-uptake heat-treated [75 mg $Pt(acac)_2$ precursor dose; 8 mg_{Pt}/template] PtNTs are shown in Figure 2.1. The samples show a similar gross morphology corresponding to the pore structure of the anodic alumina templates, namely, a roughly circular cross-section with an approximate diameter of 200 nm and lengths a fraction of the 50 μm thickness of the template. At smaller length scales, significant differences in the microstructure of the PtNTs are apparent.

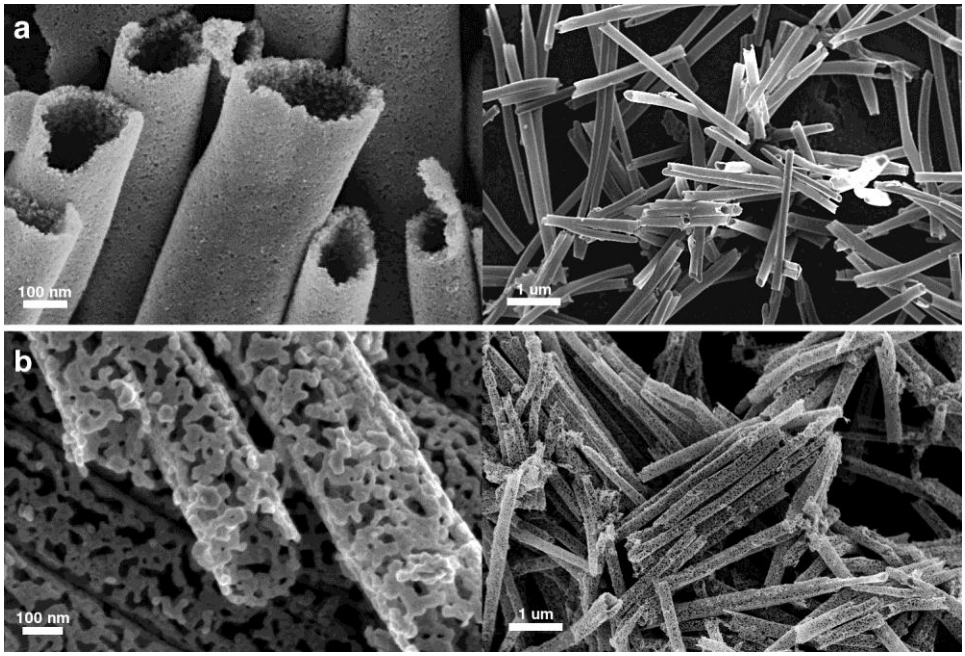

Figure 2.1. SEM micrographs of (a) Pt nanotubes as-synthesized and (b) after annealing in flowing N_2 at 500°C.

Before heat treatment, the walls of the nanotubes are approximately 10-20 nm thick and have a fine-grained and uniform appearance. At high magnification (~100 kx) individual nanoparticles can be resolved with difficulty. After annealing, the walls of the nanotubes become thinner, decreasing to an approximate thickness of 5-10 nm. Grain boundaries are still plainly visible, and suggest significant grain growth. Non-uniform porosity is also observed in the walls of the annealed nanotubes, resulting in a highly irregular filigree-like structure.

The structural evolution of the PtNTs after heat treatment is confirmed in TEM micrographs shown in Figure 2.2. The inset selected-area diffraction

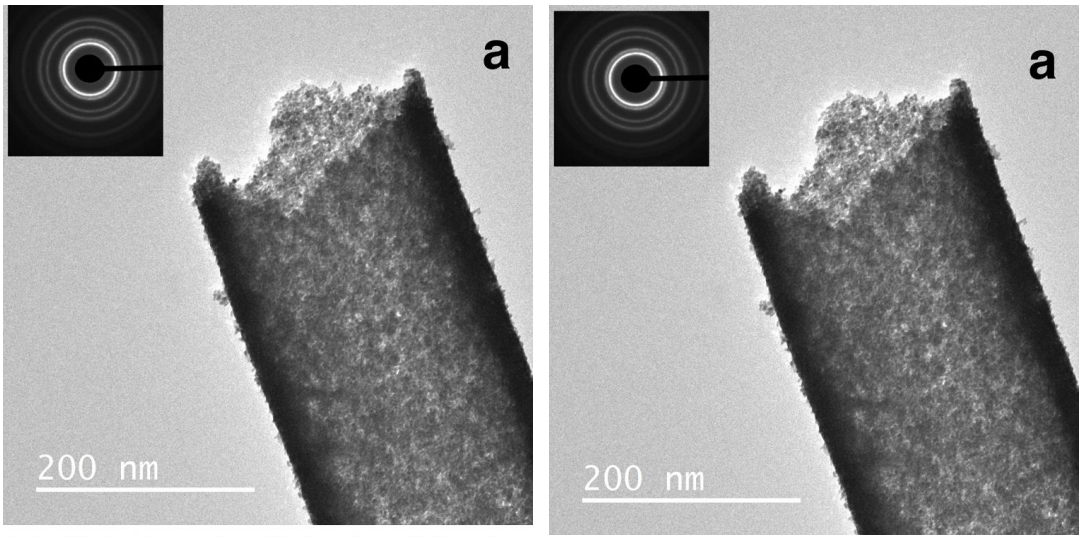

Figure 2.2. TEM micrographs of Pt nanotubes (a) as-synthesized and (b) after annealing in flowing N_2 at 500°C. Selected-area diffraction patterns for each sample are inset.

patterns display diffuse, continuous Debye rings in the case of the untreated sample, and discontinuous rings after heat treatment, indicating that fewer crystallites are sampled by the electron beam, i.e. the crystallites have grown.

X-ray diffraction was used to quantify the initial crystallite size of the PtNTs before and after heat treatment. Cu Kα diffraction patterns are shown for the as-synthesized and heat-treated nanotubes in Figure 2.3. A clear sharpening of the diffraction peaks is evident with heat treatment, indicating crystallite growth. Grain sizes were computed using the Scherrer equation

$$L = \frac{0.9\,\lambda}{B\cos\theta}$$

applied to the Pt(111) peak. Here, B is the full width at half maximum intensity of the peak, θ is the Bragg angle, and for Cu Kα, λ = 0.154060 nm. The results of these calculations are shown in Table 2.1.

Table 2.1. Lattice Parameter, a, and Crystallite Size, L, of Platinum Nanotubes Before and After Annealing.

Sample	a [nm]	L [nm]
as-synthesized	0.39040	2.6
500°C	0.39213	15.2

As-synthesized PtNTs have a mean grain size of approximately 3 nm, a value that increases to 15 nm after annealing; grain size was found to be

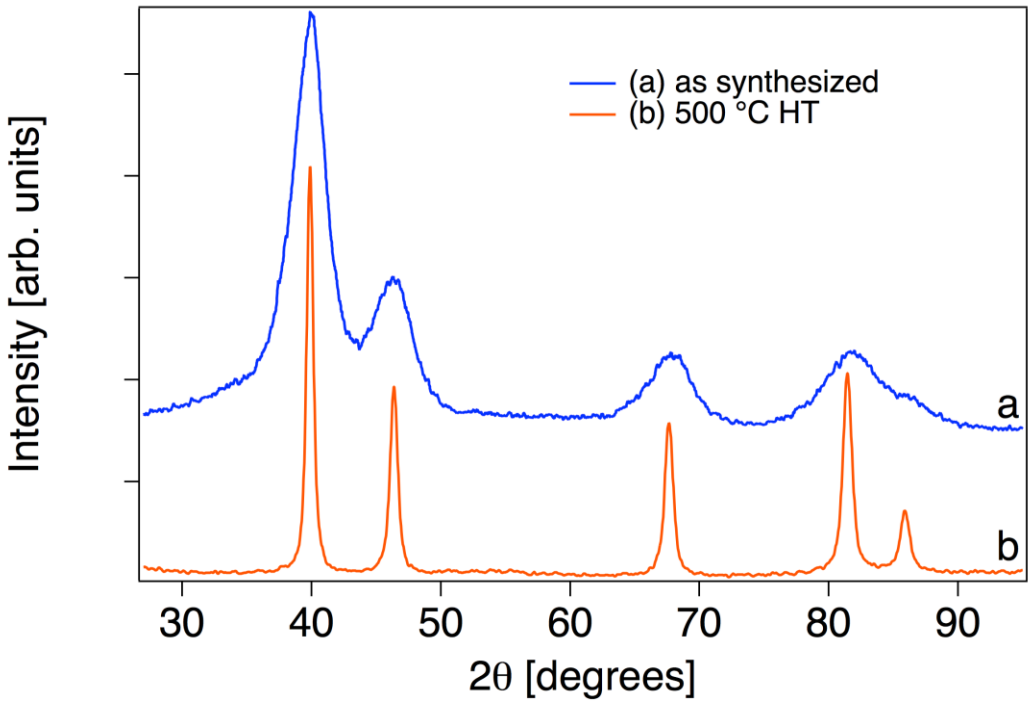

Figure 2.3. Cu Kα x-ray diffraction patterns of (a) as-synthesized PtNTs and (b) PtNTs annealed in flowing N_2 at 500°C.

insensitive to Pt uptake. The lattice parameter of the untreated PtNTs is slightly contracted, in agreement with Pt nanoparticles we have synthesized using similar methods,[106] while the lattice parameter of the annealed samples is identical to polycrystalline Pt. We emphasize here that in the case of an unsupported nanotube, the Scherrer coherence length for a diffraction peak corresponds to a *grain* size, and not necessarily a *particle* size as in the case of supported nanoparticles. Micrographs of the annealed samples shown in Figure 2.1 and Figure 2.2 suggest that this is an important distinction, as we observe platinum surfaces that are clearly greater than 15 nm in extent.

Nafion-free cylic voltammograms of annealed PtNTs are shown with CV data from the control sample, 46wt% Pt supported on high-surface-area carbon [Tanaka Kikinzoku Kogyo (TKK) TEC10E50E, hereafter Pt/HSC] in Figure 2.4. The PtNT ECA calculated from the HUPD charge using the correspondence of 210 $\mu C/cm^2_{Pt}$ was found to be approximately 10 m^2/g_{Pt}. Based on a purely geometrical consideration of perfectly cylindrical Pt tubes with an outer diameter of 200 nm and 10 nm wall thickness, an ECA of 9 m^2/g_{Pt} is expected. This rough calculation suggests that Pt utilization in the Nafion-free case is high and implies that both inner and outer surfaces of the PtNT are available for HUPD, and by extension, the ORR.

Figure 2.4 also shows the effects of scaling the current density of the PtNT voltammogram by a factor of 10, proportional to the difference in ECA between

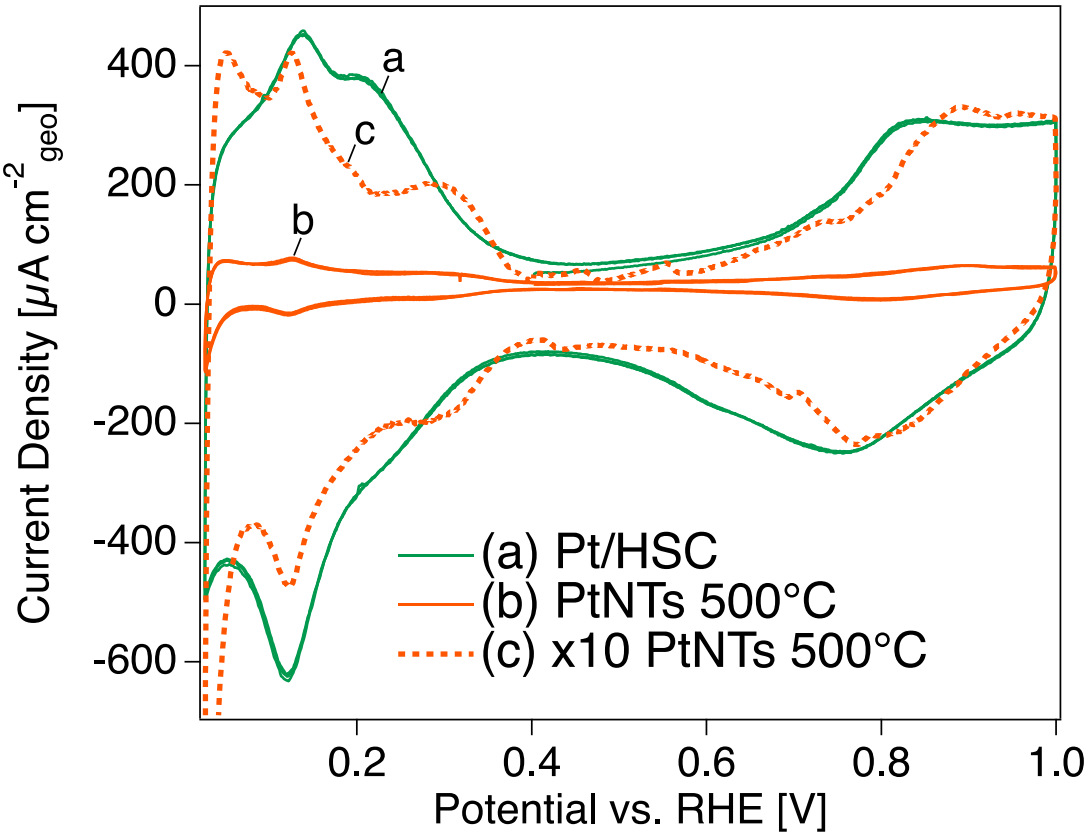

Figure 2.4. Representative cyclic voltammograms for the (a) Nafion-free Pt/HSC control electrode and (b) Nafion-free annealed, porous PtNTs recorded at 25°C and 20 mV/s in 0.1 M $HClO_4$. (c) Shows the current density of (b) multiplied by a factor of 10 to emphasize the features in the voltammogram.

PtNTs and Pt/HSC. Complete ECA values for experimental and control samples are shown in Table 2.2. The scaled voltammogram clearly shows an anodic shift in the onset of the Pt oxide formation feature and its concomitant reduction peak. These shifts are associated with increasing Pt particle size[66] and are observed in other extended Pt surfaces such as the NSTF electrocatalyst[44] and bulk polycrystalline Pt. Catalysts exhibiting this characteristic oxide shift typically display enhanced ORR activity due to a greater site availability.[80]

Table 2.2. ORR activity at 0.9 V and electrochemical surface area for PtNTs and baseline samples in ionomer-free electrodes. Measured in 0.1 M $HClO_4$ at room temperature and corrected to 100 kPa oxygen partial pressure.

Sample	$i_{s(0.9V)}$ [$\mu A/cm^2_{Pt}$]	$i_{m(0.9V)}$ [mA/mg_{Pt}]	ECA [m^2/g_{Pt}]
Poly-Pt	2200 ± 150	2.6	-
Pt/HSC	506 ± 37	497 ± 44	101 ± 4
PtNT (as)	1409 ± 178	141 ± 29	10 ± 0.8
PtNT (500°C)	2390 ± 423	241 ± 41	10 ± 0.8

Representative linear sweep voltammograms for annealed PtNTs and Pt/HSC are also shown plotted in Tafel form in Figure 2.5. Specific activity values at 0.9 V computed from multiple LSV trials for Nafion-free PtNT samples, a

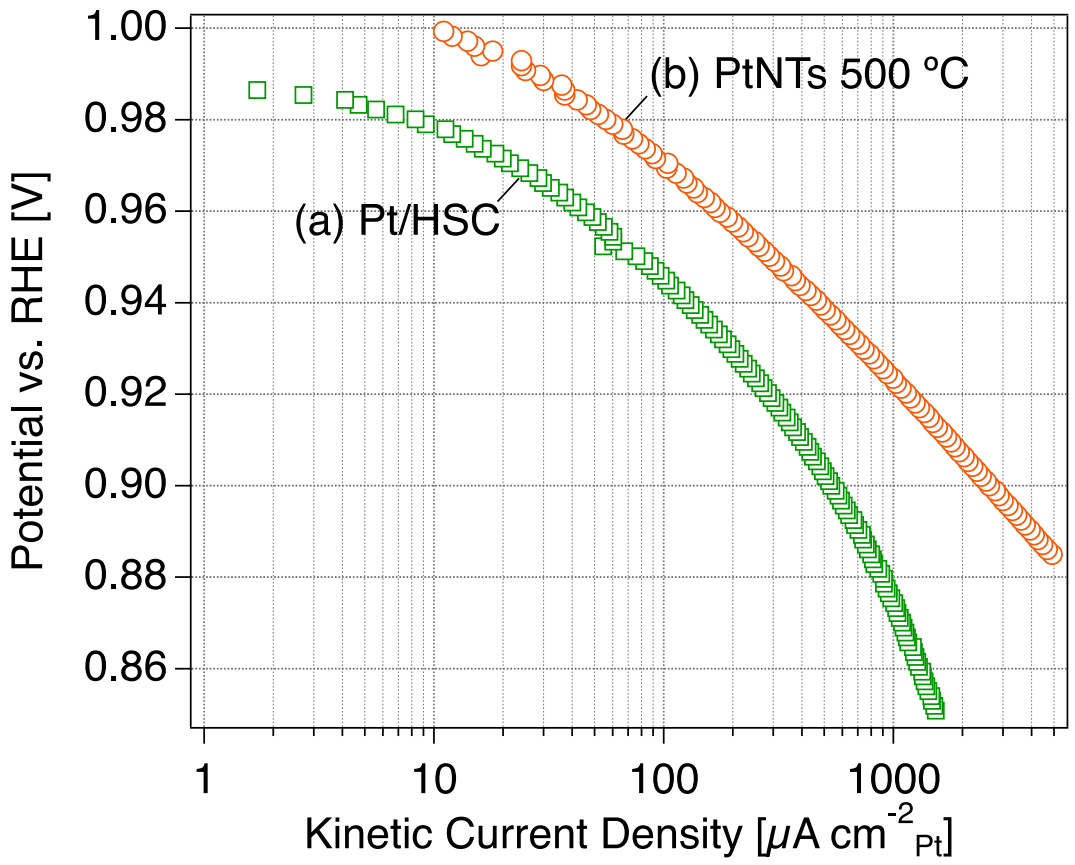

Figure 2.5. Representative Tafel plots for the (a) Nafion-free Pt/HSC control electrode and (b) Nafion-free annealed, porous PtNTs recorded at 25°C, 20 mV/s and 1600 rpm electrode rotation rate in 0.1 M $HClO_4$.

polycrystalline Pt disc, and Nafion-free Pt/HSC are shown in Table 2.2 and the results of each discrete trial of the experimental annealed PtNT catalyst are shown in Figure 2.6. Porous, low-uptake PtNTs annealed at 500°C show a specific activity on par with polycrystalline Pt and nearly five times that of Pt/HSC. Due to the relatively low ECA of PtNT samples, the mass activity of the catalysts is roughly half the mass activity of the supported Pt control. Average mass activity values for the Nafion-free experimental and control samples are collected in Table 2.2.

It is likely that the low mass activity of the annealed PtNTs stems from the suboptimal wall thickness of the tubular nanostructures. Walls that we judge to be 10 nm thick are approximately 3 to 4 times the diameter of a typical carbon-supported nanoparticle. Since the physical surface area of a nanotube scales with $1/t$, halving the wall thickness of the PtNTs would double the specific surface area, and thus similarly double the mass activity. This would bring PtNT mass activity into parity with Pt/HSC and satisfy the 2017 US DOE technical target. Achieving these thickness reductions may be possible via adjustment of the vapor deposition conditions or post-deposition acid treatments, for example. Alloying with base metals is also an established route to mass activity enhancements that could be the subject of future work.

The durability of the annealed PtNT catalysts was also investigated at room temperature in 0.1 M $HClO_4$. A Nafion-free electrode was cycled 20,000

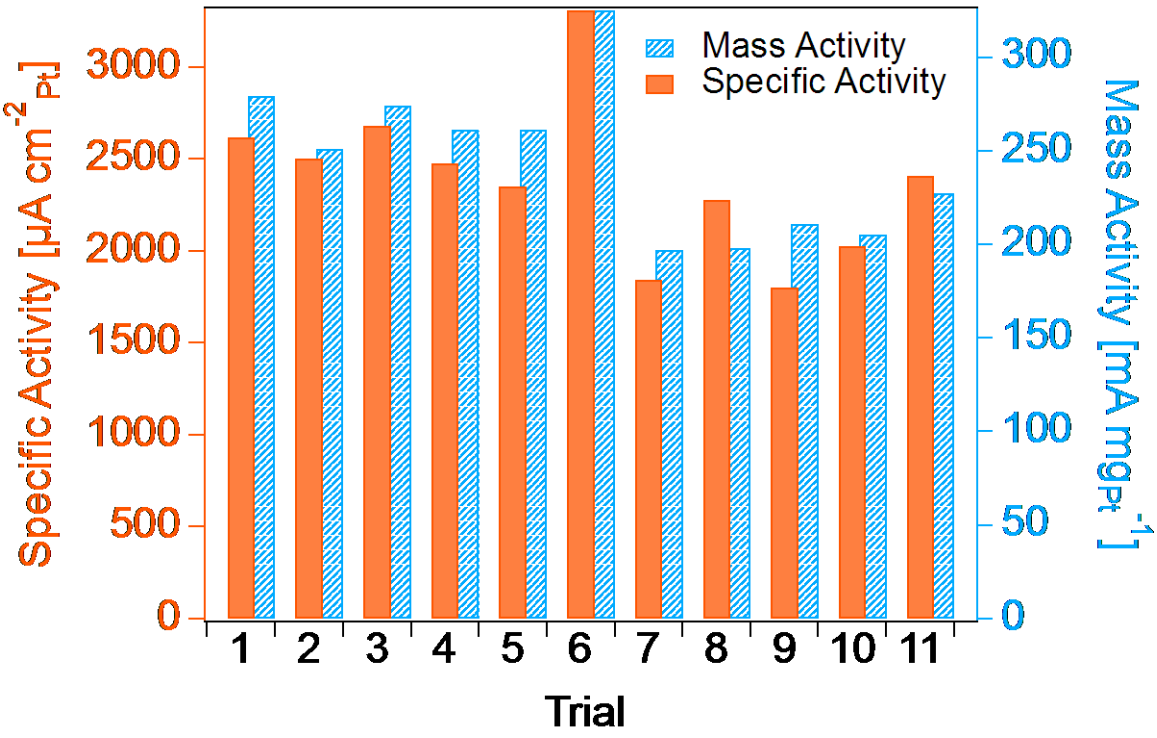

Figure 2.6. Summary of experiments conducted at 25°C in 0.1 M $HClO_4$ to determine specific activity and mass activity of porous PtNTs annealed at 500°C.

times at 50 mV/s from 0.6 V to 1.0 V. Electrode ECA was determined at regular intervals from HUPD charge obtained from voltammograms recorded from 0.05 V to 1.0 V. The evolution of the ECA value and selected voltammograms are shown in Figure 2.7. The annealed PtNTs are reasonably durable, retaining 66% of the initial ECA over the course of the experiment. Under identical experimental conditions, Pt/C was observed to lose half of its ECA.[41]

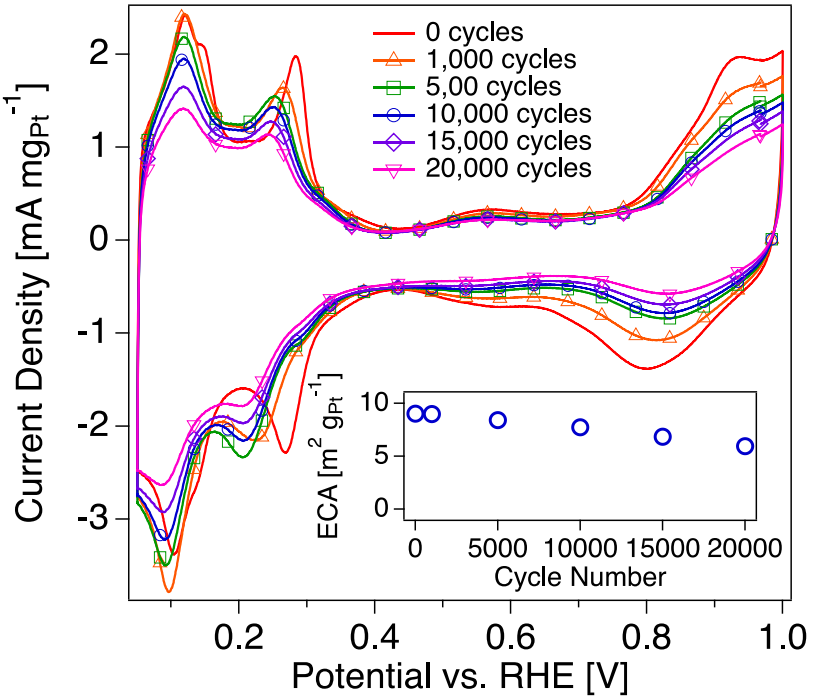

Figure 2.7. Rotating disc electrode cyclic voltammograms of annealed PtNTs recorded at 20 mV/s in 0.1 M HClO4 at 25°C at regular intervals during cycling from 0.6 V to 1.0 V at 50 mV/s. Inset shows ECA plotted against cycle number.

Though ionomer-free electrodes are possible in ex situ RDE evaluations of catalyst activity, unsupported ETFECs typically require dispersal within a porous electrode matrix that can provide for proton transport and gaseous reactant delivery. Recent RDE experiments have also shown that Nafion is not accurately classified as a non-adsorbing electrolyte in the case of low-index Pt crystals or polycrystals,[107] and can impact catalysis at supported Pt.[97] To evaluate the effects of ionomer on PtNT ORR activity, ionomer content in a series of electrode inks was varied systematically in water-based dispersions of annealed PtNTs. The effects of ionomer addition on specific activity and ECA are shown in Figure 2.8. PtNT specific ORR activity drops rapidly with the addition of small amounts of Nafion, stabilizing near 1500 $\mu A/cm^2_{Pt}$, while ECA drops monotonically with ionomer addition.

These results are in some contrast with the effects observed in the case of Pt/HSC. In that study,[97] ionomer addition to Pt/HSC caused drops of specific and mass activity of similar relative magnitude to those observed here, but ECA values were unaffected. This suggests that the deleterious effect of ionomer addition on PtNT properties is in part a function of a reduced ECA, since very small amounts of ionomer will exceed typical ionomer film thicknesses found in carbon-containing catalyst layers which are approximately 1 nm to 2 nm. We expect ionomer film thicknesses of more than 10 times this value in the case of similar quantities of ionomer addition to PtNT inks, based on the difference in

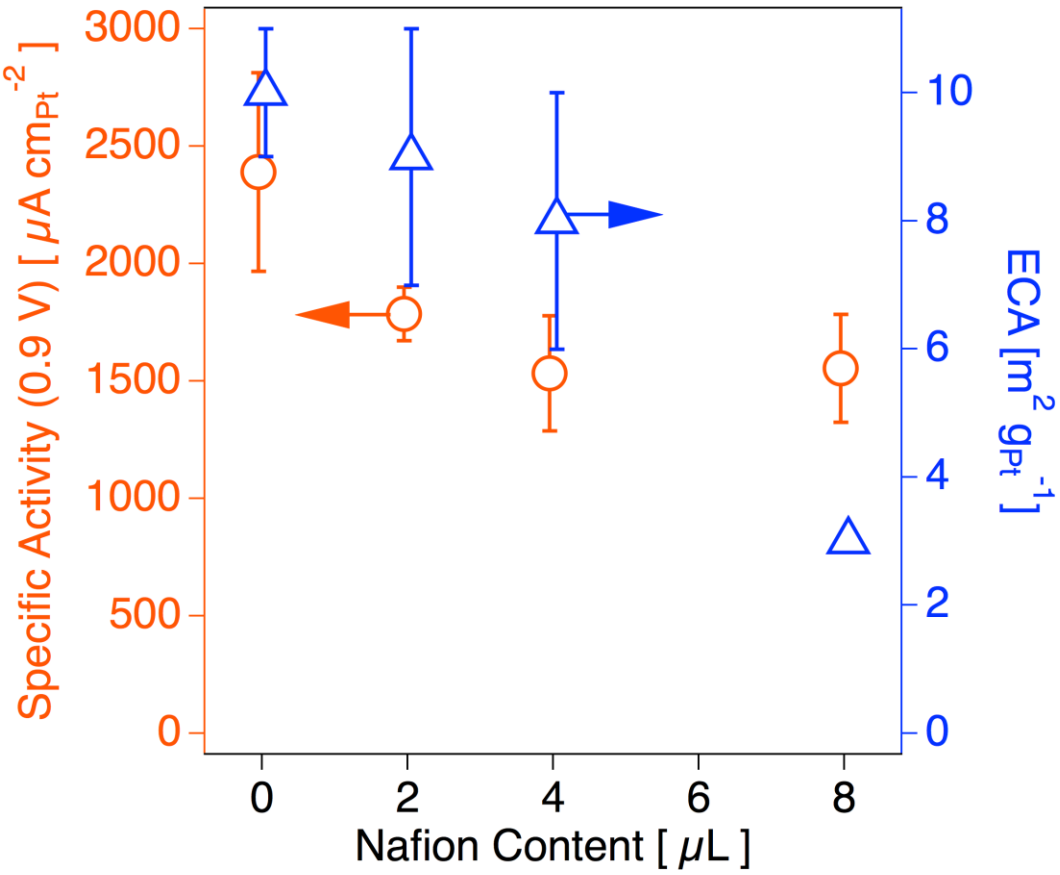

Figure 2.8. The effects of Nafion addition on specific activity and ECA of porous PtNTs annealed at 500°C.

ECA between Pt/C and PtNTs. An order of magnitude is the minimum increase, of course, since film thickness should depend on physical surface area, and the presence of carbon can increase the total surface area considerably. The addition of significant amounts of carbon to ionomer-free PtNT inks had no effect on ECA or activity,[108] so it is likely that this route may partially arrest the effects of the ionomer on annealed PtNT ORR activity.

Conclusion

We have demonstrated a novel synthesis route to supportless platinum nanotubes via the decomposition of platinum acetylacetonate vapor within anodic alumina templates at 210°C. Annealing of the Pt-bearing templates at 500°C before template dissolution results in an increase of the mean PtNT crystallite size from 3 nm to 15 nm.

The electrochemical surface area of the PtNTs was unchanged by annealing, remaining approximately 10 m^2/g_{Pt} for both samples, a value in agreement with estimates of the geometrical surface area of the catalysts. In rotating-disc electrode experiments based on ionomer-free inks, the annealed structures display an extraordinary specific activity for oxygen reduction that is on par with polycrystalline Pt.

The addition of Nafion to the water-based PtNT inks results in a decrease of specific activity and electrochemical surface area. In an actual PEMFC MEA, PtNT catalysts would be incorporated in composite electrodes by mixture with

corrosion resistant carbon materials to yield thick catalyst layers that are resistant to flooding at high current densities. The inclusion of high surface area carbon materials is also likely to mitigate the effects of the ionomer on activity by increasing the available surface area and consequently decreasing the mean ionomer film thickness.

CHAPTER 3

VAPOR SYNTHESIS AND THERMAL MODIFICATION OF SUPPORTLESS PLATINUM-RUTHENIUM NANOTUBES AND APPLICATION AS METHANOL ELECTROOXIDATION CATALYSTS

A version of this chapter was originally published in ACS Applied Materials & Interfaces:

Atkinson, III, R. W.; Unocic, R. R.; Unocic, K. A.; Veith, G. M.; Zawodzinski, Jr., T. A.; Papandrew, A. B. Vapor Synthesis and Thermal Modification of Supportless Platinum-Ruthenium Nanotubes and Application as Methanol Electrooxidation Catalysts. *ACS Appl. Mater. Interfaces* **2015**, *7*, 10115–10124.

Abstract

Metallic, mixed-phase, and alloyed bimetallic Pt-Ru nanotubes were synthesized by a novel route based on the sublimation of metal acetylacetonate precursors and subsequent vapor deposition within anodic alumina templates. Nanotube architectures were tuned by thermal annealing treatments. As-synthesized nanotubes are composed of nanoparticulate, metallic platinum and hydrous ruthenium oxide whose respective thicknesses depend on the sample chemical composition. The Pt-decorated, hydrous Ru oxide nanotubes may be thermally annealed to promote a series of chemical and physical changes to the nanotube structures including alloy formation, crystallite growth and morphological evolution. Annealed Pt-Ru alloy nanotubes and the as-synthesized analogs demonstrate relatively high specific activities for the oxidation of methanol. As-synthesized, mixed-phase Pt-Ru nanotubes (0.39 mA/cm^2) and

metallic alloyed $Pt_{64}Ru_{36}$NTs (0.33 mA/cm^2) have considerably higher area-normalized activities than PtRu black (0.22 mA/cm^2) at 0.65 V vs. RHE.

Introduction

Unsupported, high-aspect ratio nanostructured catalysts, or extended surface catalysts, remain promising candidates as oxygen reduction and alcohol oxidation catalysts for fuel cells. These extended surface catalysts usually demonstrate higher specific activities[31,98] compared to zero-dimensional nanoparticle counterparts due to unique anisotropic, electronic, surface and structural properties.[21,109] One-dimensional nanostructures are less susceptible to the common degradation modes of conventional carbon-supported nanoparticle catalysts in an operational fuel cell such as carbon support corrosion, nanoparticle dissolution, aggregation and Ostwald ripening.[40,110,111] These anisotropic catalysts typically feature lower crystal defect populations, minimizing the surface energies of the structures.[14–16] As a result, extended surface catalysts are less vulnerable than small nanoparticles to dissolution and ripening.[14,15,35,36] High-aspect ratio extended catalysts could circumvent the need for a carbon support, and subsequently devices based on this motif would not be constrained by problems related to carbon corrosion or oxidation.[23,40,41]

Numerous synthetic strategies whose complete review would exceed the scope of this introduction have been reported for the production of high-quality, anisotropic, metallic nanostructures. Each technique bears its own strengths and

limitations.[14,15] Galvanic displacement has been used to synthesize noble metal-decorated, or completely displaced, metal templates of arbitrary shape by the replacement of the template metal with a more noble metal.[24,112] The nobility of the selected metals restricts the sequencing of layered materials, and residual amounts of common template metals are susceptible to dissolution, migration, and adverse plating during fuel cell operation.[41] Atomic layer deposition (ALD) allows for the precise control of film thickness with the ability to produce alternating layers of atomically precise films, but in some cases requires post-processing to remove undesired impurities,[113] and like chemical vapor deposition, the equipment required is prohibitively expensive. Physical vapor deposition (PVD) has also been used for thin film deposition, but line-of-sight issues limit the technique for conformal film deposition on substrates with high-aspect ratio shapes. Though colloidal and other solution-based methods do not require an expensive apparatus for synthesis, surfactants that may be used for shape control can adsorb strongly to the catalyst surface blocking active sites for the intended reaction, requiring additional processing steps prior to use.[15,114–116]

In light of the limitations of some other techniques used to synthesize extended nanostructures, we have established an alternative process for developing monometallic, discretely layered bimetallic, and alloyed bimetallic nanotubes based on a modified chemical vapor deposition (CVD) method that does not require the expensive instrumentation required for conventional CVD.[50–

[52] Metalorganic precursors are decomposed by heat treatment in a vacuum oven below 250°C to deposit conformal nanoparticle films along the channels of a porous anodic alumina (AAO) membrane. Unlike galvanic displacement, metals may be deposited in any order, and the initial deposition of a metal has been observed to seed the subsequent vapor deposition of the second metal within the template. Following metal impregnation, the thermally stable AAO templates may be annealed in various gas environments to induce phase transitions, morphological evolution, alloy formation and grain growth. The ability to control grain growth by adjusting the temperature of the heat treatment is a valuable asset of this post-synthesis annealing technique considering the influence of particle size on activity, well-known in the case of oxygen reduction in acidic media,[42,68] and recently shown to have an impact on hydrogen oxidation in alkaline conditions.[56] Following thermal treatment, the nanotubes may be recovered by dissolution of the sacrificial template. We have previously vapor deposited porous platinum nanotubes using this technique that demonstrated very high specific activity, comparable to bulk polycrystalline platinum, for the oxygen reduction reaction.[117] Here, we demonstrate the extended capacity of this vapor deposition method for the synthesis and thermal evolution of bimetallic nanostructures by detailing the synthesis of platinum-ruthenium nanotubes.

To date, platinum-ruthenium catalysts have been the preferred choice of anode catalyst for direct methanol fuel cells (DMFCs).[2] Pt is a highly active

catalyst for the oxidation of methanol and it is considered to sequentially dehydrogenate the methyl group until an adsorbed carbon monoxide remains on the Pt surface.[118] In order to remove adsorbed CO from Pt sites on bare Pt catalysts, oxygen-containing species like hydroxide must form on adjacent sites to oxidize CO_{ads} to CO_2.[119–122] The formation of oxygen-containing species on Pt is delayed until high potentials, leaving Pt surfaces blocked by adsorbates beyond the desirable window for DMFC operation.[65] In the presence of ruthenium in a PtRu alloy, Pt sites adsorb and dehydrogenate methanol to CO_{ads}, and this site-blocking intermediate is oxidized by the oxygen-containing species that form on Ru.[95,118,123,124] Ruthenium is more effective at transferring surface oxygen than Pt because it adsorbs water at lower potentials than Pt.[125] This process of methanol dehydrogenation by Pt and subsequent carbon monoxide oxidation from oxygen-containing species adsorbed on Ru in a Pt-Ru alloy is known as the bi-functional mechanism.[95,118,123]

Metallic PtRu alloys have been the most well-studied DMFC anode catalyst,[2] but other promising mixed-phase Pt-Ru catalysts have emerged featuring the hydrous oxide phase of Ru (RuO_xH_y) with metallic Pt. The promotional effects of Ru on Pt for CO oxidation are closely linked to its oxidation state. The hydrous oxide of Ru weakens the Pt interaction with CO while providing OH adsorption locations for CO oxidation.[126] The presence of the hydrous oxide as the exclusive Ru species in a Pt-Ru catalyst was shown to

enhance methanol oxidation activity by two orders of magnitude compared to the metallic and anhydrous forms.[95] The methanol oxidation activity enhancement by hydrous ruthenium oxide has been attributed to its mixed valence, ability to conduct protons and electrons, and its natural expression of Ru-OH.[95] The hydrous oxide of Ru efficiently dissociates water,[95] implying that a methanol oxidation catalyst containing this material could oxidize site-blocking intermediates effectively.

This work showcases the potential of this metalorganic vapor deposition technique by detailing the synthesis of two distinct types of platinum-ruthenium nanotubes. In the as-synthesized case, nanotubes are synthesized with walls composed of a nominally layered structure comprising an interior bulk hydrous Ru oxide and exterior metallic Pt. In this catalyst motif, which has been deployed previously with different extended nanostructures and materials for other reactions,[22,46,49,91–93] catalytically active Pt decorates the surface of the nanotube and is highly utilized while the more abundant and less expensive Ru provides structural support composing the wall interiors. In the second case, the layered Pt-Ru nanotubes are annealed while still within the template to reduce the hydrous oxide to metallic Ru, and to promote nanotube wall porosity, grain growth and Pt-Ru alloy formation. In each case, the template is etched away to yield unsupported, dispersed nanotube suspensions.

Experimental

Platinum-Ruthenium Nanotube Synthesis Platinum-ruthenium nanotubes were synthesized by consecutive vapor deposition experiments, each consisting of the deposition of one metal species. Platinum was deposited first, followed by deposition of ruthenium, within the pores of an anodic alumina (AAO) membrane (Whatman Anodisc, 13 mm diameter, 200 nm pore size). A powder of platinum(II)(2,4)-pentanedionate (Alfa Aesar), or platinum acetylacetonate, was contained beneath the porous alumina template and transferred to a vacuum oven with a glass vial containing 2.3 mL of DI water. The oven was evacuated with a rotary vane vacuum pump and purged with dry N_2 several times before finally being evacuated to 0.3 bar and sealed. The oven thermostat was set to a calibrated value of 180°C. The liquid water was vaporized and equilibrium was reached after 75 minutes at a total pressure of 0.8 bar, as measured by a Bourdon gauge. The oven was evacuated after 15 hours at 180°C, flushed with dry N_2, and cooled to room temperature before the Pt-bearing template was recovered, and the mass of Pt deposited during this first step of the synthesis was measured.

The above procedure for platinum deposition was repeated at an elevated temperature for the deposition of ruthenium within the Pt-seeded template. Hydrous ruthenium oxide [$Ru(O_xH_y)$] was deposited along the Pt-lined channels of the alumina template from the decomposition of ruthenium(III)2,4-

pentanedionate at 240°C. By adjusting the masses of the respective precursor doses, the masses of Pt and $Ru(O_xH_y)$ that were deposited sequentially were controlled, from which the nanotube sample composition was determined.

The platinum and hydrous ruthenium oxide-filled templates were then immediately dissolved or thermally annealed to induce morphological and chemical phase changes and alloy formation. The sample templates were annealed in a quartz tube furnace with a flowing H_2 (4% hydrogen, balance argon) mixture. After purging the furnace tube for 30 minutes, the templates were heated at 750°C for 1 hour before allowed to cool passively to room temperature.

To liberate the nanotubes for further study, the sacrificial alumina templates were dissolved by magnetic stirring in 30% KOH solution at room temperature for 90 hours. The supernatant solution was then decanted and replaced with de-ionized water; a process that was repeated until the pH of the supernatant solution was neutral. A variety of materials characterization techniques were then used to analyze the structure, morphology, and chemistry of the as-synthesized and heat-treated nanotubes.

Electron Microscopy Scanning electron microscopy (SEM) images were acquired using a ZEISS 1525 Field Emission SEM using an accelerating voltage of 3 kV and an in-lens electron detector. SEM-EDS measurements of nanotube chemical compositions were acquired at an accelerating voltage of 20 kV. A Hitachi NB-5000 focused ion beam (FIB) instrument was used to prepare thin

TEM cross-sections of samples still in the AAO template for scanning transmission electron microscopy (S/TEM) imaging and EDS mapping using a JEOL 2200FS operating at 200 kV. High-resolution (HRTEM) images were acquired on these FIB-derived lamellae using a FEI Titan S/TEM operating at 300 kV.

X-ray photoelectron spectroscopy (XPS) data were collected using a PHI 3056 spectrometer with an Al anode source operated at 15KV and an applied power of 350 W. No charge correction was required or applied. High resolution data was collected at a pass energy of 23.5 eV with 0.05 eV step sizes and a minimum of 50 scans to improve the signal to noise ratio; lower resolution survey scans were collected at a pass energy of 93.5 eV with 0.5 eV step sizes and a minimum of 20 scans.

X-ray diffraction (XRD) patterns were measured with a Bruker D2 Phaser diffractometer with Cu Kα radiation (λ = 0.1541874 nm, 30 kV, 10 mA, 0.014° step, 0.5 s/step).

X-ray absorption spectroscopy X-ray absorption near-edge spectra (XANES) data were acquired at beamline X11A of the National Synchrotron Light Source (NSLS) at Brookhaven National Laboratory. Spectra were obtained in transmission mode at the Ru K edge, using a Si(111) double crystal monochromator with a 10% detuning and gas ionization chambers for beam intensity monitoring. Nanotube samples were drop cast on Kapton discs from

aqueous solution and dried in air. A 325 mesh Ru powder and PtRu black (Alfa Aesar) were used as control samples. All measurements were conducted at room temperature in air. Data analysis was performed using the iXAFS software suite.

Electrochemistry Measurements Electrode inks were prepared for electrochemistry experiments by diluting the nanotube-water suspensions to concentrations ranging from 0.25 – 0.50 mg_{PtRu} mL^{-1}. No alcohol or ionomer was added to the inks. The unsupported platinum-ruthenium nanotubes were deposited on the working electrode with loadings of 25-60 μg_{PtRu} cm^{-2}_{elec}.

Cyclic voltammetry (CV) measurements were performed in a glass electrochemical cell with a glassy carbon (GC) working electrode, platinum wire counter electrode, and an Hg/Hg_2SO_4 (0.5 M H_2SO_4) reference electrode. All potentials reported in this work are referred to a reversible hydrogen electrode (RHE) by calibration of the reference electrode versus a Pt electrode in hydrogen-saturated electrolyte. Prior to applying catalyst inks to the GC electrode, solids in the inks were dispersed by sonication in an ice bath for 20 minutes. A 10 µL aliquot of catalyst ink was applied to the GC and allowed to dry in air at room temperature.

Prior to each experiment, the electrolyte was deoxygenated by purging with ultrahigh purity N_2 gas for at least 30 minutes. The electrodes were conditioned at the start of each experiment with 15 cycles in 0.5 M H_2SO_4 (Alfa

Aesar, 99.9999% metals basis) from 0.05 V to 0.70 V vs. RHE at 100 mV s^{-1}. Subsequent to conditioning, three additional cycles were recorded at 20 mV s^{-1}.

Pure ruthenium electrodes, and also Pt-Ru alloys, report inaccurately low electrochemically active surface area (ECSA) when hydrogen underpotential deposition (HUPD) is used in place of other more appropriate techniques. In addition to adsorbing hydrogen, Ru electrodes also absorb hydrogen, adsorb oxygen species and evolve hydrogen in the same potential range, making it difficult to distinguish the charges associated with each process and obtain an accurate ECSA measurement from HUPD.[127] Carbon monoxide (CO) stripping voltammetry was performed in 0.5 M H_2SO_4. The electrolyte was saturated with CO and a potential of 0.1 V was applied to the working electrode to adsorb CO. The applied potential was maintained while purging the electrolyte with 4% CO (balance Ar) for an additional 10 minutes followed by purging with nitrogen for 30 minutes. CO stripping voltammograms were recorded in the nitrogen-purged electrolyte at 20 mV s^{-1}. Sample ECSA was calculated using the charge for removing a monolayer of CO from a Pt surface (420 μC cm^{-2}).[128]

Methanol oxidation reaction (MOR) activity was measured by cycling the electrode in fresh 0.5 M CH_3OH (Fisher Scientific, HPLC grade) and 0.1 M H_2SO_4 from 0.05 V to 1.2 V vs. RHE at 20 mV s^{-1}. ECSAs obtained during CO stripping voltammetry were used to normalize methanol oxidation linear sweep voltammograms to catalyst surface area. Platinum-ruthenium black (Alfa Aesar,

nominally 50% atomic Pt) was used to benchmark the performance of the experimental catalysts. Catalyst ink and electrodes prepared with the commercial catalyst follow the procedures outlined above for the experimental catalysts.

Results and Discussion

Representative SEM images of as-synthesized Pt-decorated, hydrous Ru oxide nanotubes [PtRu(O_xH_y)NTs] and annealed, alloyed platinum-ruthenium nanotubes (PtRuNTs) are presented in Figure 3.1. In each case, the initial deposition of Pt nanoparticles within the anodic alumina template lined the template channels before a successive layer of hydrous Ru oxide was deposited, which would become the interior of the nanotube upon dissolution of the template. Individual nanotubes maintained similar morphologies from the shapes of the pores of the templates in which the metals were vapor-deposited. The nanotube cross-sections are roughly circular and approximately 200 nm in diameter with lengths ranging from 2 to 50 μm.

Owing to the conformal nature of the initial Pt deposit within the channels of the alumina template, the exterior surfaces of the as-synthesized nanotubes are uniform with no noticeable porosity. The interiors of the nanotubes are composed of a conformal hydrous Ru oxide layer that was vapor-deposited on the interiors of the Pt-lined AAO channels in a second vapor deposition step. The

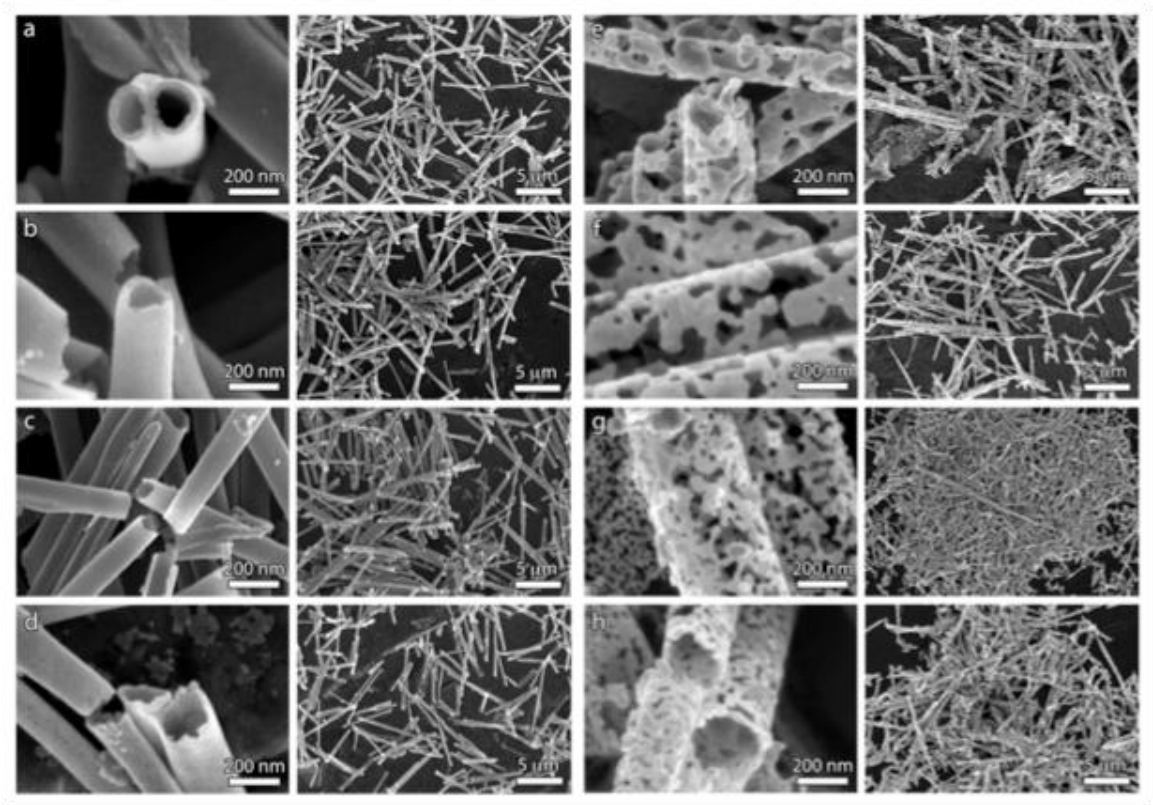

Figure 3.1. SEM images of as-synthesized $PtRu(O_xH_y)$NTs (a) 10% Pt, (b) 17% Pt, (c) 38% Pt, (d) 64% Pt, and PtRuNTs annealed at 750°C in 4% H_2 (e) 9% Pt, (f) 20% Pt, (g) 47% Pt, (h) 60% Pt.

respective thicknesses of the Pt and Ru(O_xH_y) layers vary with the amounts of each material deposited during synthesis and are controlled in order to achieve nanotubes of desired chemical compositions. Following a heat treatment at 750°C for 1 hour in 4% H_2, the PtRuNTs in Figure 3.1(e-h) displayed structural and chemical evolution. The initially nanoparticulate and finely-textured Pt exterior of the PtRu(O_xH_y)NTs evolved to a more coarsely grained, highly porous, and smooth surface. The more Pt-rich, alloyed nanotubes [Figure 3.1(g-h)] experienced less grain growth than the Ru-rich nanotubes, resulting in tube walls with a finer, filigree-like structure rather than the globular bead-like walls of the Ru-rich Pt_9Ru_{91}NTs in Figure 3.1(e). The differences in the observed mesostructures with varying Pt-Ru content may be influenced by disparities in self-diffusion rates in the nanostructured walls and the energetics of the nanotube surface interaction with the AAO template.

To better understand the structural and chemical evolution of the nanotubes from the as-synthesized PtRu(O_xH_y)NTs to the annealed PtRuNTs, cross sections were prepared from 58% Pt nanotubes that were left intact and within the Al_2O_3 template. Figure 3.2 shows representative HAADF STEM images and EDS elemental mapping of the nanotubes within the AAO pore walls for the as-synthesized PtRu(O_xH_y)NTs [Figure 3.2(a-f)] and PtRuNTs following heat treatment at 750ºC [Figure 3.2(g-l)].

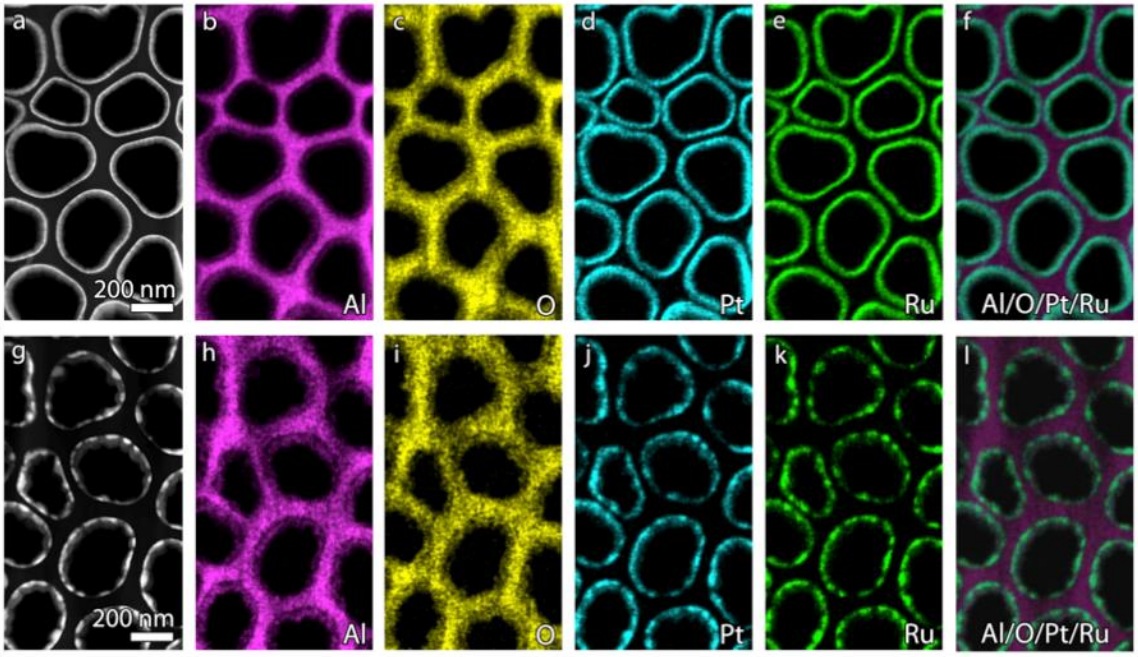

Figure 3.2. HAADF STEM and EDS elemental mapping of (a-f) as-synthesized $Pt_{58}Ru_{42}(O_xH_y)$NTs and (g-l) annealed, alloyed $Pt_{58}Ru_{42}$NTs at 750ºC in 4% H_2 for 1 hour. Cross sections were observed by leaving the nanotubes embedded within the sacrificial AAO template.

For the case of the as-synthesized $PtRu(O_xH_y)$NTs, HAADF STEM imaging [Figure 3.2(a)] and EDS mapping show the elemental distribution of Al and O in the Al_2O_3 pore walls [Figure 3.2(b-c)] and the conformal coatings of Pt [Figure 3.2(d)] and Ru [Figure 3.2(e)] that line the Al_2O_3 pore walls. Moreover, the composite STEM-EDS map [Figure 3.2(f)] shows a thin layer of elemental Pt at the Al_2O_3 pore wall interface, which is to be expected, since platinum was first deposited within the Al_2O_3 pore walls prior to Ru deposition.

Following heat treatment at 750ºC for 1 hour in 4% H_2, the morphology of the PtRuNT no longer remains conformal, rather the PtRuNT coating along the Al_2O_3 pore wall is highly non-uniform as can be seen in the HAADF STEM image in Figure 3.2(g), which can be correlated with the porous nature of the PtRuNT following heat treatment that is observed in Figure 3.1(e-h). There is no indication of elemental segregation between Pt [Figure 3.2(j)] and Ru [Figure 3.2(k)] along the Al_2O_3 pore wall [Figure 3.2(h-i)], indicating that Pt and Ru alloyed during exposure to the 4% H_2 environment at 750ºC.

Further characterization of the nanotubes can be seen in high-resolution TEM (HRTEM) images in Figure 3.3. For the as-synthesized $PtRu(O_xH_y)$NTs, the TEM images in Figure 3.3(a-b) further reveal the conformal coating nature of the nanotube while still in the Al_2O_3 template, but also show the amorphous layer of $Ru(O_xH_y)$ deposited onto Pt nanoparticles that line the walls of the template

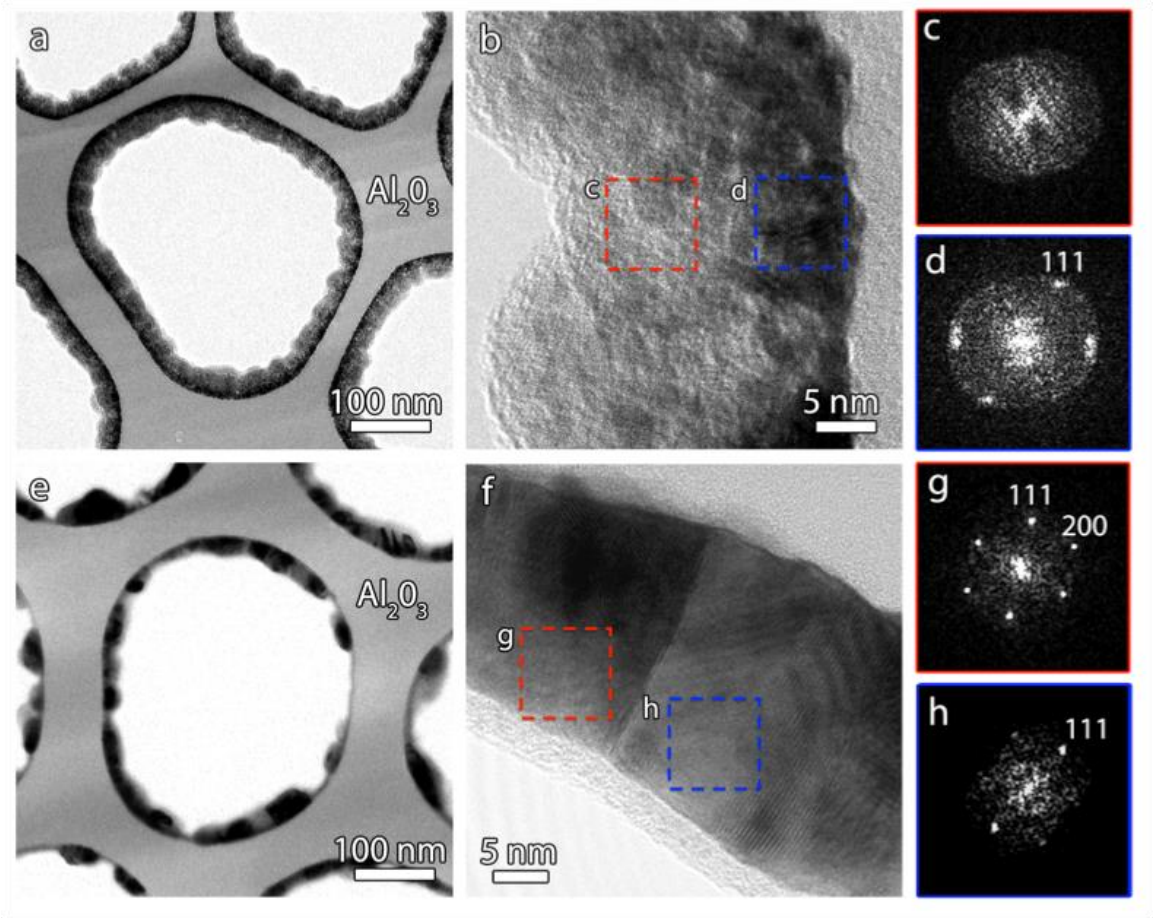

Figure 3.3. TEM images of the (a-b) as-synthesized $Pt_{58}Ru_{42}(O_xH_y)$NTs showing the amorphous $Ru(O_xH_y)$ layer on nanocrystalline Pt lining the Al_2O_3 pore walls. FFT analysis from the boxed regions in (b) correspond to (c) amorphous $Ru(O_xH_y)$ and (d) crystalline Pt. The TEM images in (e-f) are from the annealed $Pt_{58}Ru_{42}$NTs and show PtRu nanocrystals. FFT analyses from the boxed regions in (f) correspond to (g) a PtRu crystal oriented along the [011] zone-axis and (h) (111) lattice planes.

channels, which is confirmed through FFT analysis in Figure 3.3(c-d), respectively.

Following heat treatment at 750ºC for 1 hour in 4% H_2 [Figure 3.3(e-h)], the TEM images reveal how $PtRu(O_xH_y)$ is transformed into individual, PtRu nanocrystals, as shown in Figure 3.3(e-f). FFT analysis from the boxed regions in Figure 3.3(f) reveals that the structures of the PtRu crystals have a face centered cubic crystal structure. The FFT in Figure 3.3(g) shows a region of the crystal that is oriented along the [011] zone axis and the crystal to the right [Figure 3.3(h)] shows (111) lattice planes.

The observed increase in grain size induced by the heat treatment is confirmed by Scherrer analysis of the X-ray diffraction patterns in Figure 3.4. The as-synthesized nanotubes [Figure 3.4(a)] contain relatively broad face-centered cubic (fcc) peaks in comparison to the annealed $Pt_{64}Ru_{36}$NTs [Figure 3.4(e)] of the same composition. Scherrer widths of the Pt(111) peaks for the two samples were calculated to quantify the change in grain size and an increase in grain size from 4.1 nm to 11.8 nm in the annealed sample was observed.

The diffraction pattern of as-synthesized $Pt_{64}Ru_{36}(O_xH_y)$NTs [Figure 3.4(a)] only contains peaks corresponding to the fcc geometry of the Pt unit cell. At low Pt content, the as-synthesized nanotubes are dominated by the amorphous phase of hydrous Ru oxide, and no noticeable peaks are present in the diffraction patterns as a result. At higher Pt content, fcc peaks emerge at values of 2θ

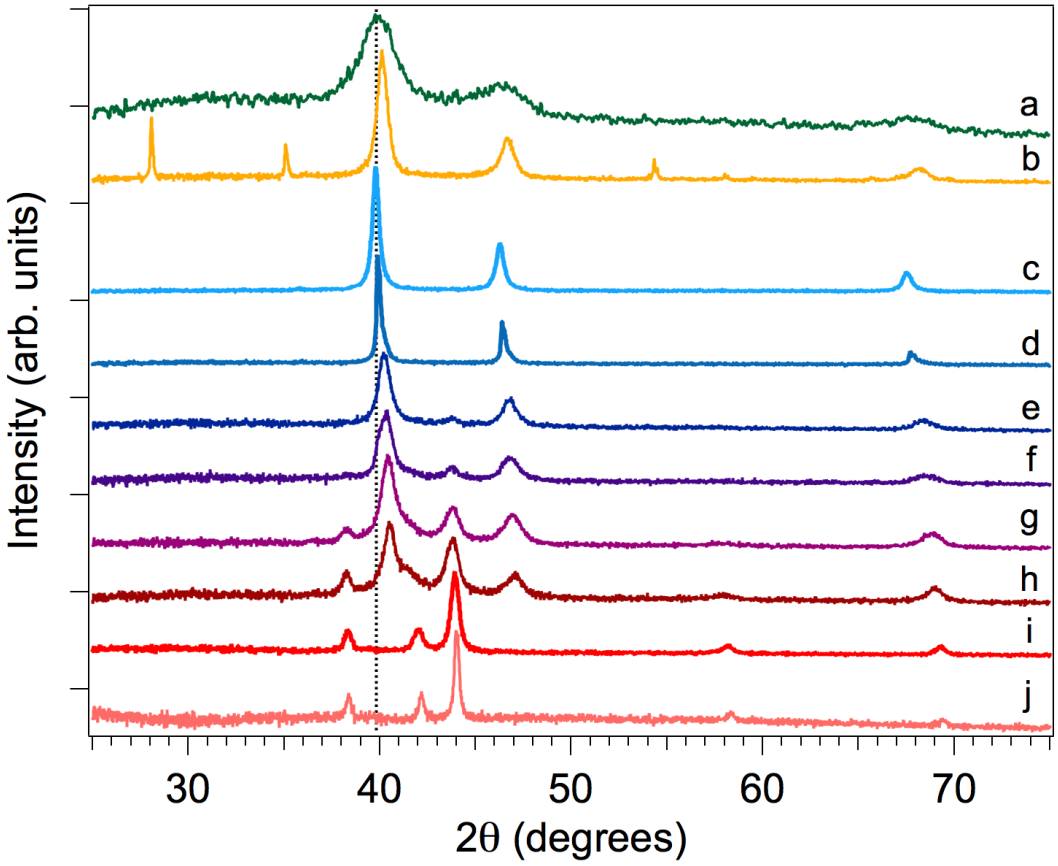

Figure 3.4. Cu Kα X-ray diffraction patterns of as-synthesized (a) $Pt_{64}Ru_{36}(O_xH_y)$NT, annealed (b) $Pt_{60}Ru_{40}O_x$NT at 750°C in N_2, and annealed at 750°C in H_2 (c) PtNT, (d) $Pt_{80}Ru_{20}$NT, (e) $Pt_{64}Ru_{36}$NT, (f) $Pt_{60}Ru_{40}$NT, (g) $Pt_{43}Ru_{57}$NT, (h) $Pt_{38}Ru_{62}$NT, (i) Pt_7Ru_{93}NT, (j) RuNT.

consistent with pure Pt. There is no shift in the location of the Pt(111) peak that would indicate the formation of a PtRu alloy during synthesis and prior to high temperature annealing. Additional diffraction patterns for compositions of as-synthesized PtRu(O_xH_y)NTs are shown in Figure 3.5, which illustrate the amorphous nature of the as-synthesized hydrous Ru oxide nanotubes with variable Pt content. The lack of characteristic peaks for tetragonal anhydrous ruthenium oxide (RuO_2) or hexagonal close-packed (hcp) peaks of metallic Ru suggest that an amorphous hydrous oxide of Ru[94,129] was formed during synthesis. During heat treatment at 750°C in inert gas, in this case N_2, the structural water is removed and crystalline, anhydrous Ru oxide is formed [Figure 3.4(b)] exhibiting a distinct diffraction pattern from metallic Ru. In a reducing gas environment, hydrous Ru oxide was reduced to metallic Ru in our annealed, pure ruthenium nanotubes [RuNTs, Figure 3.4(j)]. Nanotubes composed of hydrous Ru oxide and metallic Ru were the focus of this study of methanol oxidation.

The diffraction patterns in Figure 3.4 indicate the formation of alloys during heat treatment at 750°C. As the composition of the annealed nanotube samples departs from monometallic Pt [Figure 3.4(c)] to feature a small amount of Ru [Figure 3.4(d)], the Pt(111) peak shifts to higher values of 2θ; the Pt lattice contracts as Ru, with smaller atomic radius than Pt, substitutes into the Pt lattice.[130] The dashed line in Figure 3.4 corresponds to the lattice parameter of the Pt(111) peak in bulk polycrystalline platinum. The lattice contraction of the

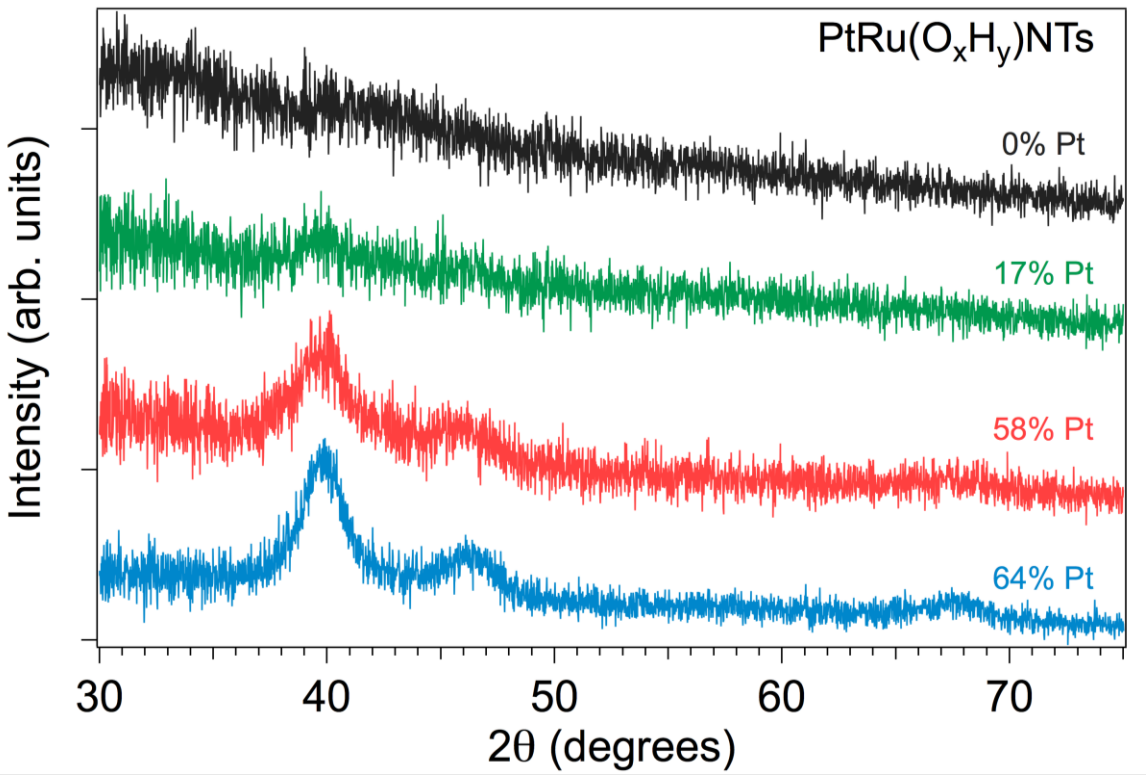

Figure 3.5. Cu Kα X-ray diffraction patterns of as-synthesized $Ru(O_xH_y)NTs$ and as-synthesized $PtRu(O_xH_y)NTs$ with variable Pt content.

PtRuNTs increased with the increase in Ru content [Figure 3.4 (d-i)]. In nanotube samples with Ru composition between 36-62%, the formation of a dual-phase alloy is observed. Characteristic hcp peaks of metallic Ru emerge and intensify with increasing Ru content in the nanotubes. The formation of fcc and hcp alloy phases at compositions closer to a 1:1 atomic ratio of Pt to Ru are believed to be a result of the relatively thick layers of Pt and hydrous Ru oxide sequentially deposited to compose the nanotube walls during synthesis that are discernible in the HAADF STEM and TEM images of the as-synthesized $Pt_{58}Ru_{42}(O_xH_y)$NTs. When the Ru composition is increased to 93% [Figure 3.4(i)], a homogeneous PtRu alloy is formed as evidenced by the pure hcp phase. In this case, the Pt layer at the nanotube exterior is assumed to be very thin and all Pt present has diffused into the Ru lattice.

A more detailed probing of nanotube chemical composition and the transformations induced during the heat treatment are possible using XPS analysis. A composition near the midpoint of the examined range was selected ($Pt_{59}Ru_{41}$). As-synthesized and heat-treated samples of this composition were drop-cast from water solutions on Si wafers after dissolution of the AAO template. PtRu black was similarly prepared. High-resolution XPS scans of the Pt 4f doublet and the Ru $3p_{3/2}$ peak, along with peak deconvolution components derived via nonlinear, least-squares fitting, are shown in Figure 3.6. In both of the experimental nanotube samples, Pt is present almost entirely as metallic Pt, with

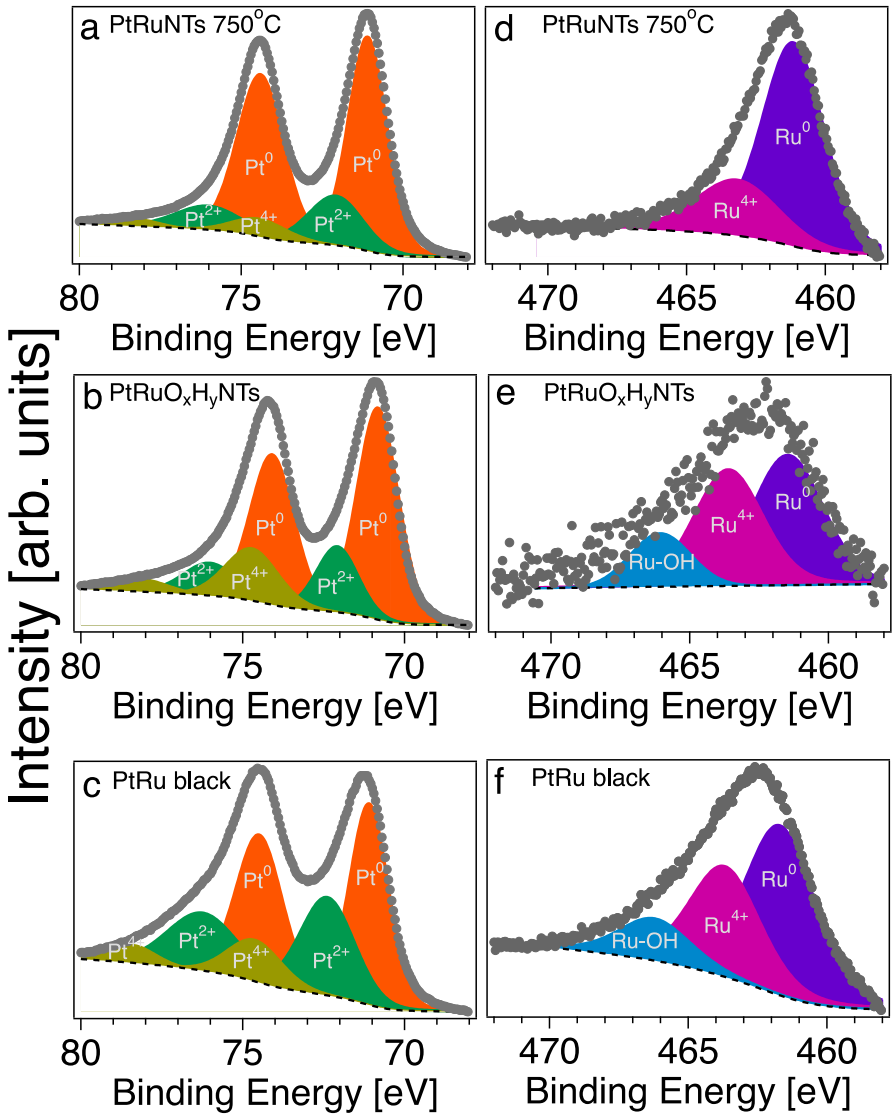

Figure 3.6. High resolution XPS spectra of the Pt 4f doublet (a-c) and the Ru $3p_{3/2}$ peak (d-f) for (a, d) 750°C, 4% H_2-annealed $Pt_{59}Ru_{41}$NTs (b, e) as-synthesized $Pt_{59}Ru_{41}(O_xH_y)$NTs, and (c, f) PtRu black.

a small amount of Pt^{4+} discernible. The PtRu black sample exhibits more oxidized Pt, clearly visible in the elevation of the Pt $4f_{5/2}$ above the Pt $4f_{7/2}$ peak in Figure 3.6(c).

Ru is present primarily as metallic Ru in the annealed nanotube sample, with a small amount of Ru^{4+} present, presumably as RuO_2. The presence of this oxide can be inferred from the HRTEM images in Figure 3.3(f), which show what may be a 1-2 nm oxide film on the tube interior. Some degree of oxidation is also inferred from edge shifts observed in Ru K-edge XANES in Figure 3.7. In the case of the as-synthesized nanotube sample, the Ru signal was of very low intensity and thus exhibited significant noise in Figure 3.6(e). In addition to any chemical information, then, we are also able to infer supporting structural information from the low intensity of this peak. As we observed in our HRTEM investigations, Ru is initially confined to the nanotube interiors. In the case of moderate Pt content, Pt dominates the outer surfaces of the nanotubes that have been freed from the AAO template, and acts to absorb the scattered Ru photoelectrons. The surface composition measured via XPS peak areas adjusted via the appropriate atomic adsorption factors was approximately 10:1 Pt:Ru in the case of the as-synthesized sample. Using the same analysis of the annealed sample returned the nominal composition measured via EDS.

Deconvolution of the as-synthesized Ru $3p_{3/2}$ peak found almost equal amounts of metallic Ru and Ru^{4+} species, with approximately 15% of the total

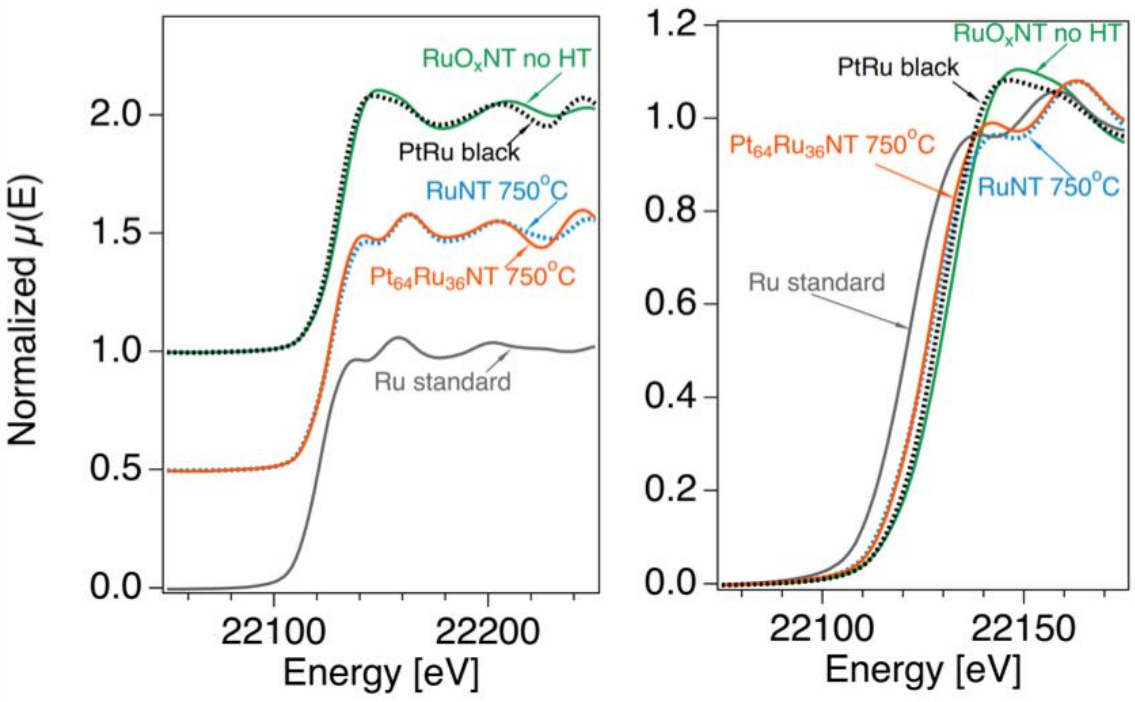

Figure 3.7. XANES data at the Ru K edge of selected synthesis products and commercial PtRu black.

observable Ru present as RuO_xH_y-type species. However, we stress that this is not the overall Ru chemical composition but rather the Ru species located closest to the walls of the tubes. Analysis of the PtRu black Ru $3p_{3/2}$ peak reveals a similar 1:1 balance of metallic to Ru^{4+} species, though 30% of the Ru in this case is present as Ru hydrates.

The XANES spectra of the experimental materials are grouped with the standard materials sharing the same spectral characteristics in the left panel of Figure 3.7. The XANES data for the annealed nanotube samples supports observations from XPS about the presence of metallic Ru character, as the annealed nanotube samples share features of the Ru powder standard. However, in the case of these samples we find a 5 eV shift of the absorption edge that suggests the presence of oxide. From HRTEM investigations in Figure 3.3 it is probable that this is a surface phase.

The as-synthesized $Ru(O_xH_y)$NT sample shows a decidedly larger edge shift of nearly 8 eV, lacks the distinct dual peaks of metallic Ru, and nearly overlays the PtRu black standard spectrum. It is well known that commercial PtRu blacks are rich in Ru hydrous oxides[131] and in concert with the HRTEM data, this implies that Ru is present in the as-synthesized samples as amorphous $Ru(O_xH_y)*zH_2O$. We note also that during methanol oxidation, Ru oxides are likely to be at least partially reduced from the presence of methanol.[132]

In Figure 3.8A, the cyclic voltammograms in acid of as-synthesized PtRu(O_xH_y)NTs further demonstrate that ruthenium is deposited as a hydrous oxide during synthesis and prior to heat treatment. As the Ru content in the nanotubes is increased relative to Pt, the characteristic hydrogen adsorption and desorption regions (0.05 to 0.35 V vs. RHE) diminish and the capacitive features associated with the mixed-valent, hydrous oxide of Ru dominate the voltammograms.[133] The high specific capacitance observed here is attributed to the ability of hydrous ruthenium oxide to transport and store electrons and protons.[94,125] The dashed line in Figure 3.8A represents reduced, metallic ruthenium nanotubes (RuNTs).

The versatility of this synthesis technique is highlighted by Figure 3.8B, which features cyclic voltammograms of three different nanotube sample types with low Pt content, each with a unique chemical phase of ruthenium. The above-mentioned as-synthesized nanotubes that feature amorphous, hydrous Ru oxide are compared to two Pt-Ru nanotube samples that are annealed in different gas environments. The Pt and anhydrous, crystalline Ru oxide (RuO_2) nanotubes [Figure 3.8B(b)] were prepared by annealing in dry nitrogen at 750°C. Like the alloyed PtRuNTs [Figure 3.8B(c)] that feature metallic Ru after a heat treatment in 4% H_2 at 750°C, the anhydrous and crystalline ruthenium oxide is relatively featureless in the capacitive charging region in comparison to the hydrated form of the Ru oxide.

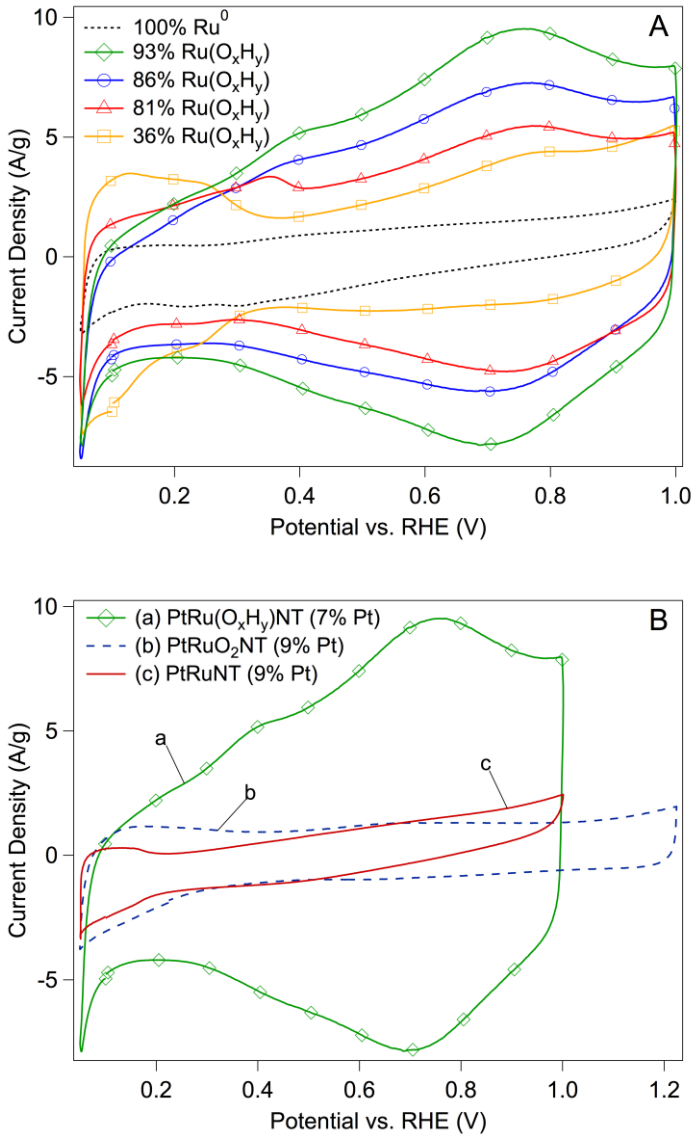

Figure 3.8. Cyclic voltammograms recorded in 0.5 M H_2SO_4 at 20 mV s^{-1}. In (A), pure and metallic RuNTs (dashed black line) which are reduced at 750°C in 4% H_2 are compared to as-synthesized $PtRu(O_xH_y)$NTs with variable Pt content. In (B), as-synthesized (a) $PtRu(O_xH_y)$NTs, (b) 750°C N_2-annealed $PtRuO_2$NTs, and (c) 750°C, 4% H_2-annealed PtRuNTs with similar Pt content are compared.

At all quantities of Pt content tested for the experimental catalysts, the as-synthesized PtRu(O_xH_y)NTs are more active than the annealed PtRuNTs. We attribute this improved performance to the high degree of Pt utilization and the presence of Ru in hydrous oxide form. Methanol oxidation specific activities of the experimental nanotube catalysts are plotted against Pt composition in Figure 3.9.

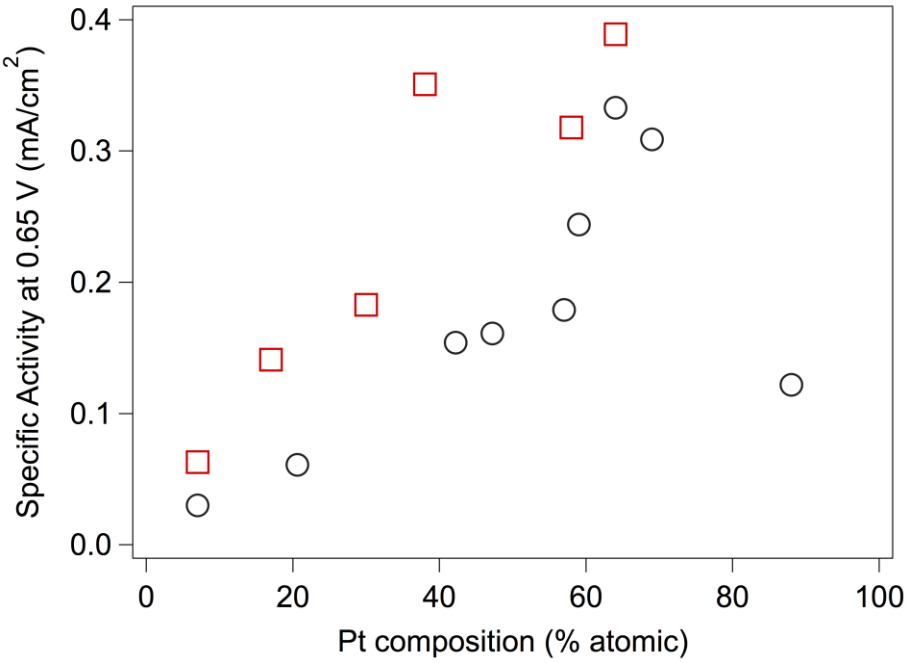

Figure 3.9. Scatter plot of specific activity vs. Pt content measured at 0.65 V vs. RHE for as-synthesized PtRu(O_xH_y)NTs (red squares) and alloyed PtRuNTs (black circles) recorded in 0.5 M CH_3OH and 0.1 M H_2SO_4.

In the as-synthesized nanotubes (Figure 3.9, red squares), it must be considered that these samples are composed of a hydrous Ru oxide interior with a discrete Pt surface layer as demonstrated in the TEM images in Figure 3.3(a-d), the latter increasing in thickness with Pt content. Therefore, the concept of Pt content must be considered differently from the alloyed PtRuNTs (Figure 3.9, black circles), where a consideration of bulk composition applies. When more Ru-rich, the specific activities of the PtRu(O_xH_y)NTs increase almost linearly with Pt content from 7% to 38% Pt as more catalytically active Pt is effectively added to the nanotube exterior in a thin and conformal Pt layer. In the more Pt-rich PtRu(O_xH_y)NTs (40-64% Pt), the core-shell design is most effective and the specific activity no longer increases with Pt content, but rather plateaus, as the nanotube exterior surfaces become more enriched with Pt, visible in the $Pt_{58}Ru_{42}$(O_xH_y)NTs in the representative HAADF STEM [Figure 3.2(a-f)] and TEM images [Figure 3.3(a-d)].

Similarly in the alloyed PtRuNTs, the specific activity increases with Pt composition until a maximum activity is observed at 64% Pt, followed by a reduction in activity in the most Pt-rich samples. We suggest that the $Pt_{64}Ru_{36}$NTs are the most active of the alloyed nanotubes because the metals that compose these nanotubes are well dispersed with a high degree of surface Pt-Ru pair sites that are required to remove methanol oxidation intermediates from the catalyst surfaces efficiently, as manifested by the CO stripping

voltammograms. Both nanotube sample types reported maximum specific activities at 64% Pt content and these particular samples have been isolated for further study. Low Pt content, as-synthesized $Pt_{17}Ru_{83}(O_xH_y)$NTs with a presumably thin Pt surface layer are also highlighted because these catalysts may serve as a better model of a core-shell design.

The charge of a respective sample's CO stripping peak was used to determine the catalyst's ECSA, and is used to normalize the mass-normalized CO stripping voltammograms in Figure 3.10A to the area-normalized voltammograms in Figure 3.10B. Commercial PtRu black [Figure 3.10(a)] is a highly dispersed alloy of Pt and Ru with high ECSA that efficiently oxidizes surface-adsorbed CO at relatively low potentials due to its high degree of metal dispersion and alloying.[95] The alloyed $Pt_{64}Ru_{36}$NT sample had an earlier onset and lower peak potential for CO oxidation than both of the as-synthesized nanotube samples, which is likely the result of an improved dispersion of Pt and Ru and the concomitant increase of bimetallic Pt-Ru pair sites. Additionally, the increased grain size of the annealed $Pt_{64}Ru_{36}$NTs is expected to promote faster CO_{ads} oxidation, likely from an increase in CO surface diffusion expected on the surface of a larger nanoparticle.[62,64,65] However, the CO stripping peak of the alloyed PtRuNT [Figure 3.10(b)] is broad and features a shoulder at higher potentials (0.77 V) that presumably corresponds to more Pt-rich regions at the surfaces of the nanotubes that are less active for CO oxidation.

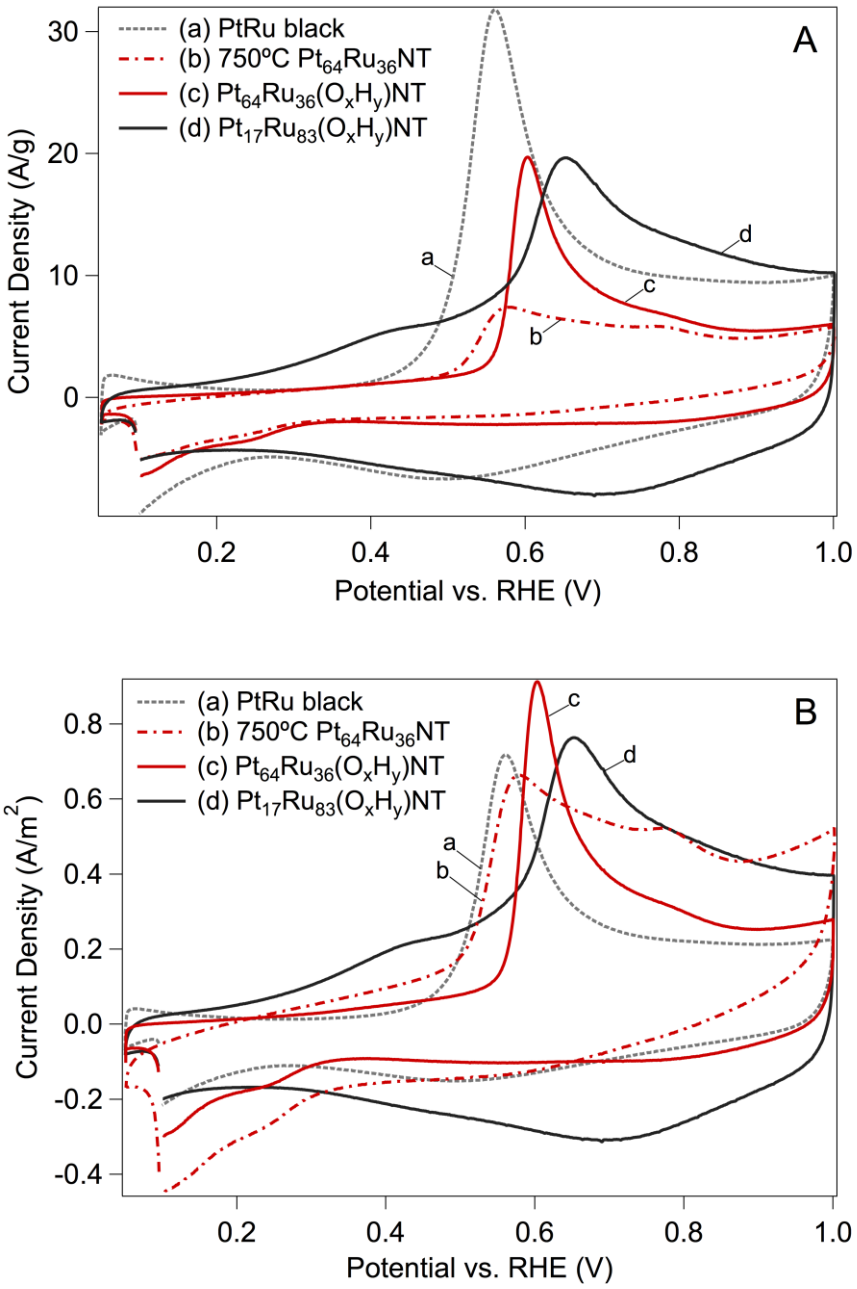

Figure 3.10. CO stripping voltammograms recorded in 0.5 M H_2SO_4 at 20 mV s^{-1} normalized to (A) total electrode mass and (B) ECSA. CO was adsorbed at 0.1 V vs. RHE.

Though the phase of Ru varies between the as-synthesized and annealed Pt-Ru nanotube samples, the change in CO stripping kinetics is more likely dependent on the proximity of Pt to Ru in the catalyst.[134] The bifunctional mechanism that is used to explain methanol oxidation on a Pt-Ru catalyst maintains that adsorbed CO is produced at the Pt sites while Ru provides oxygenated species to assist in oxidizing the adsorbed intermediate. The putative Pt and Ru(O_xH_y) layers in the as-synthesized PtRu(O_xH_y)NTs lack the proximity between Pt and Ru necessary for improved CO stripping kinetics.[135] In this case of distinct material layers with less uniform dispersion of Pt and Ru than in an alloy, there is a greater diffusional distance required of Pt-adsorbed CO to migrate along the catalyst surface to the Ru, the source of oxygen-containing species, for CO oxidation and desorption from the catalyst surface.[81,95,124] The ECSAs recorded by CO stripping for each catalyst tested are reported in Table 3.1.

Despite an observed decline in CO stripping kinetics, the as-synthesized PtRu(O_xH_y)NT samples are surprisingly active for methanol oxidation. This is an interesting, although not unique, result considering that CO-like intermediates are formed during the methanol oxidation reaction and a sample that oxidizes CO effectively is expected to be more active for methanol oxidation. However, CO oxidation does not necessarily correlate to methanol oxidation activity[134] and the

Table 3.1. Location of Pt(111) peak, crystallite size (L) measured by Scherrer analysis of the Pt(111) peak, electrode loading, electrochemical surface area (ECSA), MOR Mass and Specific Activities and MOR Pt mass and Pt specific activities at 0.65 V vs. RHE.

Sample	Pt(111) 2θ [deg]	L [nm]	Loading [μg/cm^2]	ECSA [m^2/g]	i_m [A/g]	i_s [mA/cm^2]	Pt i_m [A/g$_{Pt}$]	Pt i_s [mA/cm^2$_{Pt}$]
PtRu black	40.342	2.8	55.78	44.3	96	0.217	146.3	0.330
$Pt_7Ru_{93}O_xH_yNT$	-	-	68.33	14.4	9	0.063	70.9	0.497
$Pt_{17}Ru_{83}O_xH_yNT$	39.717	3.9	36.42	25.8	36	0.141	127.1	0.498
$Pt_{30}Ru_{70}O_xH_yNT$	-	-	26.13	20.7	38	0.183	83.9	0.404
$Pt_{38}Ru_{62}O_xH_yNT$	-	-	28.25	24.8	87	0.351	160.5	0.648
$Pt_{58}Ru_{42}O_xH_yNT$	39.763	3.8	29.36	33.6	107	0.318	147.1	0.437
$Pt_{64}Ru_{36}O_xH_yNT$	39.813	4.1	31.33	21.6	84	0.389	108.5	0.502
$Pt_7Ru_{93}NT$	-	33.8	36.88	9.9	3	0.030	23.6	0.236
$Pt_{21}Ru_{79}NT$	-	27.6	43.20	6.9	4	0.061	11.8	0.180
$Pt_{39}Ru_{61}NT$	40.568	12.0	40.75	-	13	-	23.5	-
$Pt_{42}Ru_{58}NT$	40.503	9.2	53.34	6.8	11	0.154	18.9	0.279
$Pt_{47}Ru_{53}NT$	40.437	13.7	42.03	6.1	10	0.161	15.8	0.276
$Pt_{51}Ru_{49}NT$	40.421	11.9	39.07	-	18	-	27.0	-
$Pt_{57}Ru_{43}NT$	40.326	9.7	42.79	7.8	14	0.179	19.3	0.268
$Pt_{59}Ru_{41}NT$	40.301	9.7	48.24	8.7	22	0.244	30.3	0.336
$Pt_{64}Ru_{36}NT$	40.238	11.8	38.21	9.0	30	0.333	38.7	0.430
$Pt_{69}Ru_{31}NT$	40.142	9.1	40.75	9.4	29	0.309	35.8	0.381
$Pt_{88}Ru_{12}NT$	39.937	16.3	45.85	9.3	11	0.118	11.8	0.126

$Pt_{64}Ru_{36}(O_xH_y)$NTs have a comparable mass activity to PtRu black at 0.7 V vs. RHE despite half the ECSA. Figure 3.11 shows linear sweep voltammograms for methanol oxidation with currents normalized to total catalyst mass (Figure 3.11A) and ECSA (Figure 3.11B). The high activity of the $Pt_{64}Ru_{36}(O_xH_y)$NTs can be ascribed to its high Pt utilization and the presence of hydrous Ru oxides in similarity with PtRu black.[131] This can be seen in the XPS scans of the Ru $3p_{3/2}$ peak (Figure 3.6) and also in X-ray absorption near-edge spectra (XANES) data in Figure 3.7. The annealed $Pt_{64}Ru_{36}$NTs demonstrate metallic Ru character similar to the Ru standard, which is in agreement with the X-ray diffraction data presented in Figure 3.4. There is a slight edge shift in the annealed sample compared to the Ru metal standard, likely from the formation of surface oxides. This is confirmed by the observation of oxides on the surfaces of the interior walls of the $Pt_{58}Ru_{42}$NTs in the HRTEM image in Figure 3.3(f) and such oxides are expected to be reduced to some degree during the methanol oxidation experiments.[132]

The substantial reduction in mass activity of the alloyed PtRuNTs is strongly influenced by changes in the catalyst structure that occur during the heat treatment at 750°C, namely, reductions in ECSA and Pt utilization. Prior to heat treatment, the as-synthesized $PtRu(O_xH_y)$NTs have finely-textured surfaces with considerably higher ECSAs than alloyed $Pt_{64}Ru_{36}$NTs due to a surface roughness not observed in the alloyed $Pt_{64}Ru_{36}$NTs. The SEM and TEM images

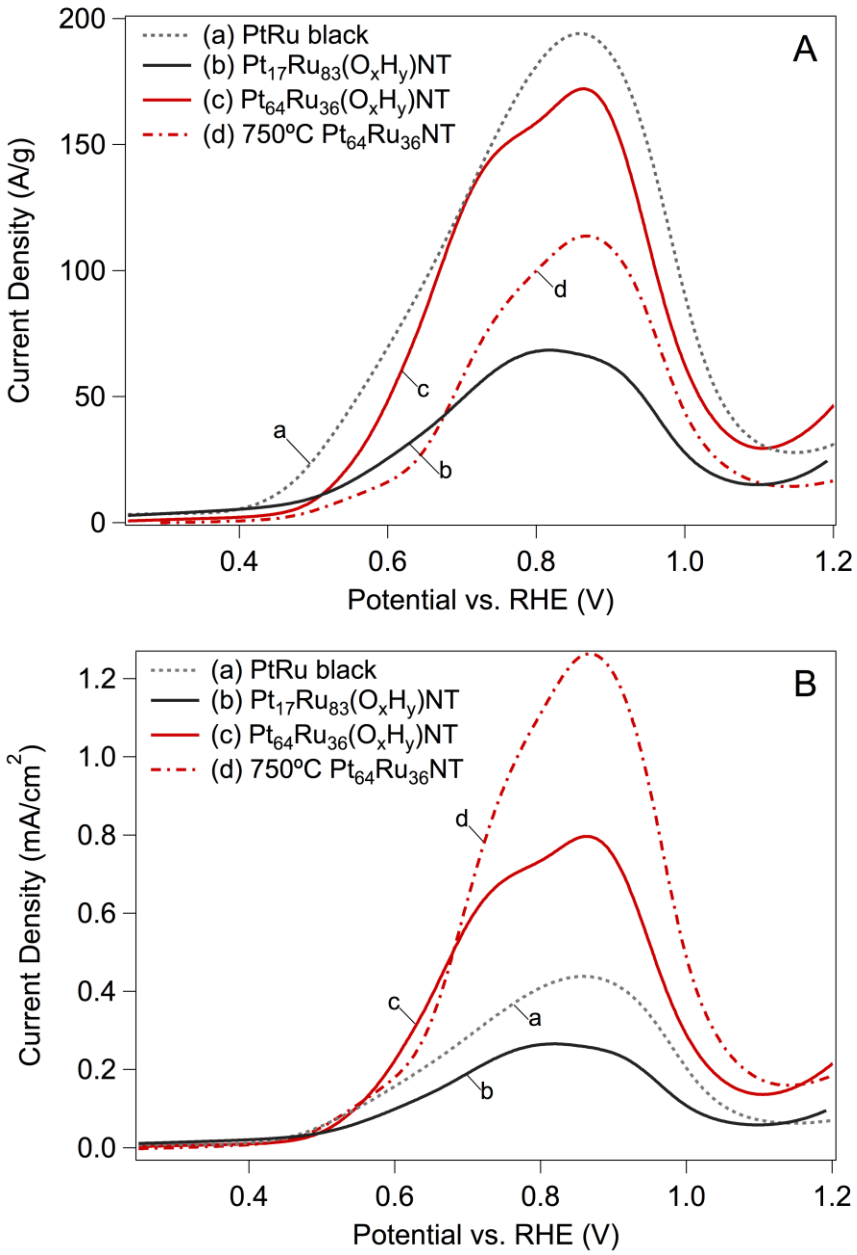

Figure 3.11. Linear sweep voltammograms recorded in 0.5 M CH_3OH and 0.1 M H_2SO_4 at 20 mV s^{-1}. Voltammograms are normalized to (A) total electrode mass and (B) ECSA.

in Figure 3.1(a-d) and Figure 3.3(a-d), respectively, reveal the fine nanoparticulate nature of the $PtRu(O_xH_y)$NT surfaces while the annealed PtRuNT surfaces [Figure 3.1 (e-h)] are smoother from the grain coarsening and surface relaxation induced by the high temperature treatment. In the alloyed $Pt_{64}Ru_{36}$NTs [Figure 3.11(d)], Pt has diffused within the 15-25 nm thick walls of the nanotubes during the heat treatment where it would not be accessible for methanol adsorption and dehydrogenation. However, in the as-synthesized, Pt-decorated nanotubes, catalytically active Pt would only be inaccessible when thick Pt layers or clusters formed during the synthesis of more Pt-rich samples. The methanol oxidation currents were normalized by the ECSAs measured during CO stripping voltammetry in Figure 3.10B and specific activities at 0.65 V are reported in Table 3.1. At 0.65 V vs. RHE, the alloyed $Pt_{64}Ru_{36}$NTs with considerably lower surface area demonstrated comparable specific activity (0.33 mA/cm^2) to the as-synthesized nanotube sample with similar composition (0.39 mA/cm^2) and 1.5 times the specific activity of the commercial PtRu black (0.22 mA/cm^2). Of the highlighted nanotube catalysts in Figure 3.11, only the as-synthesized $Pt_{17}Ru_{83}(O_xH_y)$NT sample with significantly less Pt had a lower intrinsic activity than the commercial PtRu black (50% Pt). With a considerable reduction in Pt content from 64% Pt to 17% Pt in these $Pt_{17}Ru_{83}(O_xH_y)$NTs in Figure 3.11, the promotional effect of the underlying $Ru(O_xH_y)$ on Pt is more distinct, as the

sample reaches a peak current for methanol oxidation at a potential 52 mV lower than the more Pt-rich $Pt_{64}Ru_{36}(O_xH_y)$NTs.

The experimental nanotube catalysts discussed here represent a broad range of Pt composition; therefore, we also consider the catalysts' Pt content in the context of activity. Sample activity per unit of Pt mass, and also sample activity normalized to Pt mass and sample ECSA, here referred to as Pt specific activity, are recorded at 0.65 V vs. RHE and reported in Table 3.1. Considering the high activities of the as-synthesized nanotubes, it may be interesting to consider the potential for these dual-layer nanotubes following a third consecutive vapor deposition of a final interior layer of Pt. This resulting nanotube would be composed of three distinct layers, Pt-Ru(O_xH_y)-Pt, with active surfaces at both the exterior and the interior of the hollow nanotube and promises further improvements in mass activity.

Conclusion

We have detailed the synthesis of monometallic, layered bimetallic, and alloyed bimetallic nanotubes by a novel method based on templated vapor deposition from metal acetylacetonate precursors. Prior to recovery from sacrificial anodic alumina templates, the nanotubes may be thermally annealed to induce a host of chemical and structural evolutions with significant implications on catalytic activity. Hydrous Ru oxide was reduced to metal during heat treatment in a forming gas, yielding Pt-Ru alloys with composition-dependent

crystal structures. Annealed PtRuNTs demonstrated non-uniform, nanoscale porosity as a result of observed grain size increases of approximately 3 times after 1 hour at 750°C.

Alloyed PtRuNTs demonstrated improved CO stripping kinetics compared to the as-synthesized PtRu(O_xH_y)NTs, suggested to be the result of the increased dispersion of Pt and Ru following thermal treatment. However, PtRu(O_xH_y)NTs had a higher Pt utilization and higher electrochemically active surface areas than alloyed PtRuNTs. Despite relatively poor CO stripping kinetics, the as-synthesized, Pt-decorated, hydrous ruthenium oxide nanotubes demonstrated higher mass activities than alloyed platinum-ruthenium nanotubes at 0.65 V vs. RHE. With performance normalized to ECSA, PtRu(O_xH_y)NTs and alloyed $Pt_{64}Ru_{36}$NTs demonstrated 1.5 times the activity for methanol oxidation than PtRu black at 0.65 V vs. RHE.

The methods we demonstrate here are broadly applicable to the synthesis of high surface area, extended metal and oxide surfaces with tunable composition and microstructure. Though we demonstrate applications for electrooxidation of simple alcohols here, the materials palette made available via this approach is appropriate for a host of catalysis applications.

CHAPTER 4

SUPPORTLESS, BISMUTH-MODIFIED PALLADIUM NANOTUBES WITH IMPROVED ACTIVITY AND STABILITY FOR FORMIC ACID OXIDATION

Abstract

Palladium nanotubes (PdNTs) were synthesized by templated vapor deposition and investigated for formic acid electrooxidation. Annealed PdNTs are 2.4 times more active (2.19 mA/cm^2) than commercial carbon-supported palladium (0.91 mA/cm^2) at 0.3 V vs. RHE. Bismuth modification improved nanotube performance over 4 times (3.75 mA/cm^2) vs. Pd/C and nearly 2 times vs. unmodified PdNTs. A surface Bi coverage of 80% results in optimal site-specific activity by drastically reducing surface-poisoning CO generation during formic acid electrooxidation. The Bi-modified PdNTs are exceptionally stable, maintaining 2 times the area-normalized current density as Pd/C after 24 hours at 0.2 V vs. RHE. We attribute the enhanced activity and stability of the nanotube catalysts to the presence of highly coordinated surfaces, mimicking a flat polycrystal while retaining high surface area geometry.

Introduction

The growing market for portable and mobile devices has driven the demand for small, light, long-lasting power sources. Direct liquid fuel cells (DLFCs) have the potential to compete with current battery technology in these arenas because of the high volumetric energy density of liquid fuels. Formic acid is an attractive fuel option that is non-toxic, non-flammable, and can be used in

highly concentrated fuel feed streams without the crossover observed in direct methanol fuel cells (DMFCs).[9,136]

A common shortcoming of DLFCs is low efficiency due to the high overpotential typically required for fuel oxidation. Here we use overpotential to refer to the additional applied voltage beyond the thermodynamic requirement needed for an electrochemical reaction to proceed, that is, for current to flow. In many cases, an applied overpotential affects the removal of adsorbed species from the catalyst surface. This is the case in both DMFCs and direct formic acid fuel cells (DFAFCs), for which anode catalyst poisoning by CO is a deactivation channel (Eq. 4.1).[137] However, a direct reaction pathway (Eq. 4.2)[137] is accessible depending on the adsorption orientation of formic acid.[138] Designing catalysts selective for this path is thus the key to enabling efficient DFAFCs.

Indirect pathway (overpotential > 0.6V)[138]

$$HCOOH \rightarrow CO_{ads} + H_2O \rightarrow CO_2 + 2H^+ + 2e^- \quad (4.1)$$

Direct pathway (overpotential > 0.18V)[139]

$$HCOOH \rightarrow CO_2 + 2H^+ + 2e^- \quad (4.2)$$

Palladium has been shown to be highly active for formic acid electro-oxidation at low potentials because it favors the direct pathway.[89] However, Pd lacks sustained performance from the accumulation of CO_{ads} that can form from competition by the indirect pathway.[28,140–143] Modifying Pd to promote its activity at low overpotentials and to improve its stability by limiting CO_{ads} formation is

essential. Strategies centered on alloying to remove CO_{ads} generated by the indirect pathway have been described previously.[89,144–150]

The addition of adatoms to the catalyst surface, like Bi or Sb, has been shown to improve formic acid electro-oxidation activity at low overpotentials by so-called ensemble or third-body effects.[138,139,151–157] Coupled in situ surface-enhanced infrared spectroscopy and first-principles density functional theory (DFT) calculations indicate that the addition of adatoms can influence the configuration of the formic acid molecule at the catalyst surface.[138] High adatom coverage can promote the adsorption of formic acid in the CH-down configuration[138] that is considered the precursor for the direct formic acid oxidation (FAO) pathway and high activity at low overpotentials.[158–162]

The less desirable indirect pathway for formic acid oxidation requires a larger ensemble of metal atoms than the direct pathway,[157,158] therefore, a high adatom coverage that effectively reduces the Pd ensemble size can improve formic acid electrooxidation activity at low overpotentials. Because active catalyst surface area is lost to the adsorbed adatom, having a high proportion of adjacent low index sites is paramount when pursuing strategies that use adsorbed promoter atoms. High surface area catalysts do not provide sufficient surface area for Bi adsorption adjacent to active sites for formic acid adsorption because they have small terraces. Additionally, these catalysts lose half of their surface to low coordination edge and vertex sites.[32]

An alternative to supported nanoparticle catalysts are unsupported extended-surface catalysts, such as metallic nanowires or nanotubes. Metallic nanotubes have many similarities to bulk polycrystalline materials while maintaining nanoscale dimensionality, allowing very high activities while limiting sacrifices in active surface area. Extended surface catalysts have highly coordinated surfaces that are more resistive to corrosion and ripening,[31,32,35,36,40,163] reduced oxophilicity and binding of oxygenated intermediates,[21,25,30] and significant flexibility to achieve optimal porous structure via heat treatment.[85,117,164] In this contribution, we describe palladium nanotubes (PdNTs) designed to mimic highly coordinated polycrystalline surfaces but with nanoscale dimensions and mesoporosity. As a result, the nanotubes maintain high surface area without the formation of an under-coordinated surface associated with reductions in nanoparticle size.[70] This was achieved via the use of a modified chemical vapor deposition technique to synthesize the PdNTs within sacrificial, porous alumina templates. The morphology and grain size of the nanotubes were adjusted by thermal treatments of the Pd-lined templates using post-deposition heat treatment. The sacrificial templates were dissolved to release unsupported nanotubes. Electrochemical bismuth adsorption was subsequently used to systematically probe the coverage-dependent steric effects for the promotion of the direct electrooxidation of formic acid.

Experimental

Nanotube Synthesis. Palladium nanotubes (PdNTs) were synthesized by a chemical vapor deposition within the pores of an anodic alumina membrane (Whatman Anodisc, 13 mm diameter, 200 nm pore size) by a technique reported previously.[117] A powder of palladium(II)(2,4)-pentanedionate (Alfa Aesar), so-called palladium acetylacetonate, was confined beneath the alumina template and placed in a vacuum oven with 2.3 mL of deionized water. Air was evacuated from the oven by a rotary vane vacuum pump and replaced with dry N_2 several times before the pressure was reduced to 0.3 bar and the oven sealed. The thermostat was set to a calibrated value of 170°C and this final temperature was maintained for 15 hours before the oven was flushed with dry N_2 and cooled to room temperature to recover the Pd-filled template.

The Pd-bearing templates were either immediately dissolved to recover as-synthesized PdNTs or thermally annealed to induce morphological evolution. After purging a quartz furnace tube for 30 minutes, the sample templates were heated at one of a range of temperatures for 1 hour with flowing 4% H_2 (balance Ar) before they were allowed to cool passively to room temperature. The temperatures selected for the heat treatments were 300°C, 400°C, and 500°C.
The sample templates were stirred in a 30% KOH solution at room temperature for 90 hours to completely dissolve the templates. Afterwards, the supernatant

solution was decanted and replaced with de-ionized water until the nanotubes were suspended in a solution with neutral pH.

Scanning Electron Microscopy. SEM micrographs were collected using a ZEISS 1525 Field Emission Scanning Electron Microscope with an accelerating voltage of 3 kV using the in-lens electron detector.

Transmission Electron Microscopy. Thin cross-sections of the nanotubes within the alumina template were prepared using a Hitachi NB-5000 focused ion beam (FIB). High-angle annular dark-field (HAADF) scanning transmission electron microscopy (STEM) imaging and EDS mapping were conducted using a JEOL 2200FS operating at 200 kV. Nanotubes liberated from the sacrificial template and suspended in water were drop cast onto lacy carbon and dried under vacuum to collect high-resolution transmission electron microscopy (HRTEM) images with a ZEISS Libra 200MC at an accelerating voltage of 200 kV.

X-ray Diffraction. X-ray diffraction (XRD) patterns were recorded with a Bruker D2 Phaser diffractometer with Cu Kα radiation (λ = 0.1541874 nm, 30 kV, 10 mA, 0.014° step, 0.5 s/step). Small aliquots of the nanotubes suspended in water were cast onto a zero-background Silicon wafer for data collection. The diffraction peaks were fit using a Voigt function with IGOR Pro (Wavemetrics, Inc.) allowing for determination of their positions and widths.

X-ray Absorption Spectroscopy. X-ray absorption spectroscopy (XAS) was conducted at beamline 20-BM at the Advanced Photon Source at Argonne National Laboratory (Argonne, IL, USA). Pre-edge correction, normalization, and post-edge subtraction via spline fitting were done in Athena.[165] The k^2-weighted $\chi(R)$ forward Fourier Transform (FT) parameters were: R-range, 1 – 3 Å; window, Hanning.

Electrochemical Measurements. Electrode inks were prepared by diluting the water-suspended nanotubes to 0.65 – 0.80 mg_{Pd} mL^{-1} without the addition of alcohol or ionomer, as is common for carbon-supported, high-surface-area catalysts.[104] Measurements were conducted with a glassy carbon working electrode, platinum wire counter electrode and a reversible hydrogen reference electrode (RHE) using a Bio-Logic VMP3 potentiostat. All electrolytes were purged with ultrahigh purity N_2 for 30 minutes prior to experiments.

Carbon monoxide (CO) stripping voltammograms were recorded in 0.5 M H_2SO_4 via a technique described elsewhere[46,139] to calculate electrochemically active surface areas (ECSAs). The ECSAs were calculated using the charge for removing a monolayer of CO from a Pt surface (420 μC cm^{-2}).[166] FAO activity was measured by cycling the electrode once in fresh 0.5 M formic acid (HCOOH, Fluka Analytical, for HPLC) and 0.5 M H_2SO_4 at 20 mV s^{-1}. Chronoamperometry experiments were performed in 1.0 M formic acid and 0.1 M $HClO_4$ (GFS Chemicals, Veritas) with potential held at 0.2 V vs. RHE for 24 hours without

rotation. Cyclic voltammograms were recorded before and after chronoamperometry experiments to study changes in the catalysts after long-term stability experiments. Though such experiments were not conducted in this work, the analysis of the electrolytes used in the chronoamperometry experiments via inductively coupled plasma mass spectrometry (ICP-MS) would allow for accurately quantifying the amounts of Pd and Bi that dissolve from the electrode. This will be considered as a subject of future study.

Carbon-supported Pd (Pd/C, Alfa Aesar, 20 wt% Pd) was used as a standard for comparison of the performance of the experimental catalysts. The commercial catalyst (5 mg) was dispersed in 3:1 water to isopropanol solvent mixture (4 mL) containing 5 mg of Nafion from a 5% solution (Ion Power, Inc.). Bismuth (Bi) adatoms were underpotentially deposited on PdNTs annealed at 500°C. An electrode with PdNTs was immersed in a 0.5 mM $Bi_2(SO_4)_3$ (Alfa Aesar, 99%) and 0.5 M H_2SO_4 electrolyte with a constant potential (0.485-0.735 V vs. RHE) held for 2 minutes, depending on the desired adatom coverage. This method is notable for its difference in comparison to spontaneous deposition of Bi onto Pt surfaces without the need for applying a potential. Such spontaneous deposition onto Pt is well-known and has been used to quantify Pt(111) contributions to surface area on polycrystalline surfaces.[167–170] The Bi surface coverage was determined using CO stripping voltammetry with a method reported previously.[152] The ECSA used to normalize currents for the Bi-modified

PdNTs refers to the Pd without adsorbed Bi available for carbon monoxide adsorption.

Results and Discussion

Conformal coatings of Pd are vapor-grown within the channels of a porous anodic alumina template in order to form the high aspect ratio, metallic Pd nanotubes. HAADF STEM and EDS map images for cross-sections of the Pd nanotubes still embedded within the alumina template are shown in Figure 4.1. The aluminum (b, f) and oxygen (c, g) maps in Figure 4.1 identify the porous alumina template, which supports a thin layer of vapor-deposited Pd (d, h). In the as-synthesized sample template in Figure 1(a-d), the fine Pd nanoparticles form

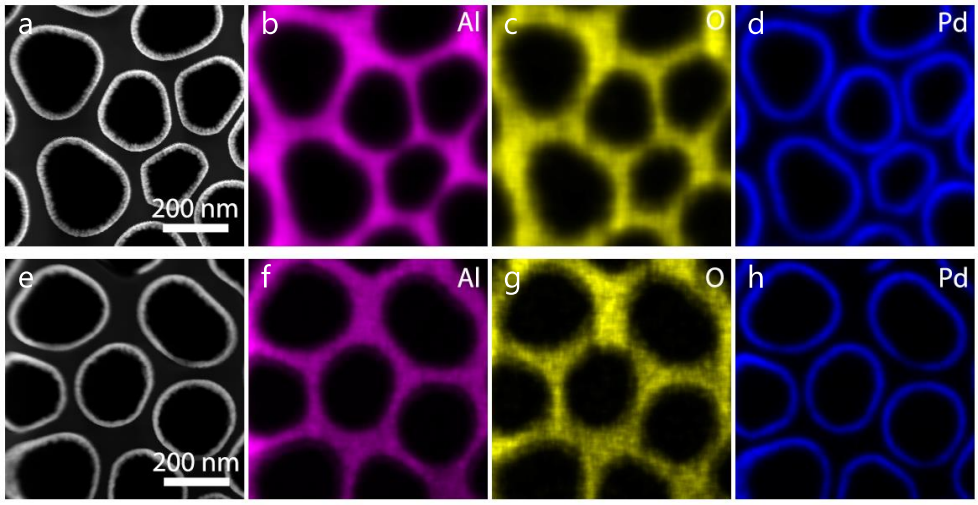

Figure 4.1**.** HAADF STEM and EDS elemental mapping of the templated (a-d) as-synthesized PdNTs and (e-h) PdNTs annealed at 500°C.

a conformal layer along the interior pores of the anodic alumina template. After heat treatment at 500°C for 1 hour, the thickness of the Pd deposit decreases while still conforming to the template pore walls, reflecting reductions in nanotube wall thickness that accompany the transition from loosely associated nanoparticle aggregates towards Pd grain growth to form a polycrystal-like surface. The nanotube samples were harvested for further study of their microstructures and for electrochemical characterization by dissolving the sacrificial template in KOH. The HRTEM images in Figure 4.2 show subtle changes in the microstructures of the PdNTs that are a result of thermal annealing. The as-synthesized PdNTs [Figure 4.2(a,b)] are best described as loosely aggregated and fine Pd nanoparticles. As a result, these nanotubes were less robust than the annealed PdNTs, manifested by a greater frequency of shortened and broken nanotubes. The morphologies of the PdNTs annealed at 300°C [Figure 4.2(c,d)] and 400°C [Figure 4.2(e,f)] are nearly indistinguishable aside from a marginal increase in Pd grain size. These annealed nanotubes more consistently maintain high-aspect ratio, tubular microstructures compared to the as-synthesized nanotubes, which may be the result of incremental Pd particle growth that occurred during heat treatment. The changes between the PdNTs annealed at 400°C and 500°C are more distinct, however. The PdNTs annealed at 500°C [Figure 4.2(g,h)] are the most coarse-grained and have the highest degree of nano-porosity. The fast Fourier transform (FFT) of the boxed region in Figure

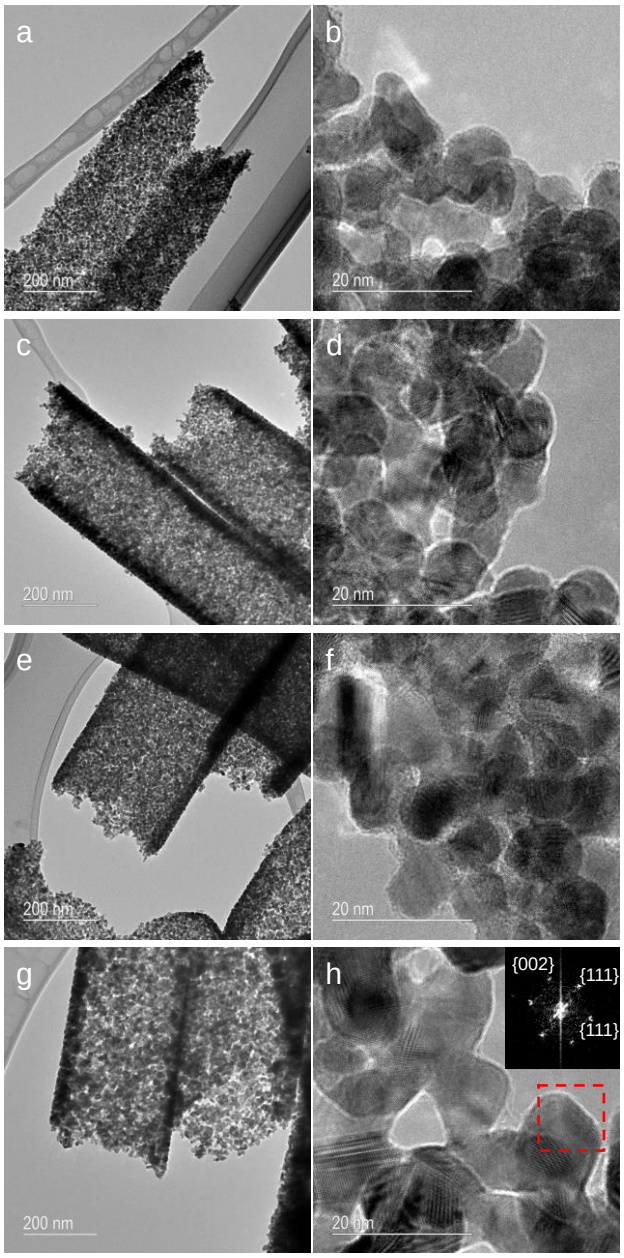

Figure 4.2**.** High-resolution transmission electron microscopy (HRTEM) images of PdNTs (a,b) as-synthesized and after heat treatments in 4% H_2 for 1 hr at (c,d) 300°C, (e,f) 400°C, and (g,h) 500°C. FFT analysis from the boxed region in (h) corresponds to crystalline, FCC Pd oriented along the [110] zone axis.

Figure 4.2(h) is represented in the image inset and is consistent with face-centered cubic (FCC) palladium.

The nanotube morphology is consistent with the shapes of the pore interiors of the AAO templates in which they were grown, as illustrated using the scanning electron microscopy (SEM) images in Figure 4.3. The nanotubes reported here, although having a different composition, have a remarkably similar nanoscale structure to previously investigated samples.[117,164] The PdNTs are roughly 250 nm in diameter with variable lengths ranging from 1 to 10 μm. There is a growth in grain size, observable upon careful inspection here and more clearly in the HRTEM images in Figure 4.2, from the as-synthesized PdNT (Figure 3a) to the annealed PdNTs. In the SEM images in Figure 4.3, this grain growth is manifested by changes in texture of the nanotube surfaces. At these magnifications, the nanoparticles are unresolvable in the as-synthesized PdNTs and give the surfaces of these relatively thick-walled nanotubes a fine, nanoparticulate texture. After heat treatments at 300°C (Figure 3b) and 400°C (Figure 4.3c) individual grains may be resolved, fine nanoscale porosity is initiated, and the exterior surfaces become smoother. After annealing at 500°C (Figure 4.3d), we observe a maximum in porosity, a reduction in nanotube wall thickness from 30 nm to roughly 20 nm, and a maximum in grain size for the nanotube samples.

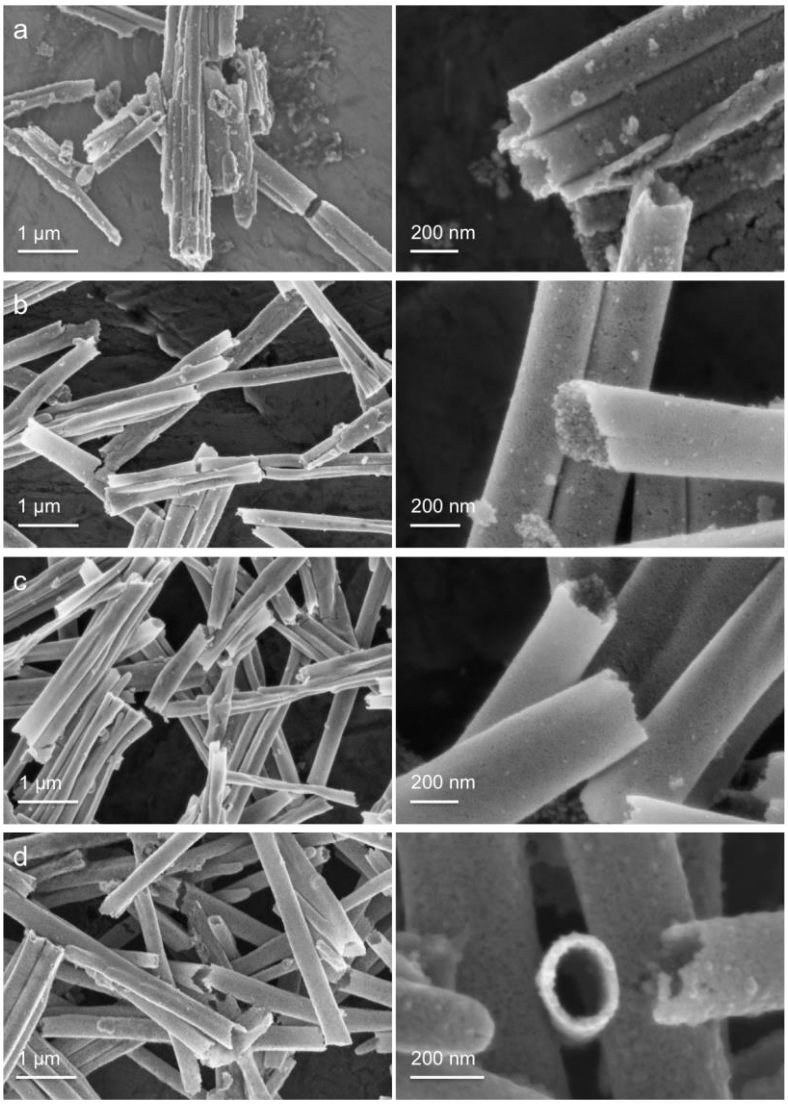

Figure 4.3**.** Scanning electron microscopy (SEM) images of PdNTs (a) as-synthesized and after heat treatments in 4% H_2 for 1 hr at (b) 300°C, (c) 400°C, and (d) 500°C. Increases in grain size are observed with increasing heat treatment temperature. Grain size estimates are provided in the text using XRD data.

The PdNT X-ray diffraction patterns were studied to measure the initial Pd grain sizes formed during synthesis, as well as study the influence of temperature on grain growth during the heat treatment. Cu Kα X-ray diffraction patterns are given in Figure 4.4. The as-synthesized PdNTs are characterized by broad FCC peaks indicating that the nanotubes are aggregates of finely packed, nanoparticulate Pd, with an average grain size of 3.7 nm in diameter. The diffraction patterns of the annealed samples increase in sharpness (i.e., reduction of the peak's full-width at half its maximum, FWHM) with increasing heat treatment temperature reflecting increases in grain size that are observable in the HRTEM and SEM images in Figure 4.2 and Figure 4.3, respectively. We calculate a maximum Pd grain size of 11.6 nm after annealing at 500°C. The average grain sizes for each sample are calculated using a Scherrer analysis of the Pd(111) peak and are reported in Table 4.1.

The primary diffraction peak of the as-synthesized PdNT is shifted relative to the reference Pd(111) peak because of absorption of interstitial carbon from the decomposition of the organic ligand during vapor deposition.[171–173] Carbon increases the size of the Pd lattice by inserting into interstitial sites, observed here as a decrease in the inversely related diffraction angle. The lattice expansion from interstitial carbon has been observed previously in other Pd catalysts that were synthesized by our group using this technique.[50,174] The return

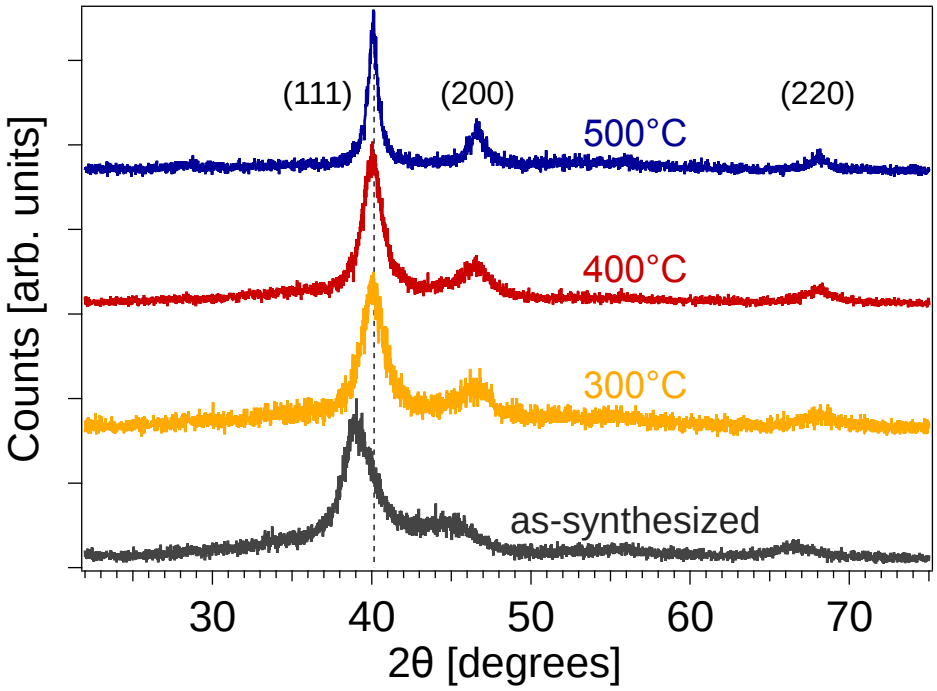

Figure 4.4**.** Cu Kα X-ray diffraction patterns for as-synthesized PdNTs and after annealing in 4% H_2 at 300°C, 400°C and 500°C for 1 hour. Dashed line corresponds to Pd(111) peak (PDF: 00-005-0681).

of the primary peak to the location of the Pd(111) peak in the reference reflects the removal of interstitial carbon during heat treatment.

Results from X-ray absorption spectroscopy are used to reveal the changes in atomic-scale structure and evolution during heat treatment and to compare with the commercial Pd/C catalyst. The X-ray absorption near edge structure (XANES) patterns in Figure 4.5(A) illustrate that both nanotube samples have similar electronic character to the zero-valent Pd foil, while the increased white-line intensity of Pd/C and shift to higher energy suggests that it is highly oxidized. The forward Fourier transforms of the extended X-ray absorption fine structure (EXAFS) oscillations in Figure 4.5(B) yield the radial positions of the nearest neighbors to the Pd absorber. The Pd-Pd radial position in the as-synthesized nanotubes show increased atomic spacing consistent with interstitially absorbed carbon.[172] Following heat treatment, the Pd-Pd radial position shifts back to match that of the Pd reference foil [gray line, Figure 4.5(B)]. As the Pd grain size/atomic coordination increases, the magnitude of the Pd-O interaction decreases. This is indicated in Figure 4.5(B) by a reduction in peak intensity at a radial position of ~1.5 Å. This reproduces the well-known effect that more highly coordinated surfaces are less oxophilic that is also observed in cyclic voltammograms in sulfuric acid.

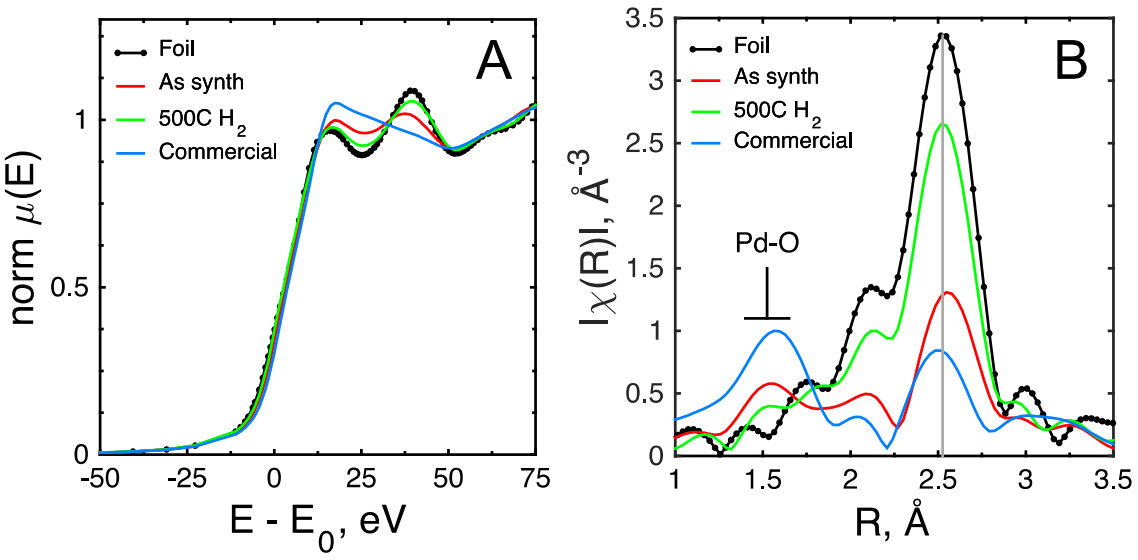

Figure 4.5**.** (A) Normalized XANES patterns for the as-synthesized and heat-treated PdNT samples, as well as commercial Pd/C compared to foil at the Pd K edge. (B) Forward Fourier transforms of the EXAFS at the Pd K edge. Gray line indicates Pd-Pd radial position. The lattice expansion due to carbon absorption in the as-synthesized sample is reflected in EXAFS as a shift to larger Pd-Pd radial position. The shift in the Pd peak of the commercial Pd/C to lower radial position reflects its high degree of oxidation and the smaller atomic size of Pd^{2+} (here observed as PdO).[175]

Because of reductions in nanotube oxophilicity, we expect that electrochemical surface oxides and poisons (e.g., CO) would be more easily removed from the PdNTs when compared to commercial Pd/C catalysts. Evidence of this weaker adsorption of oxygen-containing species by the catalyst surface can be observed in the positive shift of the palladium oxide reduction peak (Figure 4.6A inset) in the reverse scan.[64] The 500°C annealed PdNTs feature a more positively shifted palladium oxide reduction feature than the nanotubes annealed at 300°C and 400°C from a grain size increase at elevated temperatures; this behavior is also observed in platinum catalysts with increasing Pt crystallite size.[63,64,66]

The reduced oxophilicity of the nanotube catalysts also affects CO removal. There is a significant decrease in the potentials of the CO stripping peaks for the palladium nanotube samples in comparison to the Pd/C [Figure 4.6(B)]. This has been attributed to greater surface mobility of oxygen-containing species that are less strongly bound to extended surface catalysts in comparison to small, supported nanoparticles.[25,30,46]

The 500°C PdNT sample features a small CO oxidation feature at lower potential than the main CO stripping peak. This pre-ignition feature has been observed in extended Pt catalysts[25,30] and is reported to result from defect sites located at grain boundaries.[176] The presence of a grain-boundary-like component emphasizes that the annealed nanotube catalysts are close analogs to

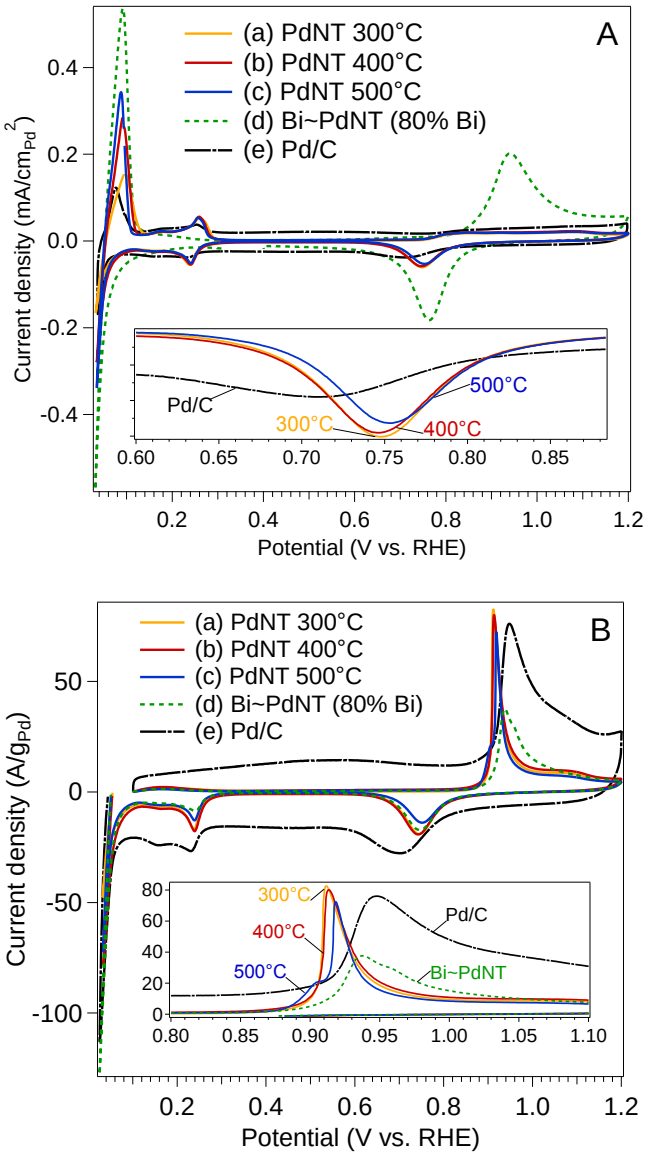

Figure 4.6**.** (A) Baseline cyclic voltammograms and (B) CO stripping voltammograms recorded in 0.5 M H_2SO_4 for the PdNTs annealed at (a) 300°C, (b) 400°C, (c) 500°C, (d) 500°C with 80% Bi surface coverage (Bi~PdNT), and (e) carbon-supported Pd. The inset in (A) highlights the Pd oxide reduction region. The inset in (B) magnifies the CO stripping peaks.

polycrystalline surfaces. This highlights a considerable advantage to the application of these metallic nanotubes, as highly active surfaces may be synthesized with nanoscopic dimensions that limit sacrifices in surface area.

Though hydrogen absorption and adsorption processes occur in the same potential region, the anodic peak at 0.1 V is reported to be dominated by the desorption of absorbed hydrogen.[177] The increase in current density of the anodic peak at 0.1 V with heat treatment temperature in the PdNT samples may correspond to an increase in hydrogen absorption by the nanotubes with coarsened Pd grains, as hydrogen absorption is more stable and abundant in larger Pd grains.[177,178] Palladium electrodes report inaccurate hydrogen underpotential deposition (H_{UPD}) charges because of this subsurface hydride formation, which produces current additional to H_{UPD} surface charging currents in the same potential region.[179,180] Therefore, the ECSA was determined by normalizing the charge of the CO stripping peak by the charge corresponding to the removal of a monolayer of pre-adsorbed CO from the catalyst surface, 420 $\mu C\ cm^{-2}$; these ECSAs are reported in Table 4.1.

Compared to the Bi-free PdNTs, the Bi-modified PdNTs (Bi~PdNT) with 80% Bi coverage [Figure 4.6(d)] have nearly eliminated charging from H_{UPD} because of interference from adsorbed Bi adatoms. Additionally, there is a reversible Bi oxidation/reduction feature at 0.94 – 0.77 V vs. RHE. The degree of Bi surface coverage of Pd is determined using the charges from the Bi oxidation

Table 4.1**.** Location of Pd(111) peak, grain size (L) measured by Scherrer analysis of the Pd(111) peak, electrode loading, electrochemical surface area (ECSA), and FAO Mass and Specific Activities at 0.3 V vs. RHE.

Sample	Heat Treatment	Pd[111] 2θ (deg)	L (nm)	Loading ($\mu g_{Pd}/cm^2$)	ECSA (m^2/g)	i_s (0.3 V) (mA/cm^2)	i_m (0.3 V) (A/g_{Pd})
300°C PdNT	300°C	40.060	4.9	38.63	29.6	1.56	461.8
400°C PdNT	400°C	40.042	5.8	36.91	30.7	1.83	561.8
500°C PdNT	500°C	40.084	11.6	38.21	24.7	2.19	540.9
Bi~PdNT (80%)	500°C	40.084	11.6	39.07	10.0	3.75	375.0
Pd/C	-	40.201	3.5	38.21	65.4	0.91	595.1

peak and the CO stripping peak with a method adapted by Bauskar and Rice[152] from techniques used for Bi-modified Pt electrodes.[181]

The PdNTs annealed at 500°C that have been modified with surface Bi adatoms [Figure 4.6(B,d)] have a unique CO stripping feature that demonstrates CO stripping from free Pd surface sites in addition to Bi oxidation, occurring in the same potential range. The CO stripping voltammogram for the Bi-modified sample peaks at 0.94 V with a broad shoulder at higher potentials (0.97 V) from the oxidation of Bi, which is also visible in the baseline voltammogram in Figure 4.6A(d).

The addition of Bi adatoms to the catalyst surface reduces the Pd ensemble size, which is considered to promote FAO activity at low potentials[157,158] compared to a surface free of adatoms. In Figure 4.7, the formic acid oxidation voltammogram of unmodified PdNTs [Figure 4.7(a)] is compared to voltammograms of PdNTs after the adsorption of Bi adatoms to 42% and 80% coverage. At an intermediate coverage of 42% Bi [Figure 4.7(b)], we observe a reduction in specific activity compared to the unmodified PdNTs at 0.3V despite a cathodic shift of the potential for their peak FAO current. Increasing the Bi coverage to 80% results in both increased specific activity at low potential as well as a more negative shift in peak current potential for FAO. Together, these observations suggest that at high Bi coverages a highly active ensemble of Pd active sites has formed on the catalyst surface that enhances FAO activity.

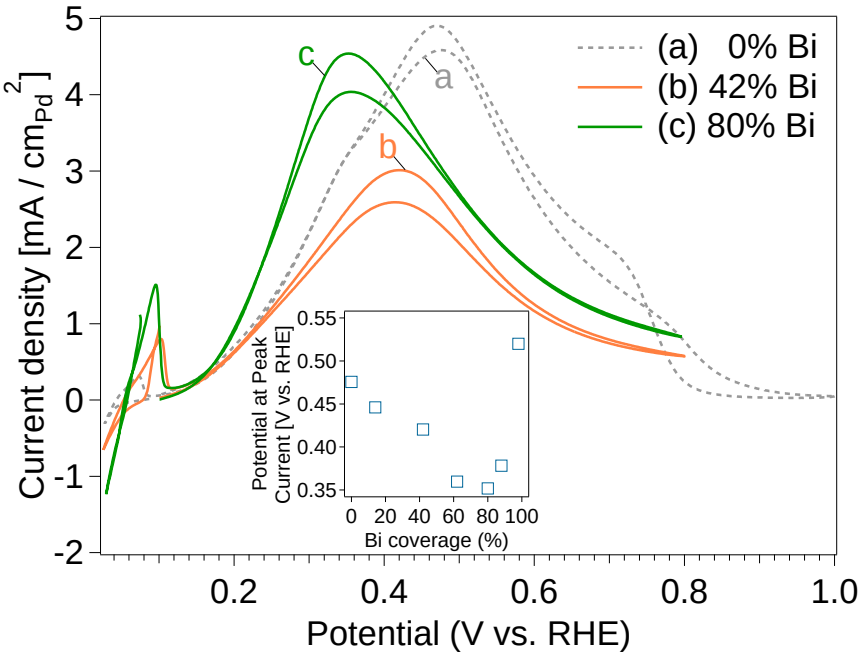

Figure 4.7**.** Area-normalized cyclic voltammograms recorded at 20 mV/s in 0.5 M H_2SO_4 and 0.5 M HCOOH for (a) PdNTs annealed at 500°C prior to Bi coverage, and with (b) 42% Bi and (c) 80% Bi coverage. Voltammograms are normalized to available Pd area. Labels point to forward scans of voltammograms. The inset plots the potential of the peak current in the anodic scan as a function of Bi coverage.

This activity improvement at high adatom coverages is consistent with computational and experimental data for an ensemble, or third-body effect.[151] The inset in Figure 4.7 reports the potential for the peak FAO current density in the anodic scan as a function of Bi coverage. As the Bi adatom coverage increases, the potential of the peak FAO current density decreases until optimal adatom coverage of 80% Bi is reached. At higher Bi coverages (>88% Bi), the FAO peak current shifts back to higher potentials. The addition of Bi adatoms to these PdNTs improves their FAO activity significantly at low overpotentials, which suggests their promise for improvements in long-term FAO stability.

We studied the effect of Bi adatom coverage of the PdNT surface on formic acid oxidation activity and found an optimum surface coverage of Bi at 80%. The scatter plot in Figure 4.8 reports the specific activity at 0.3 V vs. RHE as a function of Bi coverage on the PdNTs. There is an observed decrease in specific activity with a low Bi coverage (less than 40%), as the Bi adatoms cover and deactivate surface Pd sites. This reduction in activity suggests that there is not a significant electronic effect from the Bi on the PdNTs at this low surface coverage, otherwise a small amount of surface Bi coverage would still be expected to enhance the FAO activity.[151] At this low Bi coverage there may not be a sufficient amount of Bi on the surface to promote a considerable third-body effect.

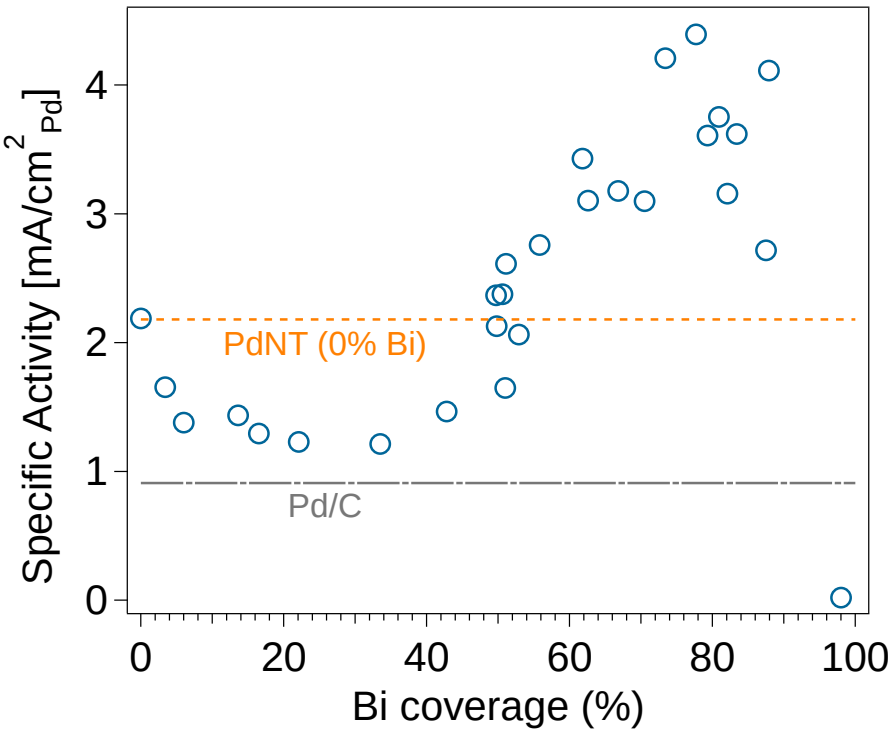

Figure 4.8**.** Scatter plot of specific activity of PdNTs as a function of their surface Bi coverage (in percent). The specific activity is reported at 0.3 V vs. RHE from voltammograms recorded in 0.5 M H_2SO_4 and 0.5 M HCOOH at 20 mV/s. The orange dashed line corresponds to the specific activity of unmodified, 500°C PdNTs and the gray dash-dot line represents the specific activity of Pd/C, both also reported at 0.3 V vs. RHE. Specific activity is normalized to available Pd area.

At high Bi coverage (50-87.5%) the specific activity is increased compared to the activity measured for the unmodified PdNTs (orange dashed line, 2.18 mA/cm^2), peaking in FAO activity at 80% Bi coverage (3.75 mA/cm^2). The specific activity improvement indicates that the intrinsic activity of the catalyst at low potential is only increased when a high Bi coverage is obtained, consistent with a third-body effect.[151] High Bi coverages here may restrict the Pd ensemble size to fewer atoms than is suggested to be required for the undesirable pathway of FAO that is not active at low overpotentials.[157,158,182] It is important to note that the specific activity reported here is calculated using an ECSA that is defined by the remaining exposed surface Pd sites, which are those not already covered by Bi. At very high Bi adatom coverages (>87%), remaining active sites are likely less accessible as the surface becomes more saturated with Bi,[139] interfering with formic acid adsorption and oxidation on these Pd surfaces.

We observe similar trends in the mass activity of PdNTs as a function of Bi coverage that are shown in Figure 4.9. Owing to the high activity of Pd for the oxidation of formic acid, any amount of Bi added to the surface of the PdNTs in an attempt to improve the stability and resistance to poison formation of the catalyst results in a sacrifice of Pd active sites and a reduction in mass activity. For the Bi-modified PdNTs with Bi coverage of 62-74%, we observe a maximum mass activity of 397 A/g_{Pd}. Though this is a significant decrease in the mass activity compared to the Bi-free PdNTs (541 A/g_{Pd}), the influence of a third body

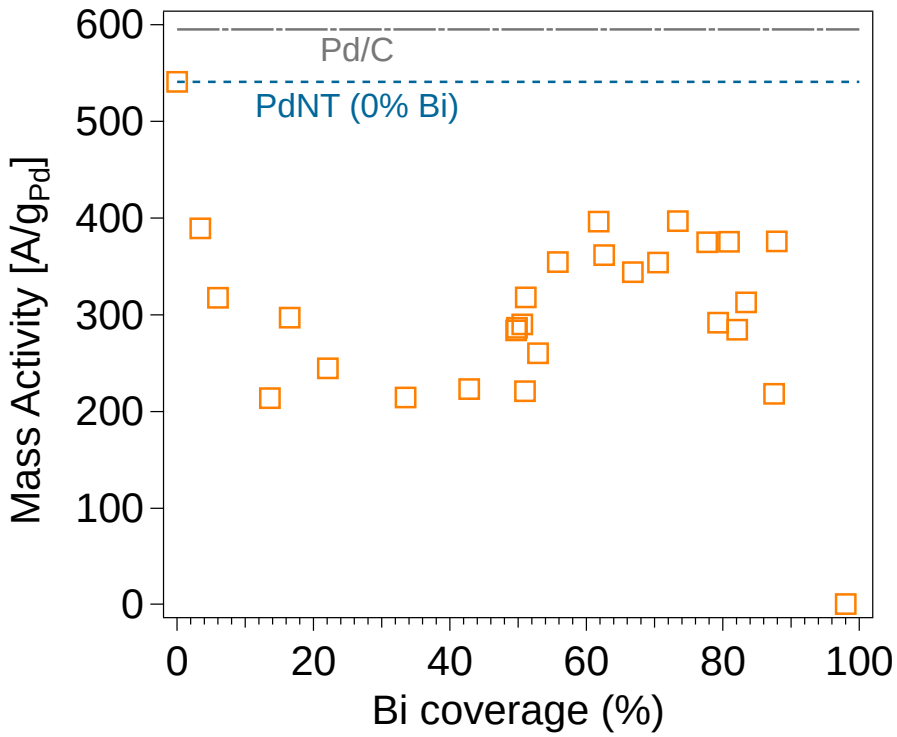

Figure 4.9. Scatter plot of mass activity of PdNTs as a function of their surface Bi coverage (in percent). The mass activity is reported at 0.3 V vs. RHE from voltammograms recorded in 0.5 M H_2SO_4 and 0.5 M HCOOH at 20 mV/s. The blue dashed line corresponds to the mass activity of Bi-free, 500°C PdNTs and the gray dash-dot line represents the specific activity of Pd/C, both also reported at 0.3 V vs. RHE.

effect from the addition of Bi adatoms to high coverage on the PdNTs promises improvements in stability by limiting the formation of poisoning intermediates.[157,158]

Prior to the addition of Bi adatoms, the annealed PdNTs are highly active for formic acid oxidation and have considerably higher specific activities than the commercial, carbon-supported Pd catalyst. Cyclic voltammograms of area-normalized currents for the electro-oxidation of formic acid by annealed and Bi-modified PdNTs are compared to Pd/C in Figure 4.10. The PdNTs annealed at 500°C have nearly 2.5 times the specific activity and comparable mass activity to the commercial Pd/C despite reductions in electrochemically active surface area. The specific and mass activities of the experimental and commercial catalysts are reported in Table 4.1.

The formic acid oxidation activity of the PdNTs increased with elevating the heat treatment temperature. The PdNTs annealed at higher temperatures exhibited negative shifts in their peak current potential for formic acid oxidation and increased activity at 0.3 V, which may be a result of grain growth and an associated increase in the expression of more active, low energy crystal planes as their surfaces become more coordinated.[28,183–185] Observations in the cyclic voltammograms in acid found in Figure 4.6A suggest that general particle size-dependent crystallographic changes are present in the PdNTs after thermal treatments at elevated temperatures. Particle size effects have previously been

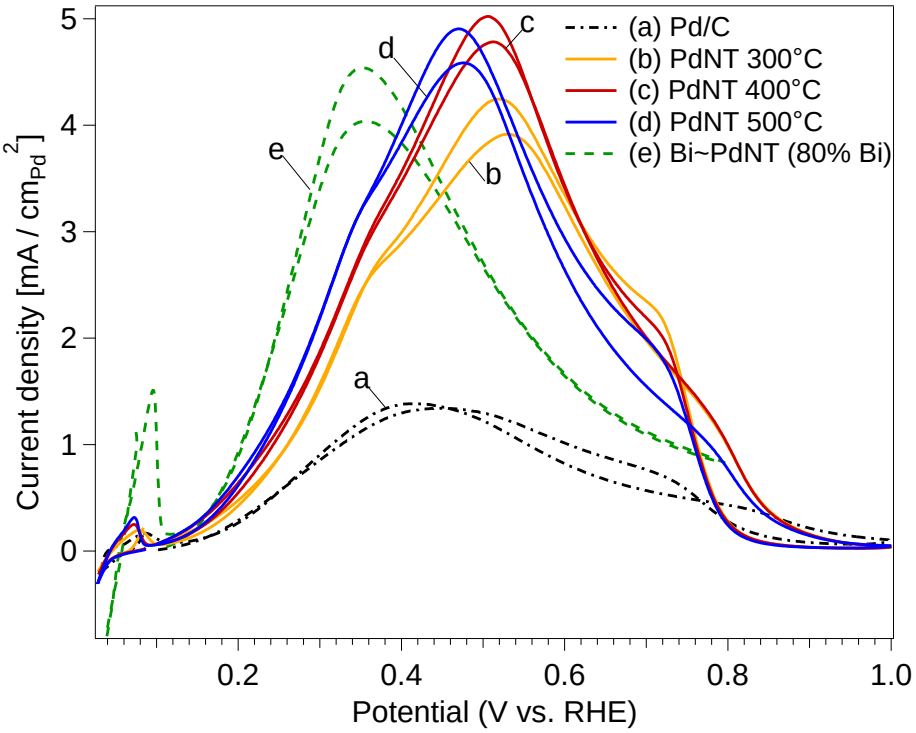

Figure 4.10. Area-normalized cyclic voltammograms recorded at 20 mV/s in 0.5 M H_2SO_4 and 0.5 M HCOOH for (a) commercial, carbon-supported Pd (20 wt% Pd), PdNTs annealed at (b) 300°C, (c) 400°C, (d) 500°C, and (e) Bi-decorated PdNTs annealed at 500°C. Voltammograms are normalized to available Pd area. Labels point to anodic scans of voltammograms.

reported for Pd for formic acid oxidation, with nanoparticles of intermediate size (5-9 nm) considered most active.[57,69] The two most active, Bi-free PdNTs tested in this work were those annealed at 400°C (5.8 nm) and 500°C (11.6 nm) and their calculated grain sizes correspond loosely to the range of particle sizes reported to be most active for carbon-supported Pd nanoparticles.[57,69]

The long-term stability of a catalyst is critical for its application within a direct formic acid fuel cell. Chronoamperometry is used to assess the stability of unmodified PdNTs annealed at 500°C, Bi-modified PdNTs (80% Bi) and the commercial Pd/C by a 24 hour potential hold at 0.2 V vs. RHE, shown in Figure 4.11. Though the PdNTs annealed at 500°C [Figure 4.11(b)] were highly active for formic acid oxidation, these extended surface catalysts destabilized rapidly over the course of the chronoamperometry experiment and were completely deactivated after 3 hours. However, the modification of their surfaces with Bi adatoms [Figure 4.11(a)] drastically improved catalyst stability without significant penalty in mass activity. After one hour of the potential hold at 0.2 V the Bi-modified PdNTs (93.4 A/g_{Pd}) maintained a higher mass activity than Bi-free PdNTs (77.0 A/g_{Pd}) and the commercial Pd/C (79.7 A/g_{Pd}). After 3 hours, the Bi-modified PdNTs (80% Bi) maintain 5 times area-normalized current density as Pd/C [Figure 4.11(c)], while in the same time frame the unmodified PdNTs completely deactivated. The Bi-modified PdNTs continued to outperform Pd/C by a factor of two after 24 hours.

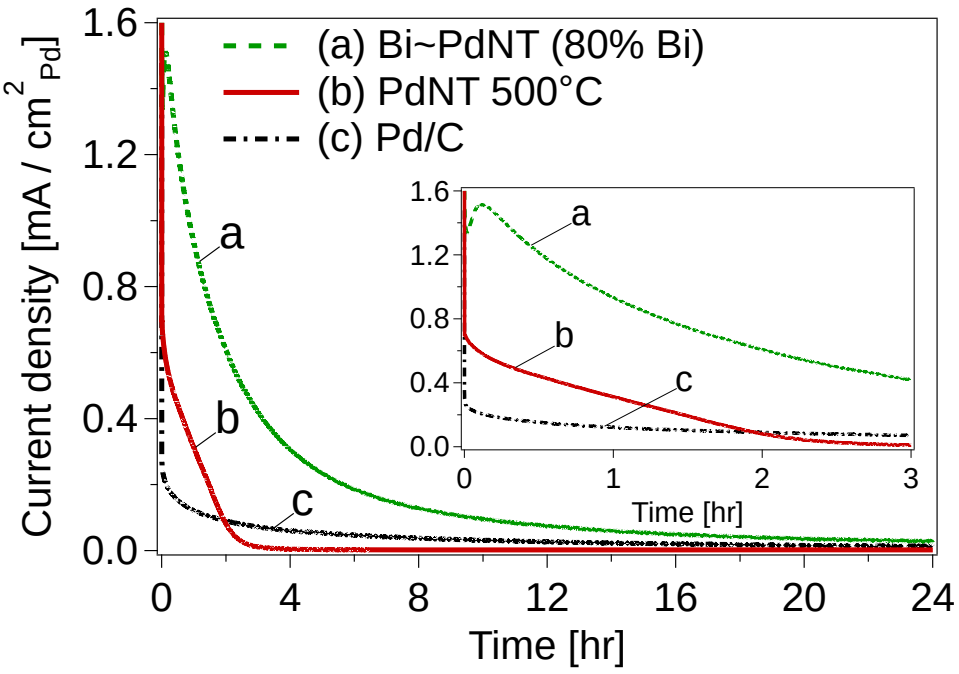

Figure 4.11. Chronoamperometric hold at 0.2 V vs. RHE in 0.1 M $HClO_4$ and 1.0 M HCOOH without rotation. The current is normalized by the sample ECSA, which refers to available Pd.

A comparison of the cyclic voltammograms recorded immediately before and after the chronoamperometry (CA) experiment offers insight into the various destabilization modes operative for the different catalysts. In Figure 4.12(A), it is apparent from the reduction in area of the Bi oxide peak in the first voltammogram following the chronoamperometry experiment [Figure 4.12(A,b)] that Bi has desorbed from the catalyst surface during the stability experiment similar to that observed previously for Bi-modified Pd/C.[152] The emergence of the H-desorption features between 0.2 and 0.4 V in the first cycle following the CA experiment [Figure 4.12(A,b)] also indicate that more Pd sites are exposed as the initial Bi coverage decreased from 80% to ~23%. This results in a suboptimal Bi coverage that we have shown to be less effective at promoting formic acid oxidation on these PdNTs than higher Bi adatom coverages. This is evident in Figure 8, as the formic acid oxidation activity decreases with reductions in surface Bi coverage below 80%.

The 500°C PdNT in Figure 4.12(B) appears to have been inhibited by the formation of site-blocking adsorbates during the chronoamperometry experiment. The hydrogen desorption peaks initially observed on its clean surface prior to chronoamperometry are suppressed in the first voltammogram following chronoamperometry. The large oxidation feature at 0.87 V in this first cycle following chronoamperometry [Figure 4.12(B,b)] is thought to correspond to the removal of carbon monoxide.[186] There is also a noticeable oxidation feature at

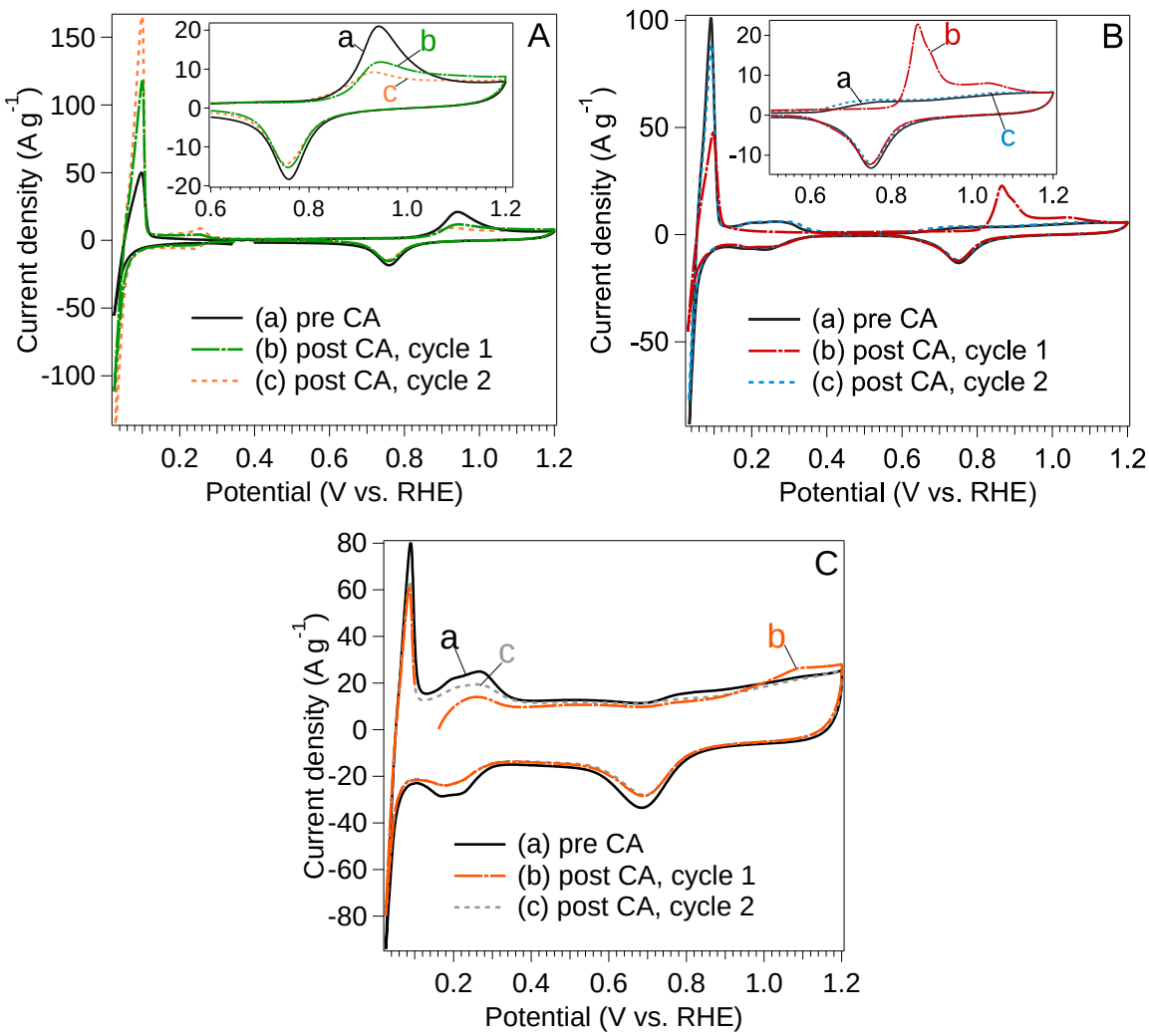

Figure 4.12. Cyclic voltammograms recorded in 0.1 M $HClO_4$ electrolyte at 20 mV/s for (A) Bi-modified PdNTs (80% Bi), (B) 500°C PdNT, and (C) Pd/C immediately before and after a 24 hour chronoamperometric hold at 0.2 V in 0.1 M $HClO_4$ and 1.0 M HCOOH.

1.05 V in the first scan following CA that is attributed to an interaction of palladium oxides and adsorbed intermediates.[29] Cycling this electrode once effectively cleaned its surfaces, as its second cyclic voltammogram following chronoamperometry [Figure 4.12(B,c)] was nearly indistinguishable from the voltammogram recorded prior to the stability experiment; the initial catalyst surface was restored after oxidizing the accumulated adsorbed species.

The Pd/C also lost activity during the CA experiment as a result of surface coverage by adsorbates as well as by a physical degradation that was not observed for the nanotube samples. In the first cycle after chronoamperometry [Figure 4.12(C,b)], the Pd/C has a small oxidation feature at 1.05 V described above for the unmodified PdNTs. Additionally, there were considerable decreases in the charges of the Pd oxide reduction peak and the hydrogen desorption features that were not restored with cycling. This indicates a reduction in catalyst surface area and is likely the consequence of Pd dissolution into the acidic electrolyte.[142,187] Unlike the two PdNT samples, those with and without Bi modification, cycling the Pd/C electrode was not observed to restore the initial surface of the catalyst.

Conclusion

Palladium nanotubes were synthesized within alumina templates by a novel chemical vapor deposition technique from palladium acetylacetonate precursors at relatively low temperatures. The metal nanotubes were thermally

annealed in a range of temperatures up to 500°C in 4% H_2. The thermal treatment promoted a series of changes to the morphologies and surfaces of the nanotubes. The Pd nanotubes, agglomerates of fine Pd nanoparticles after synthesis, underwent grain growth with increases in heat treatment temperature, and ultimately, displayed improved specific activity for the oxidation of formic acid. The palladium nanotubes annealed at 500°C (2.19 mA/cm^2) are 2.4 times more active than commercially available, carbon-supported Pd (0.91 mA/cm^2) at 0.3 V vs. RHE.

The adsorption of Bi to the Pd nanotubes significantly improved their formic acid oxidation activity and stability. A maximum in specific activity of Bi-decorated Pd nanotubes was observed at 80% Bi coverage and these optimum Bi-modified PdNTs (3.75 mA/cm^2) were over 4 times as active as Pd/C and nearly twice as active as the unmodified PdNTs at 0.3 V vs. RHE. The addition of Bi adatoms was observed to drastically reduce the accumulation of site-blocking intermediates on the surface of the Pd nanotubes during chronoamperometry experiments, improving catalyst stability remarkably. The Bi-modified PdNTs were 5 times as active as Pd/C after 3 hours of a chronoamperometric hold at 0.2 V vs. RHE. In the same amount of time, Bi-free PdNTs deactivated completely, which was the result of surface coverage by reaction intermediates. These results strongly imply that the adsorption of Bi to the Pd nanotubes promotes the

direct oxidation of formic acid by promoting a preferred molecule binding geometry.

CHAPTER 5

PLATINUM AND PALLADIUM OVERLAYERS DRAMATICALLY ENHANCE THE ACTIVITY OF RUTHENIUM NANOTUBES FOR ALKALINE HYDROGEN OXIDATION

Abstract

Templated vapor synthesis and thermal annealing were used to synthesize unsupported metallic Ru nanotubes with Pt or Pd overlayers. By controlling the elemental composition and thickness of these overlayers, we obtain nanostructures with very high alkaline hydrogen oxidation activity. Nanotubes with a nominal atomic composition of $Ru_{0.90}Pt_{0.10}$ display a specific activity (2.4 mA/cm^2) that is 35 times greater than that of pure Ru nanotubes at a 50 mV overpotential, and nearly 5 times greater than that of carbon-supported Pt nanoparticles (0.51 mA/cm^2). The surface-segregated structure also confers dramatically increased Pt utilization efficiency. We find a platinum-mass normalized activity of 1,240 A/g_{Pt} for the optimized nanotube versus 280 A/g_{Pt} for carbon-supported Pt nanoparticles. We attribute these enhancements to the atomic-scale homeomorphism of the nanotube form factor with adlayer-modified polycrystals, which have allowed us to observe both theoretical rate-determining steps proposed in the literature.

Introduction

With recent advances in stable and conductive alkaline anion exchange membranes (AAEMs),[10] alkaline anion exchange membrane fuel cells (AAEMFCs) have emerged as an alternative technology to proton exchange membrane fuel cells (PEMFCs). The relatively less corrosive environment of

AAEMFCs allow for inexpensive oxygen reduction reaction (ORR) electrocatalysts, such as silver,[188] without the concern of membrane fouling from catalyst dissolution during operation. This advantage, however, is obviated by the slow hydrogen oxidation reaction (HOR) kinetics at the anode where the gains at the cathode are offset by a 100-fold reduction in the anodic exchange current density.[189] Creating suitable HOR catalysts for alkaline pH is required to fulfill the promise of AAEMFCs.

Two different hypotheses have been proposed in the literature to describe routes to improved HOR activity and paths towards more active catalysts. The first details a bi-functional route whereby promoting hydroxyl adsorption onto the electrocatalyst surface enhances HOR activity by clearing active sites for slow dissociative hydrogen adsorption.[190] Alternatively, it has been proposed that an electronic modification of the electrocatalyst surface to reduce H-binding energy accelerates the HOR.[191] We previously addressed the observed enhancement in the electrocatalytic HOR activity of Ru_xPt_y and Ru_xPd_y alloy nanoparticles (NPs) in rotating-disc electrode measurements in 0.1 M KOH.[54] As the binding energy of hydrogen was reduced, hydrogen dissociative adsorption (Tafel step) emerged as rate limiting on Pt-Ru nanoparticles.[192] However, in the case of Pd-Ru, the hydrogen binding energy was not sufficiently reduced to observe the emergence of H_2 dissociative adsorption as rate limiting. In this way, we have observed both

ligand and bi-functional effects in the alloy nanoparticles via the characteristic differences in the electrochemical kinetic data.

Our results in the case of supported nanoparticle catalysts motivated us to investigate systems with greater structural clarity to probe the effects of the Pt and Pd additions to Ru. Foundational work has been performed for decades using bulk-like polycrystals, and recent studies have shown that adlayers can modify the properties of the combined materials significantly in comparison with the bulk. Examples include monometallic and mixed monolayers of Pt on Ru,[86,193] Pd,[194,195] and Ni,[196] as well as Bi on Pt[197] and Co on Pt[198,199]. Ligand effects have been enhanced further for select electrochemical reactions (e.g., alcohol oxidation) when the proximal distribution of bi-functional active sites is carefully controlled via submonolayer coverage. A classic example is found in enhanced ethanol oxidation by co-locating oxophilic atoms, such as Sn, near Pt active sites.[200–202] The challenge has been translating these effects into comparably active high-surface-area catalysts. We thus consider the case of so-called extended surface catalysts, which bridge the gap between polycrystals and nanoparticles. These are essentially hybrid materials, retaining the high surface-specific activity and stability of the bulk while attaining the high surface areas of nanostructured practical catalysts.

Techniques for generating thin overlayers (or shells) include galvanic displacement,[48,203] chemical processing,[84,204] or metal-ligand-mediated solution

phase synthesis[205]. We have developed an entirely physical synthesis approach based on vapor deposition from metalorganic precursors on functional supports or monolithic sacrificial templates. This approach can be used to fabricate multicomponent highly dispersed or conformal coatings on arbitrary supports simply and effectively.[53,106,117,174,206] Subsequent heat treatments and/or sequential metal deposition can be used to produce core-shell structures as well as overlayers on high-surface-area catalysts. In this contribution, we describe the synthesis of fractional overlayers of Pt or Pd on Ru nanotube analogs of extended polycrystalline surfaces and apply these catalysts to the electrochemical hydrogen oxidation reaction (HOR) in alkaline electrolyte, shown schematically in Figure 5.1.

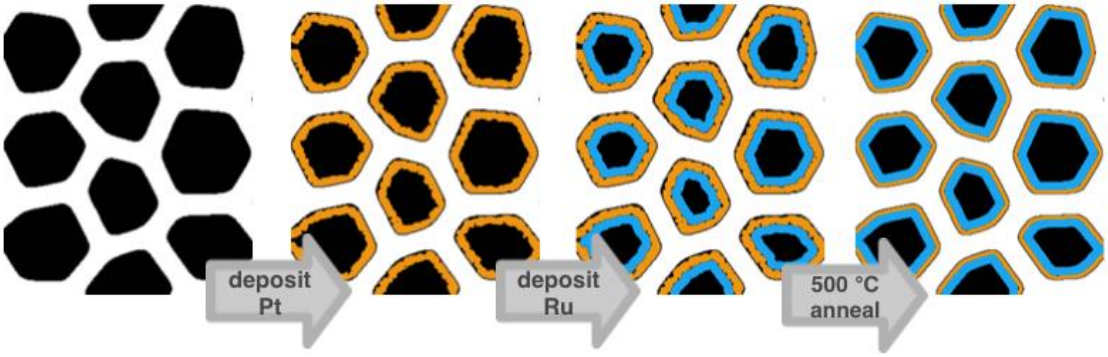

Figure 5.1. Synthesis scheme illustrating the sequence of precursor deposition used to make bi-metallic nanotubes. Following the annealing, the nanotubes are separated from the template in 30% KOH, then analyzed using microscopic, spectroscopic, and electrochemical techniques.

Experimental

Platinum-Ruthenium and Palladium-Ruthenium Nanotube Synthesis

Platinum-ruthenium and palladium-ruthenium nanotubes were synthesized by consecutive vapor depositions, first of platinum or palladium, and followed by ruthenium, in a modified chemical vapor deposition technique described previously for the synthesis of Pt-rich, alloyed PtRuNTs.[164] For these Ru-rich PtRuNTs and PdRuNTs, the more noble of the metals in the nanotube samples was deposited first within the channels of a porous anodic alumina (AAO) membrane (Whatman Anodisc, 13 mm diameter, 200 nm pore size), seeding the template for the subsequent deposition of ruthenium in a separate vapor deposition. Each isolated precursor powder (Alfa Aesar) was contained under the template prior to a mild heat treatment under vacuum and ranging in temperature from 160°C for palladium acetylacetonate to 210°C for platinum acetylacetonate and 240°C for ruthenium acetylacetonate. The masses of the metalorganic precursors applied were adjusted to control the amounts of the metals deposited for a range of Ru-rich compositions. Pure metal samples were also prepared by the lone addition of the metal to the alumina template in a single vapor deposition experiment. After 15 hours at the appropriate temperature for precursor sublimation and metal deposition within the templates, the oven was evacuated and flushed with dry N_2 several times and cooled to room temperature. Finally,

the mass of the deposited metal was measured to determine the nominal composition of the nanotube sample that was later confirmed by SEM-EDS.

Ruthenium was deposited as a hydrous oxide along the Pt- or Pd-lined template walls,[164] and after vapor deposition of the materials, the templates were thermally annealed in a reducing atmosphere to induce morphological transitions, oxide reduction, and grain growth. The metal-lined templates were annealed in a quartz tube furnace with a flowing 4% H_2 environment at 500°C for 1 hour using a programmed temperature ramp rate of 5°C/min. To characterize the nanotubes for further study, the sacrificial alumina templates were dissolved in KOH, the liberated nanotubes were settled passively, and the supernatant solution was decanted and replaced with water until the suspension reached a neutral pH.

Electron Microscopy *Scanning Electron Microscopy* (SEM) images were obtained with a ZEISS 1525 Field Emission SEM at an accelerating voltage of 3 kV using an in-lens electron detector. SEM-EDS measurements of nanotube chemical compositions were conducted at an accelerating voltage of 20 kV.

Transmission Electron Microscopy A Hitachi NB-5000 focused ion beam (FIB) instrument was used to prepare thin cross-sections of the PtRuNTs and PdRuNTs in the AAO template for scanning transmission electron microscopy (S/TEM) imaging and EDS mapping with a JEOL 2200FS operating at 200 kV.

X-ray Diffraction *(*XRD) patterns were recorded with a Bruker Phaser D2 diffractometer using Ni-filtered Cu Kα radiation (λ = 0.154184 nm, 30 kV, 10 mA,

0.014° step, 0.5 s/step) in the Bragg-Brentano geometry fitted with a 0.6 mm antiscatter slit in the incident beam and a 2.5° Soller slit in the diffracted beam. The position and width of diffraction peaks were obtained by fitting to Voigt functions using IGOR Pro (Wavemetrics, Inc.).

X-ray Absorption Spectroscopy (XAS) experiments were conducted at beamline 20-BM at the Advanced Photon Source at Argonne National Laboratory (Argonne, IL, USA). Pre-edge correction, normalization, and post-edge subtraction via spline fitting were done in Athena.[165] The k^2-weighted $\chi(k)$ forward Fourier transform (FT) parameters were: k-weight, 0.5; window, Hanning; k-range, 22 – 16 Å-1. The k^2-weighted $\chi(R)$ backward FT parameters were: R-range, 1.5 – 3 Å; window, Hanning. Atomic first-shell scattering paths were determined for tetrahedral geometry (face-center, close-packed systems) for the Pt, Pd, and Ru EXAFS data in Artemis and were used in FEFF[207] to determine scattering paths. Interference patterns were simulated simultaneously for all possible metal-metal scattering paths and parameters were fit in Artemis.[208]

Electrochemical Characterization Electrocatalysts were tested at room temperature in a standard three-electrode electrochemical cell (Pine Instruments) with a double-junction Ag/AgCl reference electrode (Pine Instruments) and Pt-wire counter electrode in H_2-saturated, 0.1M potassium hydroxide (semi-conductor grade, Sigma-Aldrich). Electrodes were made by depositing well-dispersed catalyst nanotubes onto glassy-carbon electrodes (A = 0.196 cm^2) for

a target catalyst load of ~7μg Pt-group metal/cm^2. Polarization curves were obtained over the range –0.1 – 1.025 V vs. RHE using a Bio-Logic VMP3 research-grade, multi-channel potentiostat with EC-Lab software. Potentiostatic electrochemical impedance spectroscopy (EIS) spectra were recorded from 200 kHz to 1 Hz at 0.4 V vs. RHE with a 10 mV sine perturbation amplitude under H_2 mass transport limited conditions and 1 atm H_2. The high-frequency intercept of the EIS spectrum was used to eliminate the ohmic resistance of the electrochemical cell from the polarization curves. Electrochemical active surface areas (ECSAs) were obtained using Cu-stripping techniques.[128]

Results and Discussion

Vapor-phase deposition yields uniform, nanoscale, 2D catalysts with high activity from as-received precursors that mimic extended polycrystalline surfaces allowing for fine discrimination in the geometric and electronic characteristics important to various electrochemical reactions. Conformal coatings of Pt or Pd are first vapor-grown within the channels of a porous anodic alumina template. Following the deposition of the more-noble outer layer, Ru is deposited in the channels. HAADF S/TEM and EDS map images for cross-sections of the PtRuNTs and PdRuNTs embedded within the alumina template are shown in Figure 5.2 following heat treatment. The aluminum and oxygen maps in Figure 5.2 identify the porous alumina template. The nanotubes take a shape conformal

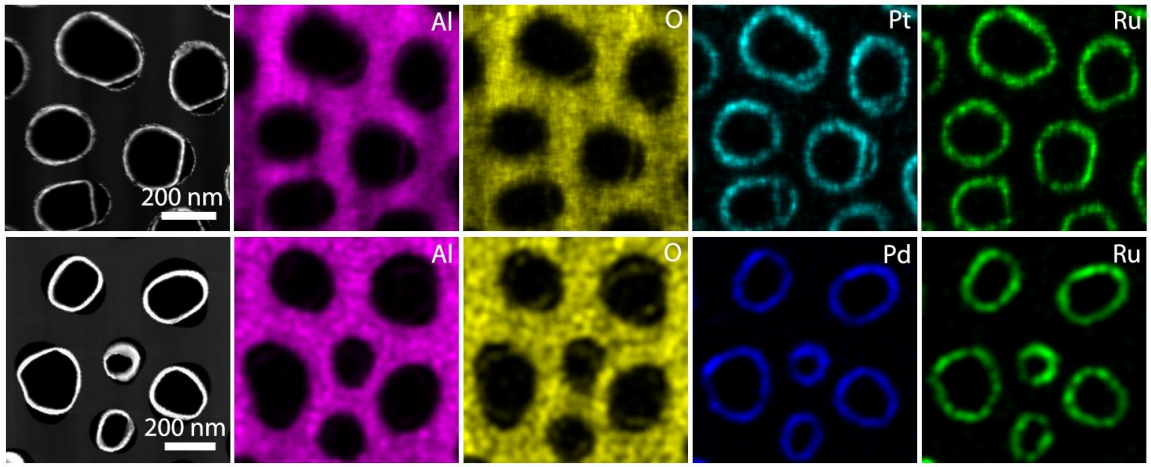

Figure 5.2. HAADF S/TEM and EDS map images of FIB cross-sections of (top) PtRuNTs (19% Pt) and (bottom) PdRuNTs (22% Pd) in the anodic alumina template.

to the template walls while the metal pairs are in close proximity. The nanotube samples were harvested for further study of the microstructures and for electrochemical characterization by dissolving the sacrificial template in KOH.

The SEM images in Figure 5.3 illustrate the high aspect ratio of the nanotube catalysts with lengths ranging from 2-20 μm that are roughly 200 nm in diameter with wall thicknesses of 10-15 nm. These results are consistent with previous applications of this technique.[164] As-synthesized, the nanotubes are nano-particulate aggregates of 3-5 nm particles of the discretely layered materials. Following a thermal treatment at 500°C, considerable Ru grain growth

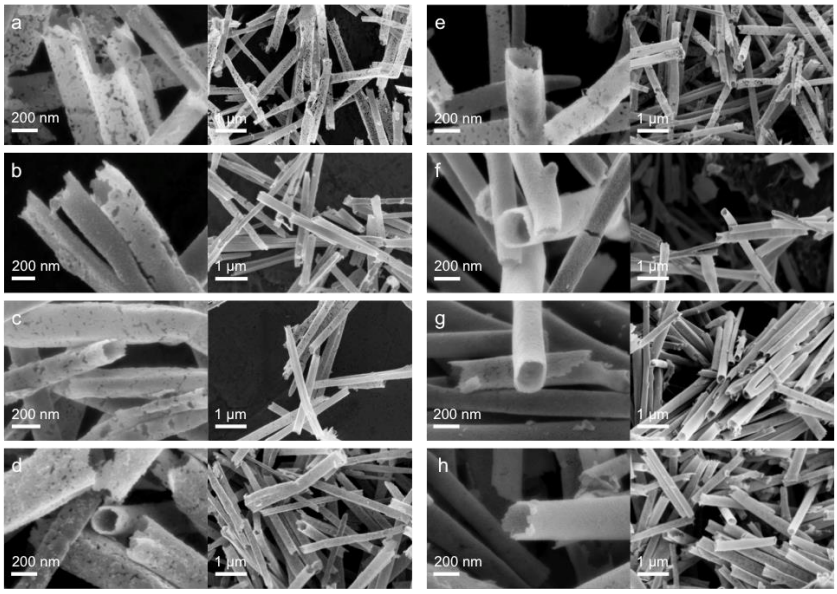

Figure 5.3. SEM images of PtRuNTs with (a) 4% Pt, (b) 7% Pt, (c) 10% Pt, and (d) 19% Pt, and PdRuNTs with (e) 7.5% Pd, (f) 18% Pd, (g) 19% Pd, and (h) 22% Pd after heat treatment.

results that is also accountable for the nanoscale porosity observed in the nanotube walls as the small crystallites coalesce and form larger crystalline grains with smoother surfaces. The nanoscale porosity between the contiguous grains will be shown to account for the high coordination, specific activity, and surface area of these nanotube catalysts. SEM images of the monometallic (Pt, Ru, Pd) nanotube control samples are shown in Figure 5.4.

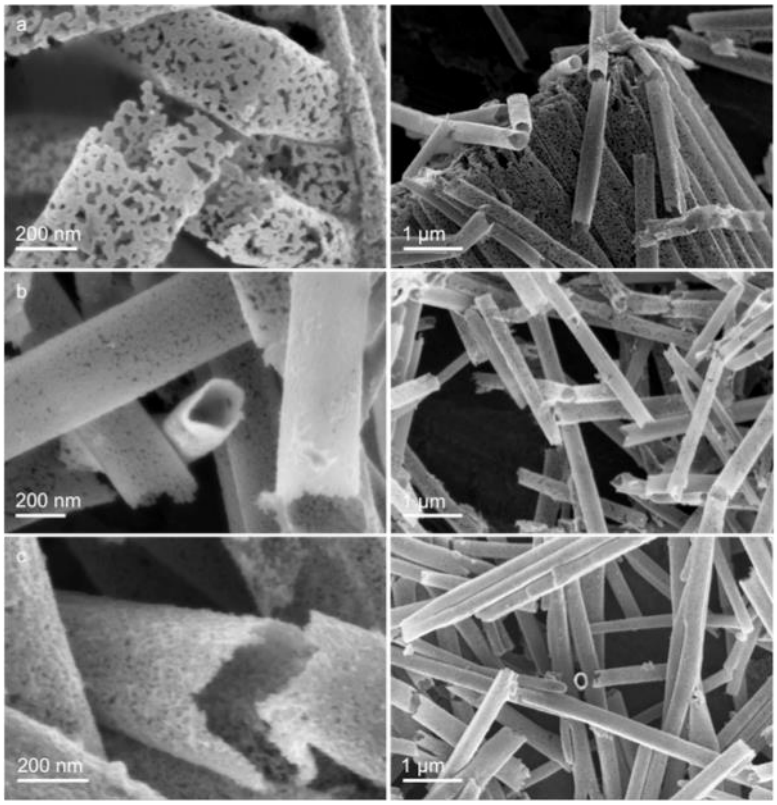

Figure 5.4. SEM images of the monometallic nanotubes used as controls: (a) PtNT, (b) RuNT, (c) PdNT. All samples are annealed at 500°C in 4% H_2.

The heat-treated nanotubes have nano-sized grains approximately the same thickness as the nanotube walls with the hcp crystal structure of the Ru nanotube as illustrated in Figure 5.5. Energy dispersive spectroscopy (EDS) was used to confirm the relative atomic composition of the nanotubes, while a simple Vegard's law approach[174] was used to investigate the degree of alloying. Above each diffraction pattern in Figure 5.5 is the respective sample's nominal composition (given on the left) and the composition calculated from the hcp (100) peak position using Vegard's law (given on the right).

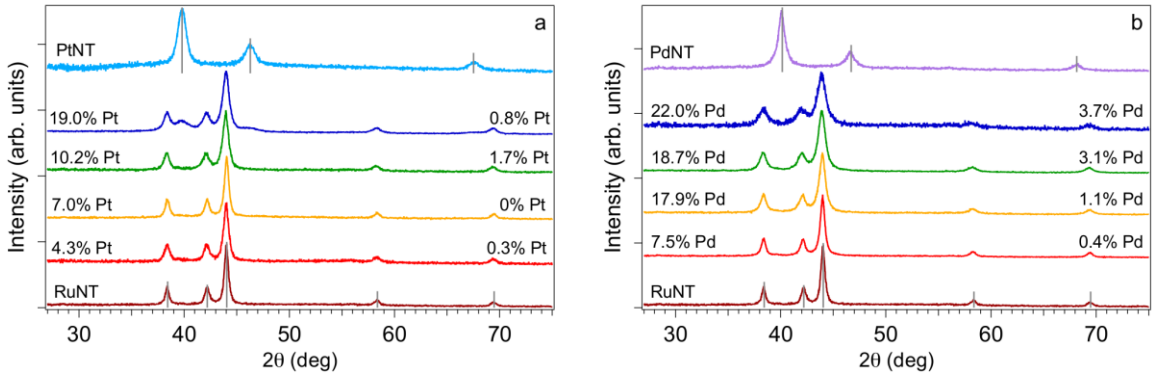

Figure 5.5. Cu Kα XRD patterns for the (a) PtRuNTs and (b) PdRuNTs with reference spectra for the monometallic RuNT, PtNT, and PdNT included. Above the respective spectra, the nominal composition is reported on the left while composition determined using Vegard's law is given on the right. Pure metal peak positions with relative intensities (gray sticks) are included for reference (Ru: PDF 00-006-0663; Pt: PDF 00-004-0802; Pd: PDF 00-005-0681).

As expected based on the nominal composition, the hcp phase is the dominant crystal structure but it lacks the lattice expansion that would be expected if the nanotubes were alloyed. The compositions calculated from shifts of the hcp (100) diffraction peak are suggestive of significant phase segregation in the nanotubes. Thermodynamic calculations and experimental evidence suggest that over 90% of the Pt is expected to phase segregate.[209] The tendency to segregate for the PdRuNTs is expected to be even stronger.[209–212] Thermodynamics and sequential chemical vapor deposition both here favor the tendency to maintain segregated structures.

The results of a Scherrer analysis indicate no large differences between measured grain sizes for each of the Ru diffraction peaks suggesting that the high aspect ratio of these vapor-grown nanotubes does not cause grain anisotropy. Grain size results for the different lattice directions are reported in Table 5.1. For high Pt fractions where complete overlayer coverage is found, the diffraction pattern for the 19% Pt sample also contains a distinct and broad (111) diffraction peak attributed to discrete Pt islands in addition to the conformal overlayer. The broad Pt (111) peak suggests small grain sizes for Pt relative to the much larger Ru grains.

Electronic interactions, probed using x-ray absorption near edge spectroscopy (XANES), reveal that the Ru phase behaves like Ru foil while Pt and Pd phases show increased valance band filling and lattice compression. For

Table 5.1. Scherrer analysis of all Ru hcp peaks of the X-ray diffraction patterns for pure RuNT, PtRuNTs and PdRuNTs annealed at 500°C in 4% H_2.

Sample	t(100) (nm)	t(002) (nm)	t(101) (nm)	t(102) (nm)	t(110) (nm)
RuNT	22.1	15.3	18.5	16.2	16.0
PtRuNT (4% Pt)	15.7	14.7	14.7	12.9	14.7
PtRuNT (7% Pt)	17.7	15.9	17.4	15.4	17.8
PtRuNT (10% Pt)	14.6	11.6	13.2	11.9	12.2
PtRuNT (19% Pt)	12.4	6.7	11.8	10.2	12.1
PdRuNT (7.5% Pd)	17.5	16.4	17.2	15.2	16.8
PdRuNT (15% Pd)	13.2	11.4	12.2	10.5	11.7
PdRuNT (19% Pd)	11.4	10.4	11.0	9.2	10.4
PdRuNT (22% Pd)	8.6	7.8	8.9	8.0	7.2

all of the bi-metallic nanotube samples, regardless of composition, the Ru electronic structures are virtually indistinguishable from Ru foil and pure Ru nanotubes, as illustrated in Figure 5.6. Such behavior indicates that the Ru phase is predominately metallic without metal oxide or alloy formation.

In the PtRuNTs, the Pt L_3 edge probes the majority of available electronic transitions in its bonding d-orbital and reductions in the observed white line intensity vs. Pt foil are consistent with electron donation from Ru to Pt.[213,214] Analogous behavior in the PdRuNTs at the Pd K edge cannot be observed because K edge transitions do not probe electron promotion into *d*-orbital vacancies in Pd.

Some structural information can also be obtained from the near edge data. The Pt and Pd white line peaks broaden in both sets of bi-metallic nanotubes. In this case, the broadening is a subtle and significant distinction from a shift of the white line to lower energies. Here, peak broadening indicates lattice compression of the Pt or Pd from the underlying large Ru grains. Calculations have shown that metal *d*-bands expand and become less tightly bound as metal lattices are compressed.[212] Such behavior would lead to broadening of the Pt and Pd white line peaks here without a shift of the white line peak energy.[212] As Pt or Pd composition increases, the white line peaks progressively broaden. This behavior is consistent with increased inter-atomic compressive forces in more complete overlayers. Examples of changes in XANES for compressive or tensile strain

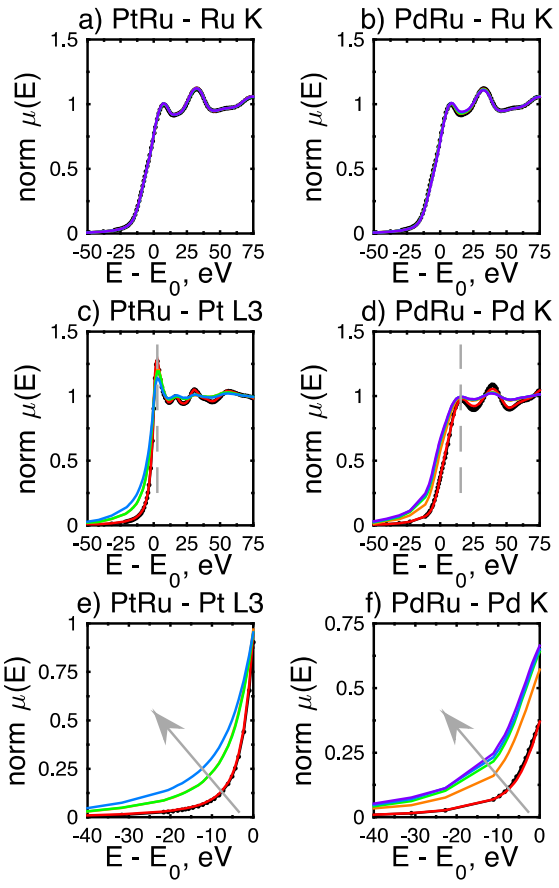

Figure 5.6. Normalized XANES spectra for the PtRuNTs (a,c,e) and PdRuNTs (b,d,f) nanotubes at the Ru K (a-b), Pt L_3, (c, e) and Pd K (d, f) edges. Gray lines (dashed) in (c) and (d) are to guide the eye to the center of the white line peak. Data for the reference foils (black •••) and the respective pure metal nanotubes (red) are included in each figure for comparison. Key: $Ru_{0.93}Pt_{0.07}$ (orange), $Ru_{0.87}Pt_{0.13}$ (green), $Ru_{0.69}Pt_{0.31}$ (blue); $Ru_{0.93}Pd_{0.07}$ (orange), $Ru_{0.85}Pd_{0.15}$ (green), $Ru_{0.80}Pd_{0.20}$ (blue), $Ru_{0.77}Pd_{0.23}$ (violet). Gray arrows indicate increasing Pt (e) or Pd (f) composition and increased peak broadening in the enlarged pre-edge XANES spectra for the Pt L_3 and Pd K edges, respectively.

have been presented in the literature; however, this data represents a more definitive example than is typically presented and represent a strength of this synthesis technique to investigate phase-segregated structures.[215–217]

For both the Pt L_3 and Pd K XANES behavior, we conclude that electron density is transferred from the Ru to the Pt or Pd and that there is evidence of compressive strain in the Pt and Pd suggestive of segregation of tightly bound Pd or Pt atop Ru nanotubes. We expect that electron donation from the Ru to the Pt or Pd would reduce the H-binding energy leading to improved HOR activity. Additionally, compressive strain should increase hybridization at the valence band from expanded *d*-orbitals that should lead to increased electron filling and reduced interaction energy with adsorbed hydrogen. In both cases of compressive strain and electron donation from Ru to the surface metal, increased activity would be observed for the bi-metallic nanotubes versus the pure metal counterparts.

The XANES observations are corroborated with atomic spacing information obtained using the forward Fourier transforms of the extended X-ray absorption fine structure (EXAFS) spectra, illustrated in Figure 5.7. Ru K edge EXAFS for all of the Ru-containing nanotubes show only Ru-Ru bonding interactions with no shifts related to either alloying or lattice strain.

Pd K edge EXAFS show a compressed Pd-Pd first-shell scattering path. Estimations of bond lengths for the Pd-Pd scattering path from fitted spectra are

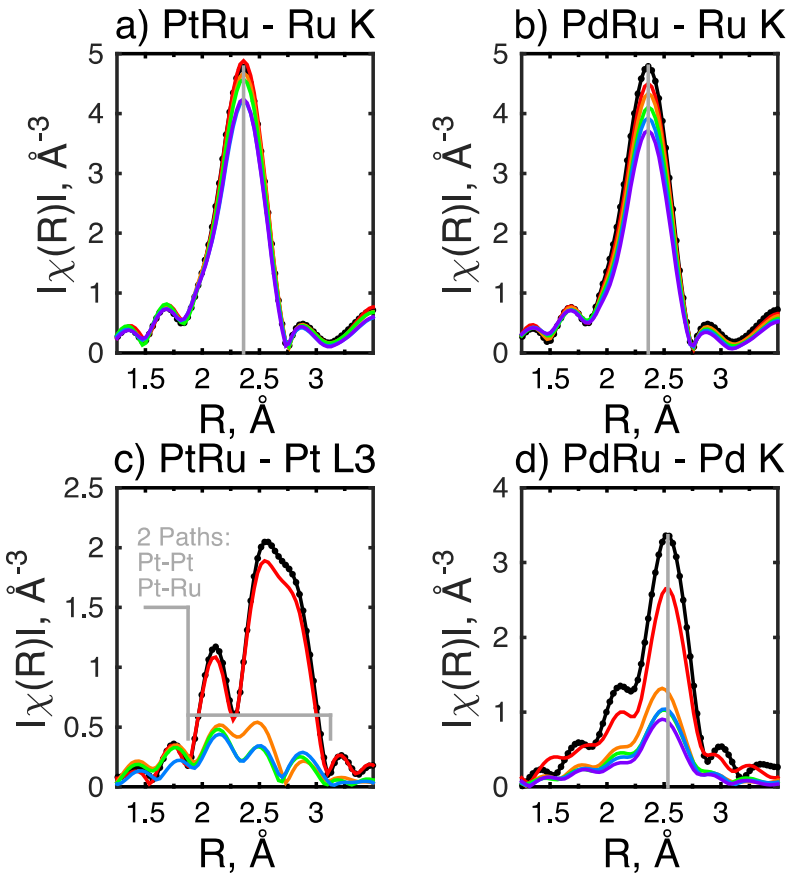

Figure 5.7. Forward Fourier transforms of the EXAFS for the PtRuNTs (a,c) and PdRuNTs (b,d) at the Ru K (a-b), Pt L_3, (c) and Pd K (d) edges. Data for the reference foils (black •••) and the respective pure metal nanotubes (red) are included in each figure for comparison. The gray guides in (a, b, d) are guides to the center of the first-shell scattering path. The transform magnitude related to the 2 paths present in (c) are indicated by the gray guides. Key: $Ru_{0.93}Pt_{0.07}$ (orange), $Ru_{0.87}Pt_{0.13}$ (green), $Ru_{0.69}Pt_{0.31}$ (blue); $Ru_{0.93}Pd_{0.07}$ (orange), $Ru_{0.85}Pd_{0.15}$ (green), $Ru_{0.80}Pd_{0.20}$ (blue), $Ru_{0.77}Pd_{0.23}$ (violet).

~98.5% of the bond length in pure Pd foil, indicative of substantial compressive strain in the Pd surface layer of the PdRuNTs. Such behavior, when considered with the Ru K edge EXAFS, suggests complete phase segregation between Pd and Ru in the PdRuNTs. Additionally, the reduction in the intensity of the Pd-Pd first-shell scattering path is consistent with lesser-coordinated, nano-sized grains as might be expected from a fractional overlayer. Examples of the EXAFS quality, as well as the Pt-Pt and Pt-Ru scattering path fitting, are illustrated in Figure 5.8. Bond lengths and EXAFS parameter fits are given in Table 5.2.

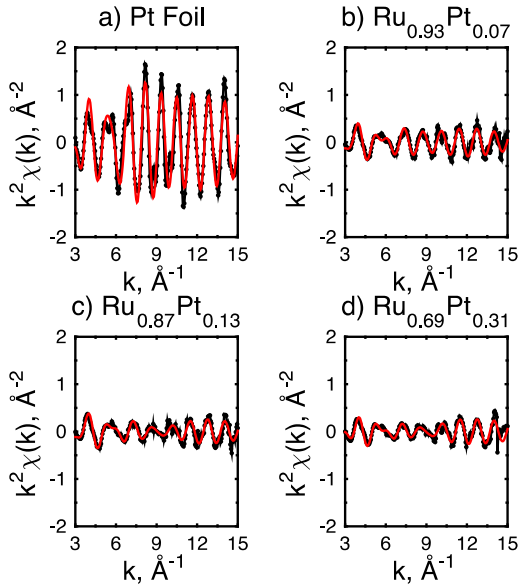

Figure 5.8. k^2-weighted EXAFS at the Pt L3 edge for the Pt foil (a) and the PtRu nanotubes (b-d). The data (black •••) and the fits (red) are represented. The same ordinate limits have been used for all plots to demonstrate the relative scattering amplitude in the EXAFS region for the nanotubes vs. foil.

Table 5.2. EXAFS fits for PtRuNTs, PdRuNTs and monometallic nanotube controls.

Catalyst	Scattering Path	Edge	EXAFS Parameters for indicated first-shell scattering path			
			N	*R* (Å)	σ^2 (Å^2)	ΔE_0 (eV)
Pt foil	Pt-Pt	L_3	12	2.764 ± 0.004	0.0055 ± 0.0002	6.138 ± 0.7881
Ru foil	Ru-Ru	K	12	2.675 ± 0.005	0.0049 ± 0.0003	-5.862 ± 1.068
Pd foil	Pd-Pd	K	12	2.742 ± 0.005	0.0069 ± 0.0003	0.6213 ± 0.7379
Pt tube	Pt-Pt	L_3	11	2.759 ± 0.003	0.0055	5.252 ± 0.8011
Ru tube	Ru-Ru	K	10.7	2.675 ± 0.005	0.0049	-5.629 ± 0.9756
Pd tube	Pd-Pd	K	9.6	2.739 ± 0.003	0.0069	2.514 ± 0.8028
$Ru_{0.93}Pt_{0.07}$	Pt-Pt	L_3	1.9	2.753 ± 0.022	0.0055	6.224 ± 1.218
$Ru_{0.87}Pt_{0.13}$	Pt-Pt	L_3	1.9	2.753 ± 0.007	0.0055	6.197 ± 1.171
$Ru_{0.69}Pt_{0.31}$	Pt-Pt	L_3	1.9	2.763 ± 0.006	0.0055	6.902 ± 0.963
$Ru_{0.93}Pt_{0.07}$	Pt-Ru	L_3	1.3	2.697 ± 0.006	0.0049	6.224 ± 1.218
$Ru_{0.87}Pt_{0.13}$	Pt-Ru	L_3	1.3	2.697 ± 0.006	0.0049	6.197 ± 1.171
$Ru_{0.69}Pt_{0.31}$	Pt-Ru	L_3	1.2	2.701 ± 0.005	0.0049	6.902 ± 0.963
$Ru_{0.93}Pt_{0.07}$	Ru-Ru	K	11.1	2.675 ± 0.005	0.0049	-5.188 ± 0.9788
$Ru_{0.87}Pt_{0.13}$	Ru-Ru	K	10.9	2.675 ± 0.005	0.0049	-5.599 ± 1.011
$Ru_{0.69}Pt_{0.31}$	Ru-Ru	K	10.2	2.675 ± 0.004	0.0049	-6.263 ± 0.8866
$Ru_{0.93}Pd_{0.07}$	Pd-Pd	K	4.2	2.699 ± 0.006	0.0069	1.813 ± 0.9112
$Ru_{0.85}Pd_{0.15}$	Pd-Pd	K	3.3	2.703 ± 0.005	0.0069	3.521 ± 0.7173
$Ru_{0.80}Pd_{0.20}$	Pd-Pd	K	3.3	2.705 ± 0.005	0.0069	3.289 ± 0.8343
$Ru_{0.77}Pd_{0.23}$	Pd-Pd	K	2.9	2.701 ± 0.005	0.0069	1.990 ± 0.8012
$Ru_{0.93}Pd_{0.07}$	Ru-Ru	K	10.3	2.675 ± 0.004	0.0049	-5.357 ± 0.9125
$Ru_{0.85}Pd_{0.15}$	Ru-Ru	K	9.8	2.675 ± 0.004	0.0049	-5.430 ± 0.8517
$Ru_{0.80}Pd_{0.20}$	Ru-Ru	K	9.4	2.675 ± 0.004	0.0049	-6.210 ± 0.8284
$Ru_{0.77}Pd_{0.23}$	Ru-Ru	K	8.9	2.675 ± 0.004	0.0049	-6.568 ± 0.8019

In the PtRuNTs there is evidence of a Pt-Pt scattering path and Pt-Ru scattering paths. These data suggest complete phase segregation of the Pt from the Ru lattice with incorporation of small amounts of Ru into the Pt lattice, consistent with previous experimental data and thermodynamic calculations.[209] There are reductions in Pt-Pt bond length consistent with alloy formation or strain induced from the Ru nanotube support.[218] Estimations of bond lengths for the Pt-Pt scattering path in Pt L_3 edge first-shell fits are approximately 99% of the bond length in pure Pt foil for each of the samples. Because of the small reduction in bond length, the Ru-Pt scattering path is attributed to interfacial Ru-Pt mixing instead of alloy formation, where more dramatic reductions in Pt-Pt bond lengths would be expected. For such structures, the ligand effects would be expected to propagate through the entirety of the Pt overlayer.[209]

We have demonstrated using XAS an ability to manipulate the electronic structure of the Pt and Pd overlayers via strain and ligand effects. The electrochemical data, illustrated in Figure 5.9(a,b), show the influence of Ru on the charging behavior of Pt and Pd with composition-dependent shifts in three important potential regions (V vs. RHE): (1) proton adsorption/desorption (~ 0 – 0.3 V); (2) anodic double layer charging (~ 0.3 – 0.7 V); and (3) cathodic M-OH_{ads} reduction (~ 0.3 – 0.7 V, negative sweep).

In the proton adsorption/desorption region, the M-H binding energy is reduced on the nanotube surfaces with respect to monometallic Pt or Pd;

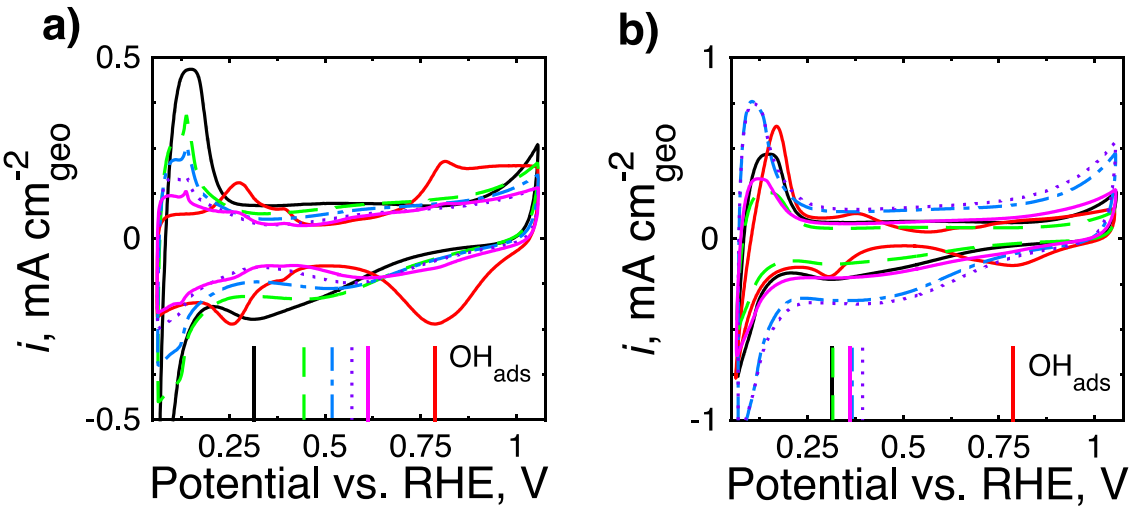

Figure 5.9. Electrochemical data collected in static, N_2-saturated, 0.1M KOH at 50 mV/s for the (a) PtRuNTs and (b) PdRuNTs. Charging currents indicate a composition-dependent reduction in the double-layer charging current for the PtRuNTs and a shift of the surface oxide reduction peak for both the PtRuNTs and the PdRuNTs. Key: a) RuNT (black), PtNT (red), $Pt_{0.04}Ru_{0.96}$NT (green), $Pt_{0.07}Ru_{0.93}$NT (blue), $Pt_{0.10}Ru_{0.90}$NT (purple), $Pt_{0.19}Ru_{0.81}$NT (magenta); b) RuNT (black), PdNT (red), $Pd_{0.07}Ru_{0.93}$NT (green), $Pd_{0.15}Ru_{0.85}$NT (blue), $Pd_{0.20}Ru_{0.80}$NT (purple), $Pd_{0.23}Ru_{0.77}$NT (magenta).

however, the characteristic polycrystalline (110) peak is not well resolved for the bi-metallic nanotubes. This behavior is common for Pt and Pd alloys with Ru and represents a significant challenge in determining changes in M-H binding energy electrochemically. For now, we are left with only a general conclusion that M-H binding energy is reduced. We will show later how changes in oxophilicity can be used as an effective probe for changes in surface electronics and, by analogy, M-H binding energy.

In the double-layer charging region, the charge decreases as the Pt content increases suggesting increasingly complete Pt coverage. The double-layer charging region of the PdRuNTs, however, is more difficult to interpret because of larger variations in grain size (and thus double layer charging).

The Ru-OH_{ads} reduction peak, ca. 0.331 V vs. RHE on the monometallic RuNTs, shifts systematically to higher potentials as indicated by the rightward shift of the bars with increasing adatom composition in Figure 5.9(a,b). There is a large and systematic variation in the reduction potential of these surface oxides on the PtRuNTs. The variation for the PdRuNTs, while not as large, is also systematic with increasing Pd content. Electron transfer from subsurface Ru to the Pt or Pd overlayers would increase the affinity of the Pt or Pd surface skins with adsorbed OH, making reduction of surface oxides more difficult vs. the monometallic analogs, as is seen here.

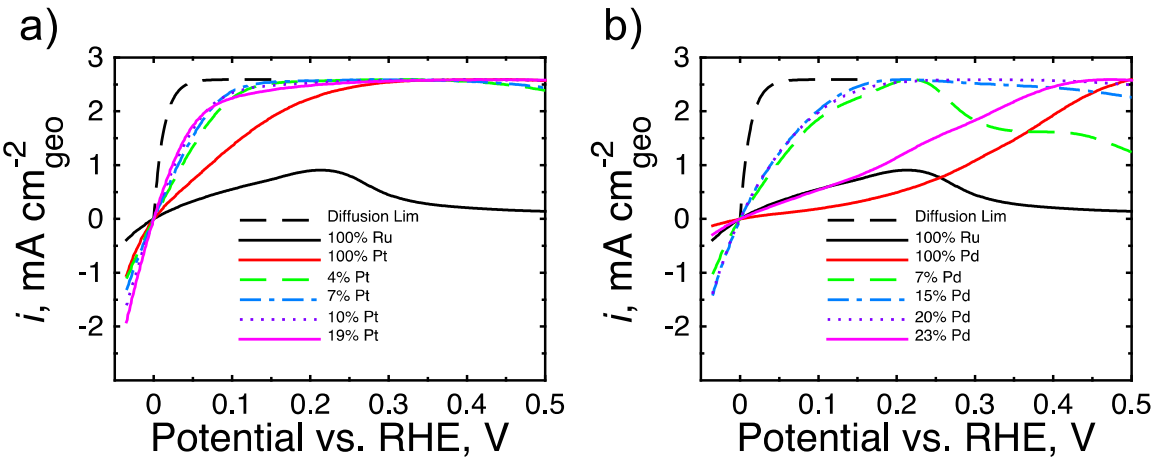

Figure 5.10. Positive-going scans in H_2-saturated, 0.1M KOH at 1600 rpm and at 10 mV/s (c-d) for the (a) PtRuNTs and (b) PdRuNTs. HOR performance of PtRuNTs and PdRuNTs are enhanced in comparison to pure Pt, Pd, or Ru nanotubes and approach the mass-transport-limited current.

From the collective structural and electrochemical data presented thus far, one would expect that hydrogen oxidation would be enhanced because of the ligand and strain effects for the Pt or Pd overlayers on the RuNTs. Hydrogen oxidation activity was measured under rotation at 1600 RPM and 10 mV/s; these data are given in Figure 5.10. The resulting performance of the bi-metallic catalysts was compared to the mass transport limited current (black dashed line, Figure 5.10) calculated using Eq. 5.1:

$$\eta_{diffusion} = \frac{RT}{2F} \ln\left(1 - \frac{i}{i_{lim}}\right) \qquad (5.1)$$

The HOR activity data for the pure Ru, Pt, and Pd nanotube catalysts are similar to those reported in the literature for monometallic polycrystalline surfaces[219] indicating that the annealed nanotubes made using our vapor-impregnation technique perform in a manner consistent with a clean, active, extended polycrystalline surface. Additionally, the illustrated data show exceptional enhancement of the HOR activity for the Ru-nanotube analogues to extended polycrystalline surfaces with fractional overlayers of Pt or Pd.

The specific activities of the bi-metallic structures are all significantly increased vs. the monometallic counterparts. The surface-area-normalized activities are given in Figure 5.11 and are considered with respect to the fractional overlayer coverage of Pt or Pd on Ru, which was calculated using a simple geometric model for the nanotubes and corroborated by the double-layer charging behavior. The results are used to illustrate a strong variation in activity with overlayer coverage with a maximum at ~ 0.5 – 0.8. By optimizing the structure of the nanotubes, we have synthesized the most active alkaline HOR catalyst reported to date with a specific activity of 2.4 mA/cm^2_{metal} at 50 mV vs. RHE. This result is nearly 5x our recently reported activity on carbon-supported Pt nanoparticles (0.51 mA/cm^2_{Pt}) with dramatically increased Pt utilization efficiency: 1,240 A/g_{Pt} for the optimized nanotube vs. 280 A/g_{Pt} for carbon-supported Pt nanoparticles.[54] The similar ~2.5x increase for the PtRuNTs and PdRuNTs with respect to the monometallic counterparts suggests similar

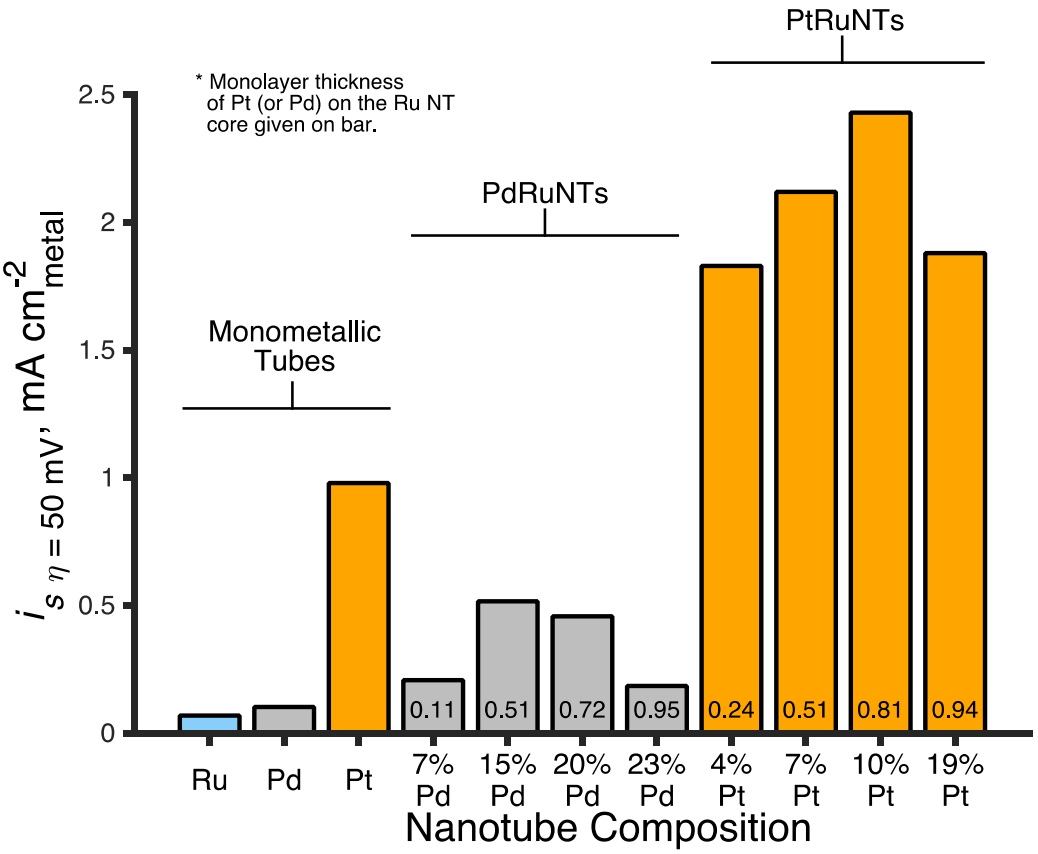

Figure 5.11. HOR specific activity of the various experimental nanotube samples. The Pt (or Pd) monolayer thickness is given on the bars for the bi-metallic nanotubes. There are significant improvements in specific activity vs. the constituent monometallic nanotubes, and the optimum performance is achieved at ~0.5-0.8 overlayer coverage for the PdRuNTs and the PtRuNTs.

reductions in M-H binding energy (as described by a Brønsted–Evans–Polanyi relationship if H-binding energy is proportional to the difference in the activation energy[191]).

There are meaningful conclusions that can be drawn from changes in Tafel slope with respect to overlayer coverage. The Tafel slope describes how the current changes with respect to the applied potential and is characteristic of the interfacial reaction kinetics.[220] Consequently, it can be used to determine the rate-determining step by comparing it to the results from microkinetic models for a hypothesized HOR mechanism.[192]

Tafel plots were obtained after correcting the HOR branch of the activity data by subtracting the diffusion overpotential and determining the kinetically-limited HOR currents.[11] The reaction order was determined previously for Ru_xPt_y and Ru_xPd_y alloy nanoparticles using Eq. 5.2.

$$i = i_k \left[1 - \frac{i}{i_{lim}}\right]^m \qquad (5.2)$$

The reaction order, *m*, is thus the slope from plots of log(*i*) vs. the log(1 – i/i_{lim}). We previously found reaction orders of ~0.5 for HOR in alkaline media on supported alloy nanoparticle catalysts.[54]

Both the HOR and HER branches of the corrected kinetic currents collected at 1600 rpm and illustrated in Figure 5.10, were fit using the Butler-Volmer[220] equation given in Eq. 5.3.

$$i\,[mA/cm^2_{metal}] = i_0 \left[e^{\left(\frac{\alpha_A F}{RT}\eta\right)} - e^{\left(-\frac{\alpha_C F}{RT}\eta\right)}\right] \qquad (5.3)$$

where the sum of the anodic (α_A) and cathodic (α_C) transfer coefficients is equal to one for a single-electron reaction at a given overpotential, η. For symmetric reactions, the anodic and cathodic transfer coefficients are both ~0.5. Transfer coefficients can change throughout polarization;[220] therefore, conclusions drawn here with respect to reaction symmetry are limited to the regions where the kinetic currents are fit as illustrated in Figure 5.12. The Tafel slopes, as well as other electrochemical data, are reported for the nanotube catalysts in Table 5.3.

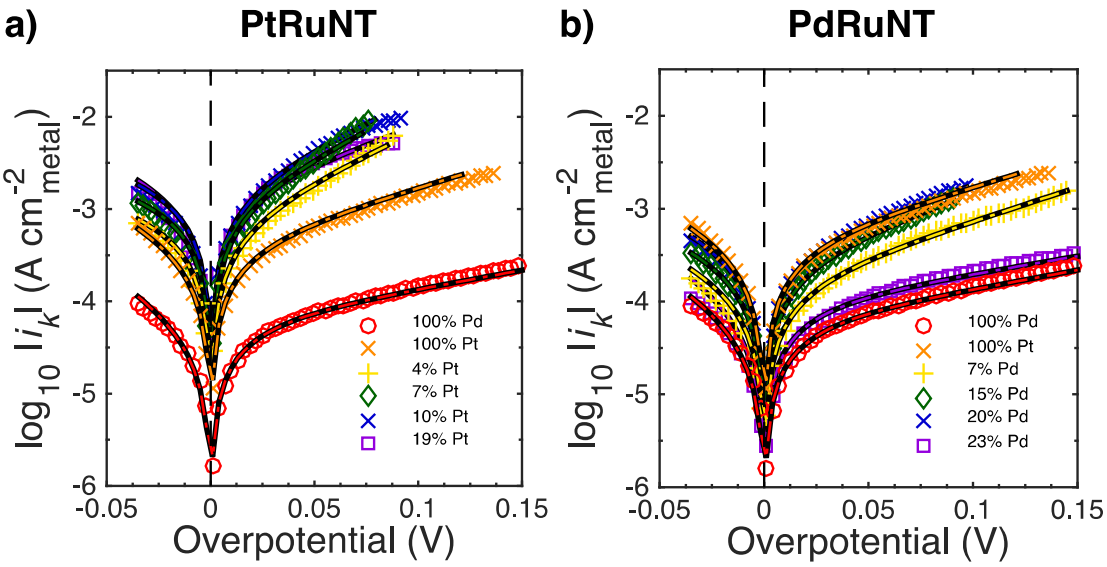

Figure 5.12. Tafel slope analysis for HOR/HER in H_2-saturated, 0.1M KOH obtained at 10 mV/s and 1600 rpm for (a) PtRuNTs and (b) PdRuNTs. Butler-Volmer equation fits (solid) to the kinetic currents (symbols) are illustrated for the samples indicated in the legends.

Table 5.3. Performance characteristics for HOR electrochemical analyses. Parameters based off of kinetic currents were not able to be determined for the Ru nanotube because it did not reach the mass transport limited current density

Catalyst	ECSA	Loading	Exch. Curr, i_0	$i_{\eta = 50\ mV}$	$i_{\eta = 50\ mV}$	$i_{\eta = 50\ mV}$	Tafel	Transfer Coefficient	
	(m^2/g)	($\mu g/cm^2_{disk}$)	(mA/cm^2)	(mA/cm^2)	(A/g_{PGM})	($A/g_{Pt/Pd}$)	(mV/dec)	α_A	α_C
Pt	11.1	7.16	0.363	0.98	109	109	145	0.4	0.6
Ru	19.3	7.04	n/a	0.069	13.9	n/a	n/a	n/a	n/a
Pd	13.7	7.03	0.054	0.103	14.1	14.1	242	0.24	0.76
$Ru_{0.96}Pt_{0.04}$	10.5	7.01	0.629	1.83	192	2,580	86.3	0.67	0.33
$Ru_{0.93}Pt_{0.07}$	10.5	6.92	1.04	2.12	223	1,580	92.2	0.63	0.37
$Ru_{0.90}Pt_{0.10}$	10	6.98	1.461	2.43	243	1,240	94.2	0.62	0.38
$Ru_{0.81}Pt_{0.19}$	13.7	6.92	1.329	1.88	257	825	124	0.47	0.53
$Ru_{0.93}Pd_{0.07}$	6.7	7.14	0.138	0.208	148	2,020	135	0.43	0.57
$Ru_{0.85}Pd_{0.15}$	36.1	6.53	0.224	0.517	187	1,190	119	0.49	0.51
$Ru_{0.80}Pd_{0.20}$	29.7	6.17	0.319	0.458	136	653	129	0.45	0.55
$Ru_{0.77}Pd_{0.23}$	20.4	7.6	0.083	0.185	37.7	158	258	0.23	0.77

A Tafel slope of ~30 mV/dec is suggestive of a molecular hydrogen dissociative adsorption rds (Tafel) and a slope of ~120 mV/dec would indicate an electron transfer rds (Volmer/Heyrovsky).[192] Slopes of ~240 mV/dec are also consistent with an electron transfer rds for asymmetric reactions. If more than one rds is present, the Tafel slope is an active-site-weighted average of the collected rate-determining steps at different active sites, i.e., it will lie intermediate to the respective Tafel slopes for the various rate-determining steps.

On the PtRuNTs, the Tafel slope is intermediate to the values expected for a purely hydrogen dissociative rds (~30 mV/dec) and for a purely symmetric electron transfer rds (~120 mV/dec). The Tafel slopes increase towards 120 mV/dec with increasing Pt overlayer coverage. The results here suggest that both ligand effects and bi-functional active sites are present on the PtRuNTs, as conceptualized in Figure 5.13. Such observations are consistent with the geometric arrangement of active sites of fractional overlayers on extended polycrystalline surfaces where most of the Pt atoms are not directly adjacent to the more oxophilic Ru atoms. Pt atoms adjacent to the more oxophilic Ru atoms are theorized to depend upon a bi-functional mechanism for HOR in alkaline conditions[190] while Pt-Pt active sites would exhibit ligand and strain effects from the presence of sub-surface Ru[86]. The intermediate Tafel slope, therefore, represents an active-site-weighted average Tafel slope for the PtRuNTs.

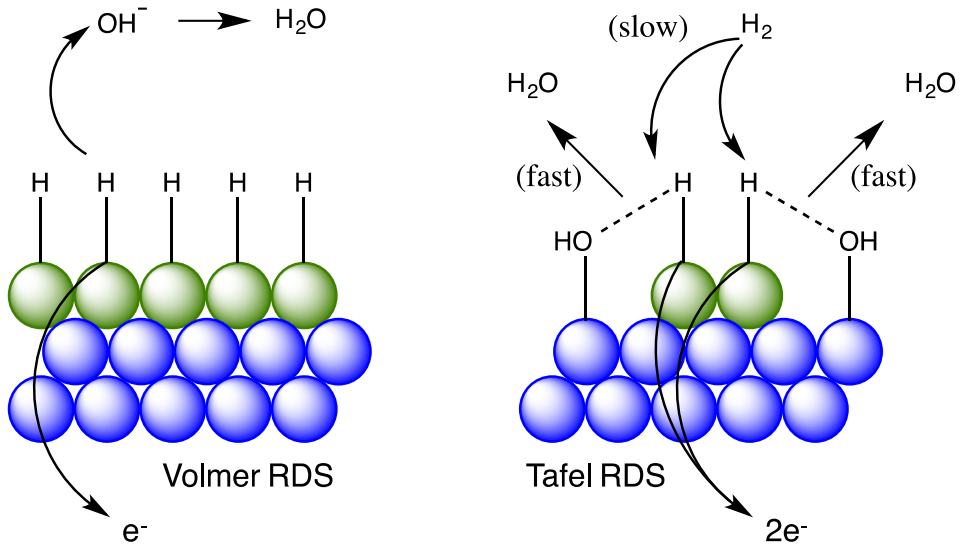

Figure 5.13. Schematic of Pt atoms (green) on Ru atoms (blue) comprising a PtRuNT showing active sites composed only of Pt atoms (left), as well as active sites of both Pt and Ru atoms (right). Electronic effects from the subsurface Ru reduce H-binding energy on both surfaces. On Pt atoms with adjacent OH, the electron transfer step is faster and the bi-functional active site clears the Pt atoms for slower H_2 dissociative adsorption (Tafel rds).

Tafel data collected on Pt-covered, Ru nanotubes starkly contrast with that collected on Ru_xPt_y homogeneous alloy nanoparticles where we observed considerably reduced Tafel slopes of ~30 mV/dec.[54] The nanoparticle alloys exhibited a high degree of dispersion as evidenced by homogeneous alloy formation with minimal atomic segregation of Ru and Pt or Pd. Presumably, this random mixing persisted throughout the nanoparticle from core to surface, whereas a high degree of segregation is predicted thermodynamically and observed experimentally in the bi-metallic nanotube structures synthesized and detailed here.

We hypothesize that ligand effects have reduced the M-H binding energy sufficiently on the PtRuNTs so that bi-functional effects are observable. This is in direct contrast to the PdRuNTs where ligand effects have not reduced the M-H binding energy sufficiently to observe bi-functional effects. This behavior would depend upon a similar intermediate species in both hydrogen dissociative adsorption and electron transfer rate-determining steps, namely H_{ad}, as given in Eq. (5.4), (5.5), and (5.6).

Tafel Reaction:

$$H_2 \leftrightarrows 2H_{ad} \qquad (5.4)$$

Heyrovsky Reaction:

$$H_2 + OH^- \leftrightarrows H_{ad} + e^- + H_2O \qquad (5.5)$$

Volmer Reaction:

$$H_{ad} + OH^- \leftrightarrows e^- + H_2O \qquad (5.6)$$

The data here exhibit no explicit differences in the H_{ad} described in the different HOR intermediate reactions. Instead, we see a smooth transition between PtRuNT structure, exchange current densities, and corresponding Tafel slopes. We, therefore, interpret our results with respect to one type of adsorbed hydrogen intermediate whose interaction energy with the PtRuNTs has been sufficiently reduced to see both electron transfer and bi-functional effects during HOR. Such an interpretation is consistent with recent microkinetic modeling of the HOR/HER equilibrium where invoking different species of adsorbed hydrogen was not necessary to estimate the intrinsic activity of Pt.[221] Additionally, the different microkinetic steps do not discriminate here between solution OH^- and surface-adsorbed OH_{ads}.[221]

All of the Pd-containing electrocatalysts, with the exception of the monometallic Pd and $Ru_{0.77}Pd_{0.23}$ nanotube samples, exhibited a Tafel slope of ~130 mV/dec in accord with a Heyrovsky/Volmer rate-determining step. The $Pd_{0.23}Ru_{0.77}$NT sample exhibited a Tafel slope of ~258 mV/dec similar to that observed on monometallic Pd nanotubes and in accord with literature reports of HOR on polycrystalline Pd in alkaline electrolyte[219] when properly corrected for the HOR reaction order on Pd. Throughout the compositional spectrum, the HOR mechanism does not change on PdRuNTs. This behavior has been observed on Ru_xPd_y alloy nanoparticles that we have presented previously.[54]

For equivalent atomic compositions between the PtRuNTs and the PdRuNTs, Pd forms more complete overlayers than Pt because of its lower density. As the layer thickness increases, the outermost Pd regains its lattice flexibility that is restricted by the Ru for the thinner overlayers. Therefore, we expect that the overlayer is sufficiently thick on the $Ru_{0.77}Pd_{0.23}$ sample that it begins to suffer some of the same problems as Pd with respect to the HOR. We have described this phenomenon before for Pd nanoparticles and hypothesized that it is related to hydride formation. The tendency of Pd to form hydride explains both its insensitivity to H_2 concentration during HOR, as well as its very high Tafel slope.

As discussed previously, we observed behavior in the charging currents in Figure 5.9 that would suggest a reduction in the H-binding energy of the bi-metallic nanotubes by a general shift of the H_{UPD} desorption features to more anodic potentials, but this is only qualitative. Changes, however, in the O-binding energy (oxophilicity) should describe the same electronic changes and thus correlate with changes in H-binding energy. We use the ORR half-wave potential, illustrated in Figure 5.14, therefore, in an attempt to quantify changes in surface electronic effects. ORR is a well-studied phenomenon in electrocatalysis research and is an electrochemically accessible measure of surface electronic

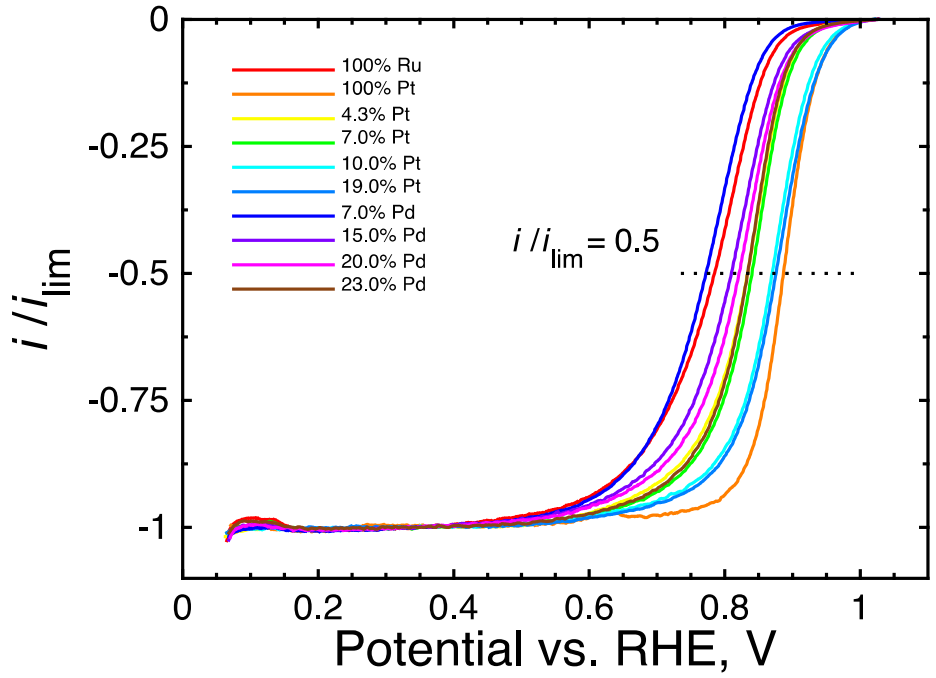

Figure 5.14. Electrochemical oxygen reduction data collected in O_2-saturated electrolyte at 1600 rpm and 10 mV/s. Oxygen reduction currents have been normalized to the transport limited currents and comparisons have been made using the respective half-wave potentials (dotted).

state that is known to correlate with *d*-band spacing in alkaline and acidic electrolyte.[75,86,222–227]

ORR data were collected for the monometallic and bi-metallic nanotubes. The data were normalized to the mass-transport limited currents and the respective half-wave potentials were measured. We plot, in Figure 5.15, the HOR exchange current density, i_0, with respect to the ORR half-wave potential.

The collected results illustrate a volcano-like dependence of i_0 whose activity reaches a maximum at a half-wave potential of approximately +0.86 V vs. RHE. We have interpolated a *d*-band center scale using calculated results provided in the literature[226] and the ORR half-wave potentials of the monometallic Ru and Pt nanotubes. The maximum activity on this interpolated *d*-band center scale is at ca. –2.1 eV relative to the Fermi level. The corresponding interpolated values of the *d*-band centers for the bi-metallic nanotubes correspond closely to the calculated values for fractional overlayers on Ru. For the PdRuNTs: –1.59 (calculated) vs. –1.55 (experimental mean). For the PtRuNTs: –2.11 (calculated) vs. –2.00 (experimental mean). The volcano correlation of the *d*-band center with exchange current density suggests a strong role for the electronic structure in determining HOR activity.

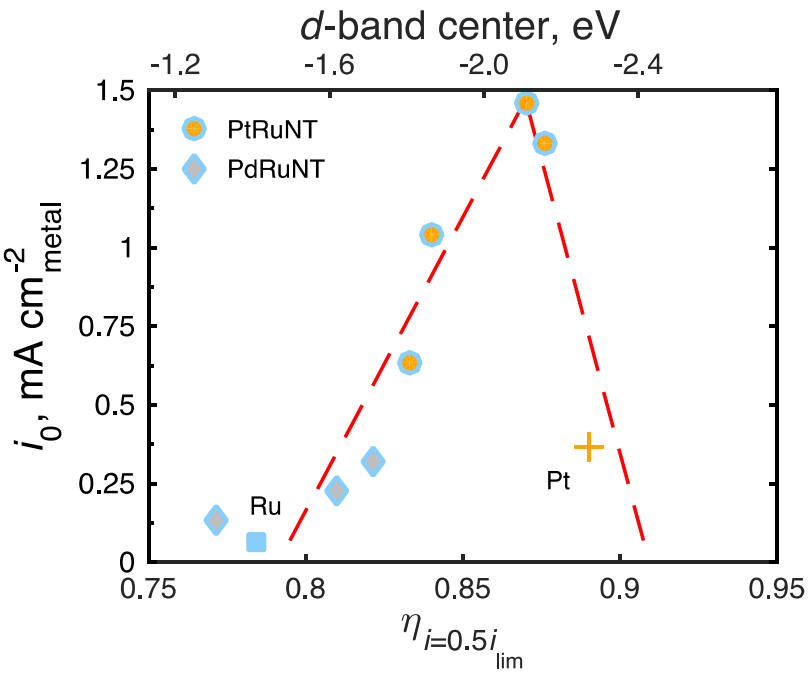

Figure 5.15. HOR exchange current density with respect to the half-wave potential for ORR in O_2-saturated, 0.1M KOH for the RuNT (square), PdRuNTs (diamond), PtRuNTs(circle), and the PtNT (plus). Dashed guides are for the eye only. The *d*-band center scale was determined using calculated values for the monometallic RuNTs and PtNTs.[226] Interpolated *d*-band centers are similar to calculated values for fractional overlayers of Pt or Pd on Ru (see text). Pd samples that formed Pd-H during HOR (as determined by the ~0.25 anodic transfer coefficient) exhibited an unusually low activity because of hydride formation[54] and have been left off of the chart for clarity.

Conclusion

Ru nanotubes were used as analogs to extended polycrystalline surfaces to support Pt- and Pd-overlayers. The HOR activity of these bi-metallic nanotubes varies with the thickness of the Pt or Pd overlayer to yield electrocatalysts with optimal bi-functional, strain and ligand effects. Using ORR half-wave potential as an electrochemical proxy for *d*-band spacing, we find a maximum activity for calculated shifts around –2.1 eV versus the Fermi level. On optimally constructed tubes with fractional surface coverage of Pt on Ru nanotubes, we observe a mixed active-site population alternatively governed by hydrogen dissociative adsorption or electron transfer, yielding Tafel slopes intermediate between 30 and 120 mV/dec. Therefore, both theoretical rate determining steps proposed in the literature may be observed in accord with the nanoscale proximity of active sites. The vapor-grown, bi-metallic nanotubes used here have successfully translated the gains typically seen for epitaxially grown films on extended surfaces to realizable, nanoscale electrocatalysts.

CHAPTER 6

COMPUTATIONAL FRAMEWORK FOR CALCULATING HAMAKER COEFFICIENTS AND INTERACTION ENERGIES FOR FUEL CELL ELECTRODE MATERIALS

Abstract

Despite our interest in designing active extended surface electrocatalysts in an effort to overcome the shortcomings of the supported catalyst paradigm, supported catalysts are currently more practical for application in a fuel cell electrode. The durability issues observed for these catalyst nanoparticles arises from a weak adsorption to the carbon support, and evidence of a strong interaction between the two components has not been reported. Accurately modeling the interactions of these materials could be highly useful for improving catalyst dispersion and for predicting the propensity of the nanoparticles to agglomerate during fuel cell operation. Additionally, such a tool could be used to model the interactions of extended surfaces for building electrodes with these materials. A computational framework has been developed to allow for the calculation of Hamaker coefficients and interaction energies that may be used to model the interactions between nanostructured fuel cell materials.

Introduction

In a carbon-supported catalyst, weakly adsorbed metallic nanoparticles can agglomerate when the energy for the cohesion of the catalyst nanoparticles exceeds the energy for the adhesion of the catalyst nanoparticle to the support material.[228] Two objects in close proximity can be acted upon by a number of forces including double layer, structural, steric, depletion, hydration, and

hydrophobic forces; additionally these objects can be acted upon by van der Waals forces.[228] A Hamaker coefficient is a material property that is a function of the electronic properties of two interacting materials and the medium that separates the two objects. The Hamaker coefficient is considered a convenient way to approximate the strength of the van der Waals forces acting between two objects, and it is a function of the material electromagnetic properties, temperature and separation between the two objects. By measuring or calculating changes in the dielectric responses with frequency of the materials and medium, one can predict the van der Waals forces from these Hamaker coefficients.[228]

Experimental Measurements of Optical Properties for Calculating Hamaker Coefficients

The input optical properties of the various fuel cell electrode materials of interest are obtained by measuring material optical properties experimentally. Dilute suspensions of the catalyst and support materials, measured separately, in water (0.01 – 0.30 wt%) are required so that shielded, interparticle interactions may be neglected.[228] If the analyte was provided in powdered form, suspensions were prepared by adding the powder to DI water and sonicating for 15 minutes prior to measurements to disperse the material. The concentration of nanotubes in a water-based suspension is determined with a nanobalance and diluted with DI water to the appropriate concentration.

UV-Visible spectroscopy allows simple measurement of optical properties of the materials at relatively high energies considering the mathematical transforms for computing the Hamaker coefficients. To measure this data we used a Cary 50 UV-Visible dual-beam spectrophotometer, which splits the incident beam to simultaneously measure the sample and background responses to radiation, from the ultraviolet to visible light regions. Sample solutions and DI water were isolated in matched quartz cuvettes with pathlengths of 1 cm.

To obtain optical data in the low energy regions, we observed each solution to wavelengths as deep as the near-IR with a Bruker Vertex 70 FTIR spectrometer. To avoid infrared absorbance by atmospheric water vapor and CO_2, the sample compartment was purged for 10 min with dry N_2 prior to measurement. During measurement, solutions were contained in a liquid cell with adjustable pathlength between IR-transparent CaF_2 windows. These CaF_2 windows are transparent into the near IR to wavenumbers as low as 896 cm^{-1}. Since the refractive index of calcium fluoride is comparable to water, fringing interference in spectral data that may be encountered when using other window materials, like ZnSe, may be avoided.

Low concentrations of catalyst or support and the presence of liquid water in the solutions presented problems in the IR as strong absorbance peaks for water dominate the spectra at 3100-3700 cm^{-1}, 1600-1700 cm^{-1}, and around 700 cm^{-1}. The background spectra for water may be measured separately and

subtracted to obtain the FTIR spectra for the isolated material. Material spectra collected in water after background subtractions were compared to spectra measured after drop casting and drying the catalyst or support solution onto an IR-transparent window of ZnSe. Observing these dried samples provided confirmation that the materials were inactive in the wavenumber ranges where water bands were present. Data from the water-suspended materials were analyzed to more accurately approximate sample thickness (cuvette pathlength) and concentration.

Computational Methods

The Hamaker coefficient formalism can be used after obtaining the dielectric spectra for the various materials of interest. One of the ways that this has been done previously is by an ab initio orthogonalized linear combination of atomic orbitals (OLCAO) density functional theory technique.[229] However, an alternative to this method is to experimentally measure the optical properties of the materials using spectroscopic methods (UV-Vis and FTIR) and to transform this data to obtain the dielectric spectra.[230] Despite spectroscopic range limitations, this experimental approach still results in accurate values for Hamaker coefficients of materials used as standards for van der Waals interactions.[231] By collecting the UV-Vis and IR spectra for a material in a solution of known concentration, we can calculate the absorption coefficient, k, for the material from the Beer-Lambert relationship (Eq. 6.1).

$$k = \frac{\lambda}{4\pi \mathrm{l c}} ln\left(\frac{I_1}{I_0}\right) \qquad (6.1)$$

Here, λ is the wavelength of incident radiation, l is the cuvette pathlength, c is the sample concentration, and I_1 and I_0 are the measured and incident intensity of the absorption spectra, respectively.

The absorption coefficient obtained above is the imaginary part of the refractive index variable, and the real part of the refractive index variable, n, can be estimated by applying a Kramers-Kronig transformation (Eq. 6.2) over the complete range of spectral data measured.[232] For this to be done, a cubic spline must be fit to fill in the region of missing data between the IR and UV-Vis that is not measured by either spectrometer. The function for the transformation is given in Equation 6.2.

$$n = 1 + \frac{1}{\pi} P \int_{-\infty}^{\infty} \frac{k(\omega')}{\omega' - \omega} d\omega' \qquad (6.2)$$

The integral is conducted over the entire finite range of frequency measured for the material spectra. The absorption coefficient is an imaginary function of the imaginary frequency, represented by ω', where the real frequency is denoted by ω. The coefficient P indicates that the integral is improper; we have developed a script to integrate the function. Once the real part of the refractive index is estimated it must be simply transformed to the imaginary part of the dielectric function with Eq. 6.3.

$$\varepsilon'' = 2nk \qquad (6.3)$$

Having obtained the imaginary part of the dielectric function in Eq. 6.3, we can apply a Kramers-Kronig transformation to estimate the dielectric function along the imaginary axis using Equation 6.4.[232]

$$\varepsilon(i\xi) = 1 + \frac{2}{\pi} P \int_{-\infty}^{\infty} \frac{\omega \varepsilon''(\omega)}{\omega^2 + \xi^2} d\omega \qquad (6.4)$$

This transformation returns a smoothly decaying function of the imaginary frequency. A material's dielectric spectrum usually appears relatively featureless, but it contains all of the information about the material's electronic band structure properties[233] necessary for computing valuable information about its van der Waals interactions with other materials.

The data for ε(iξ), the dielectric function, is fit to a series of harmonic oscillators with a least-squares fitting routine developed in Igor Pro. The complete dielectric spectrum of a material for frequency from zero to infinity is required to compute a Hamaker coefficient. By fitting for the data of a smoothly decreasing function, we can compensate for our limited spectral range and accurately extrapolate data at high imaginary frequencies.[231] Fitting for the data allows us to sample for the function at discrete Matsubara frequencies, temperature-dependent "imaginary frequencies", which cause the function to decay exponentially when these frequencies are the independent variable. The fitting function for a series of harmonic oscillators is given in Equation 6.5.

$$\varepsilon(i\xi) = 1 + \sum_{j=1..3} \frac{f_j}{\omega_j^2 + \xi g_j + \xi^2} \qquad (6.5)$$

The value of the dielectric spectra at the zero-frequency must be approximated to complete the data set for computation. This is done using a Drude-type approximation (Eqs. 6.6, 6.7, 6.8) of the dielectric spectra as it approaches zero, which is based on the conductivity data for the bulk materials.[234,235]

$$\varepsilon''(i\xi) = 1 + \frac{\omega_p^2}{\omega_\tau^2 - \xi^2} + \sum_{j=1..3} \frac{f_j}{\omega_j^2 + \xi g_j + \xi^2} \qquad (6.6)$$

$$\omega_p = \sqrt{\frac{e^2 n}{m_e^* \varepsilon_0}} \quad (6.7)$$

$$\omega_\tau = \rho \varepsilon_0 \omega_p^2 \quad (6.8)$$

Here, e is the electronic charge, n is the conduction electron density, m_e^* is the effective electron mass, ε_0 is the permittivity of free space, and ρ is the resistivity. Once the value for the dielectric function at zero-frequency has been calculated using Eq. 6.6, an approximation of a complete dielectric spectrum for a material that can be used to estimate the Hamaker coefficients for systems using the Lifshitz relationship is complete. The Hamaker coefficient for two spheres can be calculated from Equation 6.9, below.[231]

$$A_{CmS}(z; R_C, R_S) = -\frac{3}{2} kT \sum_{n=0}^{\infty}{}' r_n \sum_{q=1}^{\infty} \frac{1}{q^2} \times \int_1^{\infty} p[(\bar{\Delta}_{Cm}\bar{\Delta}_{Sm})^q + (\Delta_{Cm}\Delta_{Sm})^q] e^{-r_n p q} dp$$

(6.9)

$$\bar{\Delta}_{ij} = \frac{s_i\varepsilon_j - s_j\varepsilon_i}{s_i\varepsilon_j + s_j\varepsilon_i} \quad (6.10)$$

$$\Delta_{ij} = \frac{s_i - s_j}{s_i + s_j} \qquad (6.11)$$

$$s_i = \sqrt{p^2 - 1 + \frac{\varepsilon_i}{\varepsilon_m}} \quad (6.12)$$

$$r_n = \frac{2l\varepsilon^{1/2}}{c}\xi_n \quad (6.13)$$

$$\xi_n = \frac{2\pi k_B T}{\hbar} \quad (6.14)$$

In Eq. 6.9, A_{CmS} is the Hamaker coefficient and is a function of the separation distance between the centers of the two interacting spheres and of the dielectric properties of the spheres and the medium in the modeled system. The two spheres here are a catalyst nanoparticle (C) with radius R_C and a support (S) with radius R_S, that interact across a medium (m). The inputs for the material properties are ε_i and s_i and the dielectric medium between the materials is represented by ε_m. Typically the dielectric medium of interest is water or a vacuum.

We have developed a series of scripts for the above calculations to approximate the Hamaker coefficients for systems from data sets comprised of discrete Matsubara frequency spacing, obtained by originally measuring the UV-Visible and FTIR spectra experimentally for a number of materials. The data sets for the materials used as inputs for calculating Hamaker coefficients were calculated using the fitting coefficients determined for each material (Eq. 6.5). These fitting coefficients simplify approximating the dielectric spectra starting at frequency equal to zero (from the Drude approximation in Eq. 6.6) and extend to infinite frequency.

In addition to Hamaker coefficients, which provide information about the strength of interaction based on the electron densities of the materials present and the dielectric properties of the intervening media, the geometry-dependent interaction energies for the system can also be computed. The interaction energy for the two spheres discussed above is given in Equation 6.15.

$$G_{CS}(z; R_C, R_S) = -\frac{A_{CmS}}{3}\left[\frac{R_C R_S}{z^2-(R_C+R_S)^2} + \frac{R_C R_S}{z^2-(R_C-R_S)^2} + \frac{1}{2} ln \frac{z^2-(R_C+R_S)^2}{z^2-(R_C-R_S)^2}\right] \quad (6.15)$$

Here, A is the Hamaker coefficient, z is the shortest distance between the surfaces of the spherical particles, and R_C and R_S are the radii of the particles. The use of C designates the catalyst nanoparticle and S designates the catalyst support. This interaction energy of a supported nanoparticle catalyst system provides insight into the approximate distance between the two interacting materials and how favorable or stable this interaction is.

There currently exists formulism for a number of system geometries.[229,231,233] Modeling with spheres simplifies, but adequately describes, the geometry of a catalyst nanoparticle on a support. However, the use of spheres is not acceptable for modeling the colloidal interaction parameters of extended surfaces like metallic nanotubes. In addition to studying supported catalyst colloidal interactions, we are also interested in modeling the van der Waals interactions of catalyst nanotube suspensions. The proper Hamaker coefficient and interaction energy formulas for perpendicular or parallel cylinders

should be substituted in place of those used for spheres above to accurately model these nanotubes.

Equation 6.16 allows calculation of the interaction energy of a sphere with an infinite cylinder,[236] represented in Figure 6.1. Here, *s* refers to the sphere and *c* refers to the cylinder. The variable *z* refers to the separation distance between the centers of the sphere and cylinder, and R is the radius of the respective object. A_{Ham} is calculated using equation 6.9.

$$G_{\frac{s}{c}}(z;R_sR_c) = -\frac{A_{Ham}\pi}{8}\left[\frac{R_s^3-(z+R_c)^2}{2(z+R_c+R_s)^2}+\frac{(z-R_c)^2-R_s^3}{2(z-R_c+R_s)^2}-\frac{(z-R_c)^2-R_s^3}{2(z-R_c-R_s)^2}+\frac{(z+R_c)^2-R_s^3}{2(z+R_c-R_s)^2}+\right.$$

$$\left.\frac{2z+2R_c}{z+R_c+R_s}-\frac{2z+2R_c}{z+R_c-R_s}+\frac{2R_c-2z}{z-R_c+R_s}+\frac{2z-2R_c}{z-R_c-R_s}+ln\left(\frac{z+R_c+R_s}{z+R_c-R_s}\right)+ln\left(\frac{z-R_c-R_s}{z-R_c+R_s}\right)\right] \quad (6.16)$$

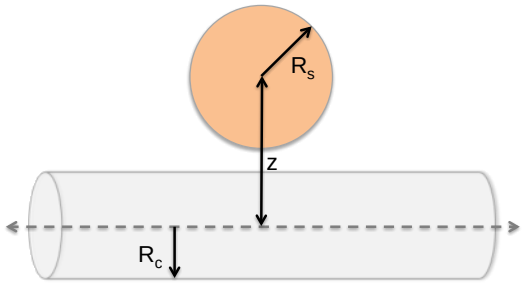

Figure 6.1. Illustration of the geometry described in equation 7.15: an interacting sphere and cylinder.

Equation 6.17 is used to calculate the interaction energy of two parallel cylinders of infinite length at small separations[237], *l*. Here, *1* and *2* distinguish the

two cylinders, allowing for the cylinders to be composed of different materials. R is the radius of the respective cylinder and z is the distance between the longitudinal axes. $A_{1m/2m}$ is the Hamaker coefficient and is calculated with equation 6.18, where $\bar{\Delta}_{ij}$ is calculated with Equation 6.10. The geometry of this system is represented in Figure 6.2.

$$G_{c||c}(l; R_1, R_2) = -\sqrt{\frac{2R_1R_2}{R_1+R_2}}\frac{A_{1m/2m}}{24l^{3/2}} \quad (6.17)$$

$$A_{1m/2m} = \frac{3kT}{2}\sum_{n=0}^{\infty}\bar{\Delta}_{1m}\bar{\Delta}_{2m} \quad (6.18)$$

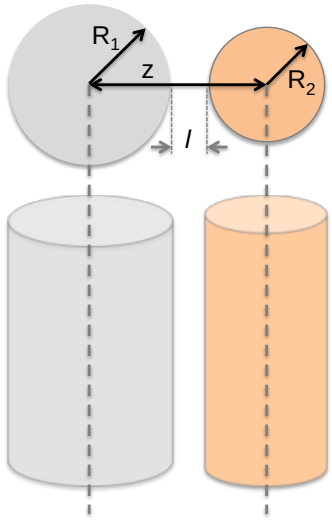

Figure 6.2. Illustration of geometry modeled by Equation 6.16: two infinite, parallel cylinders.

Equation 6.19 is used to calculate the interaction energy of two perpendicular cylinders of the same size[231] separated by a distance of closest contact, *l*. Here, *1* and *2* distinguish the two cylinders, allowing for the cylinders to be composed of different materials. R is the radius of the cylinders and z is the distance between longitudinal axes. $A_{1m/2m}$ is the Hamaker coefficient and is calculated with equation 6.20, where $\bar{\Delta}_{ij}$ and Δ_{ij} are given in Equations 6.10 and 6.11, respectively. The geometry modeled by these equations are represented schematically in Figure 6.3.

$$G_{c\perp c}(l;R) = -\frac{A_{1m/2m}}{6}\frac{R}{l} \qquad (6.19)$$

$$A_{1m/2m}(l) = \frac{3kT}{2}\sum_{n=0}^{\infty}(\bar{\Delta}_{1m}\bar{\Delta}_{2m} + \Delta_{1m}\Delta_{2m}) \qquad (6.20)$$

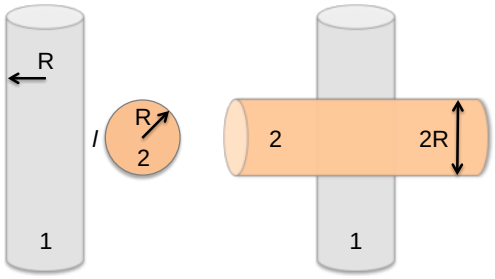

Figure 6.3. Illustration of the interaction system geometry modeled by Equations 6.18 and 6.19: perpendicular cylinders with equal radii.

Results and Discussion

To validate the code for interactions between spheres, Hamaker coefficients were calculated for well-known standards reported in the literature. The dielectric spectra for each standard material, obtained from different sources,[230,238,239] was reported via fitting coefficients for a series of harmonic oscillators, as presented in Equation 6.5. The Hamaker coefficients were calculated from our code using these fitting coefficients and are reported in Table 6.1. Here, Hamaker coefficients are approximated for same-material particle interactions of gold,[230] mica,[238] and water[239] across a vacuum at the limit of low separation.

Table 6.1. Comparison of measured Hamaker coefficients with literature values for common material standards.

Reference Materials	Obsd. Hamaker coefficient (zJ)	Lit. Hamaker coefficient (zJ)
gold-vac-gold	251.6	200-400
mica-vac-mica	74.4	69.6
water-vac-water	43.5	37-40

Figure 6.4 contains Hamaker coefficients and interaction energies as functions of the logarithm of the separation distance between the centers of two spheres. Spherical geometries are an accurate representation of the TKK Pt

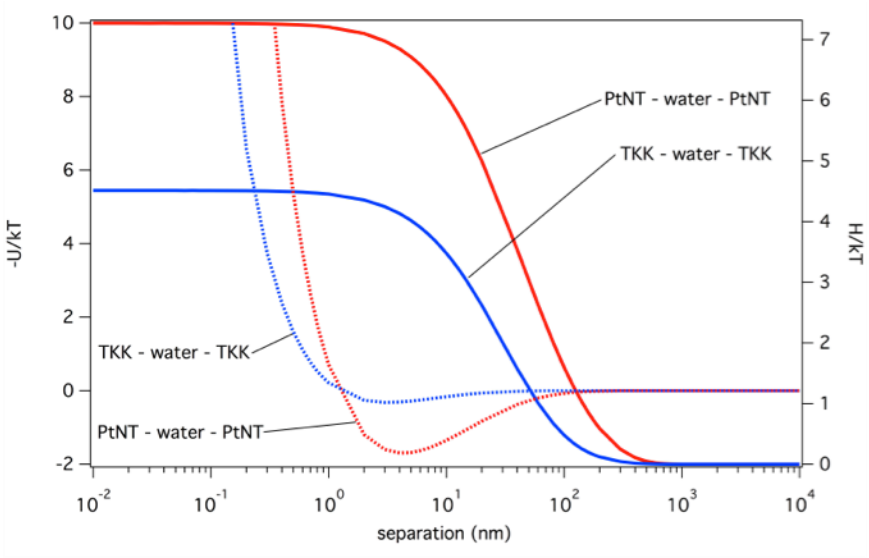

Figure 6.4. Hamaker coefficients (H) and interaction energies (U) as a function of separation distance across water between the centers of two spheres of identical material: TKK Pt black (blue) and PtNTs (red). Thermal energy units are used for the Hamaker coefficient (H, right axis) and interaction energy (U, left axis) for compactness; kT_{room}=1.3807 x 10^{23}(J/K) x 293.15 K = 4.05 zJ, where 1 zJ = 10^{-21} J.

black nanoparticles modeled here, but are not applicable to systems containing nanotubes. Interaction energies are plotted on the left axis with dashed lines, while Hamaker coefficients are reported on the right axis and are plotted with solid lines. Pt (TKK) nanoparticles are modeled as 10 nm radii spheres and PtNTs are modeled with 50 nm radii spheres. The input parameters for calculating the Hamaker coefficients and interaction energies for these materials were obtained from the measured UV-Vis and FTIR spectra. The Hamaker coefficients and interaction energies are normalized by kT in order to more easily compare the magnitude of particle interaction energy to the thermal energy at room temperature. As an example, if the Hamaker coefficient of a system is approximately 1 kT then the binding energy between the components is not strong enough to sustain the interaction.[231]

The interaction between two PtNTs is considerably stronger in water than in a vacuum, while for TKK nanoparticles in water we observe only a modest increase in interaction strength compared to how the materials interact in a vacuum. The PtNTs have a stronger self-interaction in water than do Pt nanoparticles (TKK). The size of the modeled spheres does not influence the Hamaker coefficient, which is only a function of the material properties and separation distance, but the size of the spheres influences the interaction energy. As expected, the PtNT “spheres” that have 10 times the diameter of the Pt nanoparticle (TKK) here have a minimum energy of interaction at a higher

separation value than the TKK nanoparticles. This is a balance of attractive and repulsive forces that indicates a minimum energy for a distance of separation where these two interacting “spheres” would be most stable.

The PtNTs have ~100-125 nm radii, and typical supported catalysts are even smaller than the 10 nm particles modeled here. We expect more exaggerated separation distances for larger modeled nanotubes than those suggested here, where the separation distance of minimum energy between PtNTs modeled appropriately may be greater than the results in Figure 6.4 suggest. Additionally, modeling a hollow nanotube as a sphere is an inadequate representation of the system geometry that has been addressed with updated code for the interaction of cylinders. These results are presented here to provide an example of the kind of information that may be obtained from this model.

Suggested Future Work

This model may be used to study how strongly catalyst nanoparticles adhere to various support materials, whether made from carbon, inorganics or polymers. The strength of interaction is expected to vary with the use of different metals, the use of alloy catalysts and composition of the alloy, and catalyst particle or nanostructure size. Hamaker coefficients may be used to predict the durability of a proposed catalyst during fuel cell operation.

The medium between two interacting materials influences the interaction significantly.[228,239] Where inks are prepared from catalysts either for application to

a glassy carbon electrode for rotating disc experiments or for fuel cell electrode preparation, solvent selection is critical for high dispersion and reproducibility.[97,104,240–242] This model could be used to identify the most appropriate solvent for a particular application, or for a certain set of materials. Identifying a solvent that facilitates a stronger interaction between catalyst and support, or a weaker self-attraction of the catalyst, could improve catalyst dispersion during preparation of the catalyst layer that could ultimately lead to improvements in performance and durability.[242]

Extended surface catalysts are promising materials as electrocatalysts for fuel cells, but applying them to build an electrode for testing in a cell has been a significant challenge in the literature. The use of a template to synthesize nanostructures can be considered advantageous in this respect because it could simplify the application of these high-aspect ratio catalysts within electrodes for fuel cell testing.[99,243,244] Regardless of whether or not the extended surface catalysts of interest are synthesized using templates, modeling colloidal interaction properties of these materials will be critical for electrode fabrication. In addition to Equations 6.16-6.20 above for modeling interactions between spheres and cylinders, formulas for hybrid geometries have also been derived[231] that are applicable to geometries such as cylinders with planes, for example. Models for systems with these geometries would be useful for predicting the interaction strength of metallic nanotubes with carbon materials. The use of carbon here

would not necessarily be as a support; one of the benefits of extended surface catalysts is the potential for deployment of these catalysts without a carbon support that could circumvent issues related to carbon support corrosion.[40,96,245] However, there are cases where electrodes made with extended surface catalysts may benefit from the addition of carbon to the electrode. Adding carbon to the electrode would increase the electrode thickness, and its physical surface area, and could alleviate issues related to liquid water management and flooding that are observed in the ultra-thin electrodes built from NSTFs.[98,100,244] If catalyst inks are made from metallic nanotubes and carbon is added,[108] it will be important to understand how the two components interact. It will be important to study how tuning the solvent mixture used in catalyst ink preparation and varying the carbon material may influence this nanotube-carbon interaction. We suggest that this model could be used to predict catalyst ink formulations that lead to maximum nanotube dispersion. As suggested in Chapter 2, the ability to uniformly disperse platinum nanotubes in a thicker, carbon-containing electrode may allow for the addition of ionomer that is essential for proton conduction in the electrode. Well-dispersed platinum nanotubes in the presence of carbon could reduce the deleterious effects that we observed after ionomer addition to the platinum nanotubes in the absence of carbon in Figure 2.8. In this way, this model could guide the construction of a functional PEMFC cathode catalyst layer from these highly active and durable metallic nanotubes.

CHAPTER 7

CONCLUSION

Unsupported, high-aspect ratio nanostructured catalysts, or extended surface catalysts, continue to be a promising class of electrocatalysts that may overcome the deficiencies of the preferred paradigm of supported nanoparticle catalysts. Promises of improvements in specific activity and durability by these extended surfaces make them candidates for catalyzing a number of reactions. In this work we have synthesized metallic, mixed-phase, and alloyed bimetallic nanotubes by chemical vapor deposition (CVD) and investigate how the tunable material properties influence activity and durability for a number of fuel cell reactions.

We synthesized supportless platinum nanotubes in Chapter 2 and investigated the influence of annealing these nanostructures on oxygen reduction activity. As synthesized, the nanotubes are nanoparticulate aggregates composed of Pt crystallites approximately 3 nm in diameter. Following heat treatment, the nanotubes undergo significant crystallite growth and morphological evolution of the nanotube structure, including the development of nanoscale porosity. Thermally annealing the nanotubes nearly doubled both the mass and specific activities for the ORR compared to the as-synthesized nanotubes, resulting in comparable activity to polycrystalline Pt and five times the activity of commercial carbon-supported Pt nanoparticles. The annealed platinum nanotubes, which demonstrated greater site availability by delaying surface oxide

coverage, were also more durable than the commercial catalyst, retaining more of their electrochemically active surface area after 20,000 cycles.

The success of these platinum nanotubes for ORR and the promise of extended Pt surfaces for oxidizing carbon monoxide at lower potentials than supported nanoparticles motivated the design of methanol oxidation catalysts based on these nanostructures. The CVD technique used to synthesize platinum nanotubes was expanded in Chapter 3 for the synthesis of platinum-ruthenium nanotubes. As-synthesized, the structures are composed of a hydrous Ru oxide nanotube with fine metallic Pt nanoparticles at the nanotube exterior surface. From the high Pt utilization and the use of the hydrous oxide of Ru, shown to effectively promote Pt for methanol oxidation, the as-synthesized platinum-ruthenium nanotubes demonstrated high mass activity for MOR. Alternatively, we annealed the platinum-ruthenium nanotubes to drive alloy formation, grain growth, and nanostructural evolution similar to that observed in the platinum nanotubes designed for ORR. The alloyed platinum-ruthenium nanotubes had improved CO stripping kinetics, and as a result, high specific activity for MOR that we attribute to a more intimate dispersion of Pt and Ru from alloy formation.

We synthesized palladium nanotubes and investigated the influence of heat treatment temperature on activity for formic acid electrooxidation in Chapter 4. Annealed palladium nanotubes were 2.4 times more active than commercial carbon-supported palladium, with the most active nanotubes annealed at 500°C.

However, the annealed palladium nanotubes destabilized rapidly from the formation of poisoning species during the oxidation of formic acid. We underpotentially deposited bismuth on the nanotube surfaces and observed improvements in performance over 4 times that of Pd/C and nearly twice the activity of unmodified palladium nanotubes. A surface Bi coverage of 80% resulted in optimal site-specific activity by drastically reducing surface-poisoning CO generation during formic acid electrooxidation. We found the Bi-modified palladium nanotubes to be exceptionally stable, maintaining twice the area-normalized current density as Pd/C after 24 hours at 0.2 V vs. RHE. We related the enhanced activity and stability of the nanotube catalysts to the presence of highly coordinated surfaces, mimicking a flat polycrystal while retaining high surface area geometry. High Bi coverage on the palladium nanotubes effectively reduced the overpotential for formic acid oxidation, which we suggested to result from a third body effect that promoted the direct, CO-free pathway for formic acid oxidation.

In Chapter 5 we designed unsupported metallic Ru nanotubes with Pt or Pd overlayers by sequential vapor depositions of the metals followed by thermal annealing. By controlling the elemental composition and thickness of these Pt or Pd overlayers, we synthesized nanostructures with very high alkaline hydrogen oxidation activity. Nanotubes with a nominal atomic composition of $Pt_{0.10}Ru_{0.90}$ displayed a specific activity 35 times greater than that of pure Ru nanotubes at a

50 mV overpotential, and nearly 5 times greater than that of carbon-supported Pt nanoparticles. The HOR activity of these bi-metallic nanotubes varied with the thickness of the Pt or Pd overlayer to yield electrocatalysts with optimal bi-functional, strain and ligand effects. Using ORR half-wave potential as an electrochemical proxy for *d*-band spacing, we found a maximum activity for calculated shifts around –2.1 eV versus the Fermi level and suggest that this relationship may be used to rationally design active HOR catalysts with other metals. The surface-segregated, non-alloyed structure of the platinum-on-ruthenium nanotubes also conferred dramatically increased Pt utilization efficiency. We found a platinum-mass normalized activity of 1,240 A/g_{Pt} for the optimized nanotube versus 280 A/g_{Pt} for carbon-supported Pt nanoparticles. We attributed these enhancements to the atomic-scale structural similarity of the nanotube form factor with adlayer-modified polycrystals. These optimally constructed nanostructures with fractional surface coverage of Pt on Ru nanotubes, allowed us to observe a mixed active-site population alternatively governed by hydrogen dissociative adsorption or electron transfer depending on changes in the measured Tafel slopes. Therefore, both theoretical rate determining steps proposed in the literature may be observed in accord with the nanoscale proximity of active sites. These vapor-grown, bi-metallic nanotubes successfully translated the gains typically seen for epitaxially grown films on extended surfaces to realizable, nanoscale electrocatalysts.

In Chapter 6 we discuss a computational framework that has been developed to allow for the calculation of Hamaker coefficients and interaction energies, useful for modeling the interactions between nanostructured fuel cell materials. Though this work has focused on designing active extended surface electrocatalysts in an effort to overcome the shortcomings of supported catalysts, the latter are currently more practical for application in a fuel cell electrode despite weak interactions between the catalyst nanoparticle and the support. This model, which approximates Hamaker coefficients and separation distance dependent interaction energies, may be highly useful for improving catalyst dispersion during ink and electrode preparation and for predicting the propensity of the nanoparticles to agglomerate or ripen during fuel cell operation. Throughout this work we have demonstrated that extended surface catalysts are promising materials as electrocatalysts for fuel cells, but applying them to build an electrode a fuel cell has been a significant challenge in the literature. We suggest that this model will be useful for predicting the interactions of extended surfaces in various solvents that may guide the installation of these structures in fuel cell electrodes.

REFERENCES

(1) Larminie, J.; Dicks, A. *Fuel Cell Systems Explained*; 2nd ed.; John Wiley & Sons, Ltd, 2003; Vol. 93.

(2) Wasmus, S.; Küver, A. *J. Electroanal. Chem.* **1999**, *461*, 14.

(3) Lemons, R. A. *J. Power Sources* **1990**, *29*, 251.

(4) Vigier, F.; Rousseau, S.; Coutanceau, C.; Leger, J.-M.; Lamy, C. *Top. Catal.* **2006**, *40*, 111.

(5) Springer, T. E.; Zawodzinski, T. A.; Gottesfeld, S. *J. Electrochem. Soc.* **1991**, *138*, 2334.

(6) He, C.; Desai, S.; Brown, G.; Bollepalli, S. *Electrochem. Soc. Interface* **2005**, *Fall*, 41.

(7) Neyerlin, K. C.; Gu, W.; Jorne, J.; Gasteiger, H. A. *J. Electrochem. Soc.* **2007**, *154*, B631.

(8) Chalk, S. G.; Miller, J. F. *J. Power Sources* **2006**, *159*, 73.

(9) Rice, C.; Ha, S.; Masel, R. I.; Waszczuk, P.; Wieckowski, A.; Barnard, T. *J. Power Sources* **2002**, *111*, 83.

(10) Varcoe, J. R.; Atanassov, P.; Dekel, D. R.; Herring, A. M.; Hickner, M. A.; Kohl, P. A.; Kucernak, A. R.; Mustain, W. E.; Nijmeijer, K.; Scott, K.; Xu, T.; Zhuang, L. *Energy Environ. Sci.* **2014**, *7*, 3135.

(11) Rheinländer, P. J.; Herranz, J.; Durst, J.; Gasteiger, H. A. *J. Electrochem. Soc.* **2014**, *161*, F1448.

(12) Markovic, N. M.; Schmidt, T.; Stamenkovic, V. R.; Ross, P. N. Oxygen Reduction Reaction on Pt and Pt Bimetallic Surfaces: A Selective Review, 2001, 105–116.

(13) Aricò, A. S.; Srinivasan, S.; Antonucci, V. *Fuel Cells* **2001**, *1*, 133.

(14) Xia, Y.; Yang, P.; Sun, Y.; Wu, Y.; Mayers, B.; Gates, B.; Yin, Y.; Kim, F.; Yan, H. *Adv. Mater.* **2003**, *15*, 353.

(15) Subhramannia, M.; Pillai, V. K. *J. Mater. Chem.* **2008**, *18*, 5858.

(16) Cademartiri, L.; Ozin, G. A. *Adv. Mater.* **2009**, *21*, 1013.

(17) Zhao, X.; Sánchez, B. M.; Dobson, P. J.; Grant, P. S. *Nanoscale* **2011**, *3*, 839.

(18) Bruce, P. G.; Scrosati, B.; Tarascon, J.-M. *Angew. Chem. Int. Ed. Engl.* **2008**, *47*, 2930.

(19) Boukai, A. I.; Bunimovich, Y.; Tahir-Kheli, J.; Yu, J.-K.; Goddard, W. A.; Heath, J. R. *Nature* **2008**.

(20) Dresselhaus, M. S.; Chen, G.; Tang, M. Y.; Yang, R.; Lee, H.; Wang, D.; Ren, Z.; Fleurial, J. P.; Gogna, P. *Adv. Mater.* **2007**.

(21) Sun, S.; Jaouen, F.; Dodelet, J.-P. *Adv. Mater.* **2008**, *20*, 3900.

(22) Koenigsmann, C.; Sutter, E.; Adzic, R. R.; Wong, S. S. *J. Phys. Chem. C* **2012**, *116*, 15297.

(23) Koenigsmann, C.; Wong, S. S. *Energy Environ. Sci.* **2011**, *4*, 1161.

(24) Koenigsmann, C.; Semple, D. B.; Sutter, E.; Tobierre, S. E.; Wong, S. S. *ACS Appl. Mater. Interfaces* **2013**, *5*, 5518.

(25) Zhou, W.-P.; Li, M.; Koenigsmann, C.; Ma, C.; Wong, S. S.; Adzic, R. R. *Electrochim. Acta* **2011**, *56*, 9824.

(26) Wang, S.; Wang, X.; Jiang, S. P. *Nanotechnology* **2008**, *19*, 455602.

(27) Kuchibhatla, S. V. N. T.; Karakoti, A. S.; Bera, D.; Seal, S. *Prog. Mater. Sci.* **2007**, *52*, 699.

(28) Baldauf, M.; Kolb, D. M. *J. Phys. Chem.* **1996**, *100*, 11375.

(29) Hoshi, N.; Kida, K.; Nakamura, M.; Nakada, M.; Osada, K. *J. Phys. Chem. B* **2006**, *110*, 12480.

(30) Wang, S.; Jiang, S. P.; Wang, X.; Guo, J. *Electrochim. Acta* **2011**, *56*, 1563.

(31) Van der Vliet, D. F.; Wang, C.; Tripkovic, D.; Strmcnik, D.; Zhang, X. F.; Debe, M. K.; Atanasoski, R. T.; Markovic, N. M.; Stamenkovic, V. R. *Nat. Mater.* **2012**, *11*, 1051.

(32) St. John, S.; Angelopoulos, A. P. *Electrochim. Acta* **2013**, *112*, 258.

(33) Van Hardeveld, R.; Hartog, F. *Surf. Sci.* **1969**, *15*, 189.

(34) Van Hardeveld, R.; Hartog, F. *Advan. Catal.* **1972**, *22*, 75.

(35) Shao, Y.; Yin, G.; Gao, Y. *J. Power Sources* **2007**, *171*, 558.

(36) Darling, R. M.; Meyers, J. P. *J. Electrochem. Soc.* **2003**, *150*, A1523.

(37) Darling, R. M.; Meyers, J. P. *J. Electrochem. Soc.* **2005**, *152*, A242.

(38) Borup, R.; Meyers, J.; Pivovar, B.; Kim, Y. S.; Mukundan, R.; Garland, N.; Myers, D.; Wilson, M.; Garzon, F.; Wood, D.; Zelenay, P.; More, K.; Stroh, K.; Zawodzinski, T.; Boncella, J.; McGrath, J. E.; Inaba, M.; Miyatake, K.; Hori, M.; Ota, K.; Ogumi, Z.; Miyata, S.; Nishikata, A.; Siroma, Z.; Uchimoto, Y.; Yasuda, K.; Kimijima, K.-I.; Iwashita, N. *Chem. Rev.* **2007**, *107*, 3904.

(39) Ferreira, P. J.; la O', G. J.; Shao-Horn, Y.; Morgan, D.; Makharia, R.; Kocha, S.; Gasteiger, H. A. *J. Electrochem. Soc.* **2005**, *152*, A2256.

(40) Chen, Z.; Waje, M.; Li, W.; Yan, Y. *Angew. Chem. Int. Ed. Engl.* **2007**, *46*, 4060.

(41) Alia, S. M.; Yan, Y. S.; Pivovar, B. S. *Catal. Sci. Technol.* **2014**, *4*, 3589.

(42) Bregoli, L. J. *Electrochim. Acta* **1978**, *23*, 489.

(43) Gancs, L.; Kobayashi, T.; Debe, M. K.; Atanasoski, R.; Wieckowski, A. *Chem. Mater.* **2008**, *20*, 2444.

(44) Debe, M. K.; Schmoeckel, A. K.; Vernstrom, G. D.; Atanasoski, R. *J. Power Sources* **2006**, *161*, 1002.

(45) Van der Vliet, D.; Wang, C.; Debe, M.; Atanasoski, R.; Markovic, N. M.; Stamenkovic, V. R. *Electrochim. Acta* **2011**, *56*, 8695.

(46) Alia, S. M.; Jensen, K. O.; Pivovar, B. S.; Yan, Y. *ACS Catal.* **2012**, *2*, 858.

(47) Muench, F.; Kaserer, S.; Kunz, U.; Svoboda, I.; Brötz, J.; Lauterbach, S.; Kleebe, H.-J.; Roth, C.; Ensinger, W. *J. Mater. Chem.* **2011**, *21*, 6286.

(48) Zheng, J.; Cullen, D. A.; Forest, R. V.; Wittkopf, J. A.; Zhuang, Z.; Sheng, W.; Chen, J. G.; Yan, Y. *ACS Catal.* **2015**, 1468.

(49) Guo, Y.-G.; Hu, J.-S.; Zhang, H.-M.; Liang, H.-P.; Wan, L.-J.; Bai, C.-L. *Adv. Mater.* **2005**, *17*, 746.

(50) Papandrew, A. B.; Wilson III, D. L.; M. Cantillo, N.; Hawks, S.; Atkinson, III, R. W.; Goenaga, G. A.; Zawodzinski Jr., T. A. *J. Electrochem. Soc.* **2014**, *161*, F679.

(51) Sivakumar, P.; Ishak, R.; Tricoli, V. *Electrochim. Acta* **2005**, *50*, 3312.

(52) Mercado-Zúñiga, C.; Vargas-García, J. R.; Hernández-Pérez, M. A.; Figueroa-Torres, M. Z.; Cervantes-Sodi, F.; Torres-Martínez, L. M. *J. Alloys Compd.* **2014**, *615*, S538.

(53) Papandrew, A. B.; Atkinson, III, R. W.; Unocic, R. R.; Zawodzinski, Jr., T. A. *J. Mater. Chem. A* **2015**, *3*, 3984.

(54) St. John, S.; Atkinson, III, R. W.; Unocic, R. R.; Zawodzinski, Jr., T. A.; Papandrew, A. B. *J. Phys. Chem. C* **2015**, *119*, 13481.

(55) Kinoshita, K. *J. Electrochem. Soc.* **1990**, *137*, 845.

(56) Ohyama, J.; Sato, T.; Yamamoto, Y.; Arai, S.; Satsuma, A. *J. Am. Chem. Soc.* **2013**, *135*, 8016.

(57) Zhou, W.; Lee, J. Y. *J. Phys. Chem. C* **2008**, *112*, 3789.

(58) Buffat, P.; Borel, J.-P. *Phys. Rev. A* **1976**, *13*, 2287.

(59) Zhang, M.; Efremov, M. Y.; Schiettekatte, F.; Olson, E. A.; Kwan, A. T.; Lai, S. L.; Wisleder, T.; Greene, J. E.; Allen, L. H. *Phys. Rev. B - Condens. Matter Mater. Phys.* **2000**, *62*, 10548.

(60) Law, M.; Goldberger, J.; Yang, P. *Annu. Rev. Mater. Res.* **2004**, *34*, 83.

(61) Joo, S. H.; Park, J. Y.; Renzas, J. R.; Butcher, D. R.; Huang, W.; Somorjai, G. A. *Nano Lett.* **2010**, *10*, 2709.

(62) Friedrich, K. A.; Henglein, F.; Stimming, U.; Unkauf, W. *Electrochim. Acta* **2000**, *45*, 3283.

(63) Takasu, Y.; Iwazaki, T.; Sugimoto, W.; Murakami, Y. *Electrochem. commun.* **2000**, *2*, 671.

(64) Arenz, M.; Mayrhofer, K. J. J.; Stamenkovic, V.; Blizanac, B. B.; Tomoyuki, T.; Ross, P. N.; Markovic, N. M. *J. Am. Chem. Soc.* **2005**, *127*, 6819.

(65) Maillard, F.; Savinova, E. R.; Stimming, U. *J. Electroanal. Chem.* **2007**, *599*, 221.

(66) Mayrhofer, K. J. J.; Blizanac, B. B.; Arenz, M.; Stamenkovic, V. R.; Ross, P. N.; Markovic, N. M. *J. Phys. Chem. B* **2005**, *109*, 14433.

(67) Zhou, W.; Li, M.; Ding, O. L.; Chan, S. H.; Zhang, L.; Xue, Y. *Int. J. Hydrogen Energy* **2014**, *39*, 6433.

(68) Nesselberger, M.; Ashton, S.; Meier, J. C.; Katsounaros, I.; Mayrhofer, K. J. J.; Arenz, M. *J. Am. Chem. Soc.* **2011**, *133*, 17428.

(69) Zhou, W. P.; Lewera, A.; Larsen, R.; Masel, R. I.; Bagus, P. S.; Wieckowski, A. *J. Phys. Chem. B* **2006**, *110*, 13393.

(70) Cherstiouk, O. V.; Simonov, P. A.; Savinova, E. R. *Electrochim. Acta* **2003**, *48*, 3851.

(71) Takasu, Y.; Ohashi, N.; Zhang, X.-G.; Murakami, Y.; Minagawa, H.; Sato, S.; Yahikozawa, K. *Electrochim. Acta* **1996**, *41*, 2595.

(72) Bond, G. C. *Surf. Sci.* **1985**, *156*, 966.

(73) Mayrhofer, K. J. J.; Arenz, M.; Blizanac, B. B.; Stamenkovic, V.; Ross, P. N.; Markovic, N. M. *Electrochim. Acta* **2005**, *50*, 5144.

(74) Markovic, N.; Gasteiger, H. A.; Ross, P. N. *J. Electrochem. Soc.* **1997**, *144*, 1591.

(75) Nørskov, J. K.; Rossmeisl, J.; Logadottir, A.; Lindqvist, L.; Kitchin, J. R.; Bligaard, T.; Jónsson, H.; Jonsson, H.; Jónsson, H. *J. Phys. Chem. B* **2004**, *108*, 17886.

(76) Holme, T.; Zhou, Y.; Pasquarelli, R.; O'Hayre, R. *Phys. Chem. Chem. Phys. PCCP* **2010**, *12*, 9461.

(77) Yang, Z.; Zhang, Y.; Wu, R. *J. Phys. Chem. C* **2012**.

(78) Mukerjee, S.; McBreen, J. *J. Electroanal. Chem.* **1998**, *448*, 163.

(79) Koenigsmann, C.; Zhou, W. P.; Adzic, R. R.; Sutter, E.; Wong, S. S. *Nano Lett.* **2010**, *10*, 2806.

(80) Stamenkovic, V. R.; Fowler, B.; Mun, B. S.; Wang, G.; Ross, P. N.; Lucas, C. A.; Marković, N. M. *Science (80-.).* **2007**, *315*, 493.

(81) Cherstiouk, O. V.; Simonov, P. A.; Zaikovskii, V. I.; Savinova, E. R. *J. Electroanal. Chem.* **2003**, *554-555*, 241.

(82) Friedrich, K. A.; Henglein, F.; Stimming, U.; Unkauf, W. *Electrochim. Acta* **2001**, *47*, 689.

(83) Friedrich, K. A.; Henglein, F.; Stimming, U.; Unkauf, W. *Colloids Surfaces A Physicochem. Eng. Asp.* **1998**, *134*, 193.

(84) Lu, Q.; Hutchings, G. S.; Yu, W.; Zhou, Y.; Forest, R. V.; Tao, R.; Rosen, J.; Yonemoto, B. T.; Cao, Z.; Zheng, H.; Xiao, J. Q.; Jiao, F.; Chen, J. G. *Nat. Commun.* **2015**, *6*, 6567.

(85) Wang, R.; Higgins, D. C.; Prabhudev, S.; Lee, D. U.; Choi, J.-Y.; Hoque, M. A.; Botton, G. A.; Chen, Z. *J. Mater. Chem. A* **2015**, *3*, 12663.

(86) Adzic, R. R.; Zhang, J.; Sasaki, K.; Vukmirovic, M. B.; Shao, M.; Wang, J. X.; Nilekar, A. U.; Mavrikakis, M.; Valerio, J. A.; Uribe, F. *Top. Catal.* **2007**, *46*, 249.

(87) Scofield, M. E.; Koenigsmann, C.; Wang, L.; Liu, H.; Wong, S. S. *Energy Environ. Sci.* **2014**, *8*, 350.

(88) Shui, J.; Chen, C.; Li, J. C. M. *Adv. Funct. Mater.* **2011**, *21*, 3357.

(89) Adams, B. D.; Asmussen, R. M.; Ostrom, C. K.; Chen, A. *J. Phys. Chem. C* **2014**, *118*, 29903.

(90) Liu, H.; Koenigsmann, C.; Adzic, R. R.; Wong, S. S. *ACS Catal.* **2014**, *4*, 2544.

(91) Alia, S. M.; Pivovar, B. S.; Yan, Y. *J. Am. Chem. Soc.* **2013**, *135*, 13473.

(92) Alia, S. M.; Larsen, B. A.; Pylypenko, S.; Cullen, D. A.; Diercks, D. R.; Neyerlin, K. C.; Kocha, S. S.; Pivovar, B. S. *ACS Catal.* **2014**, *4*, 1114.

(93) Alia, S. M.; Pylypenko, S.; Neyerlin, K. C.; Cullen, D. A.; Kocha, S. S.; Pivovar, B. S. **2014**.

(94) Zheng, J. P.; Cygan, P. J.; Jow, T. R. *J. Electrochem. Soc.* **1995**, *142*, 2699.

(95) Long, J. W.; Stroud, R. M.; Swider-Lyons, K. E.; Rolison, D. R. *J. Phys. Chem. B* **2000**, *104*, 9772.

(96) Roen, L. M.; Paik, C. H.; Jarvi, T. D. *Electrochem. Solid-State Lett.* **2004**, *7*, A19.

(97) Kocha, S. S.; Zack, J. W.; Alia, S. M.; Neyerlin, K. C.; Pivovar, B. S. *ECS Trans.* **2012**, *50*, 1475.

(98) Debe, M. K. *ECS Trans.* **2012**, *45*, 47.

(99) Debe, M. K. *J. Electrochem. Soc.* **2012**, *159*, B53.

(100) Debe, M. K.; Steinbach, A. J. *ECS Trans.* **2007**, *11*, 659.

(101) Alia, S. M.; Zhang, G.; Kisailus, D.; Li, D.; Gu, S.; Jensen, K.; Yan, Y. *Adv. Funct. Mater.* **2010**, *20*, 3742.

(102) Kibsgaard, J.; Gorlin, Y.; Chen, Z.; Jaramillo, T. F. *J. Am. Chem. Soc.* **2012**, *134*, 7758.

(103) V. R. Philips Analytical B. V. “Philips X’pert Highscore Plus,” 1999.

(104) Garsany, Y.; Baturina, O. A.; Swider-Lyons, K. E.; Kocha, S. S. *Anal. Chem.* **2010**, *82*, 6321.

(105) Kocha, S. S. In *Handbook of Fuel Cells*; Vielstich, W.; Lamm, A.; Gasteiger, H. A., Eds.; John Wiley & Sons, Ltd, 2003; p. 538.

(106) Papandrew, A. B.; Chisholm, C. R. I.; Elgammal, R. A.; Özer, M. M.; Zecevic, S. K. *Chem. Mater.* **2011**, *23*, 1659.

(107) Subbaraman, R.; Strmcnik, D.; Paulikas, A. P.; Stamenkovic, V. R.; Markovic, N. M. *ChemPhysChem* **2010**, *11*, 2825.

(108) Papandrew, A. B.; Atkinson, R. W.; Goenaga, G. A.; Wilson, D. L.; Kocha, S. S.; Neyerlin, K. C.; Zack, J.; Pivovar, B. S.; Zawodzinski, T. A. *ECS Trans.* **2012**, *50*, 1397.

(109) Ji, C.; Searson, P. C. *Appl. Phys. Lett.* **2002**, *81*, 4437.

(110) Garbarino, S.; Ponrouch, A.; Pronovost, S.; Gaudet, J.; Guay, D. *Electrochem. commun.* **2009**, *11*, 1924.

(111) Koenigsmann, C.; Scofield, M. E.; Liu, H.; Wong, S. S. *J. Phys. Chem. Lett.* **2012**, *3*, 3385.

(112) Sun, Y.; Xia, Y. *Adv. Mater.* **2003**, *15*, 695.

(113) Leskelä, M.; Ritala, M. *Angew. Chemie* **2003**, *42*, 5548.

(114) Narayanan, R.; El-Sayed, M. A. *J. Phys. Chem. B* **2005**, *109*, 12663.

(115) Borodko, Y.; Habas, S. E.; Koebel, M.; Yang, P.; Frei, H.; Somorjai, G. A. *J. Phys. Chem. B* **2006**, *110*, 23052.

(116) Yang, H.; Tang, Y.; Zou, S. *Electrochem. commun.* **2014**, *38*, 134.

(117) Papandrew, A. B.; Atkinson, III, R. W.; Goenaga, G. A.; Kocha, S. S.; Zack, J. W.; Pivovar, B. S.; Zawodzinski Jr., T. A. *J. Electrochem. Soc.* **2013**, *160*, F848.

(118) Gasteiger, H. A.; Markovic, N.; Ross Jr., P. N.; Cairns, E. J. *J. Phys. Chem.* **1993**, *97*, 12020.

(119) Gilman, S. *J. Phys. Chem.* **1964**, *68*, 70.

(120) McCallum, C.; Pletcher, D. *J. Electroanal. Chem.* **1976**, *70*, 277.

(121) Love, B.; Lipkowski, J. *ACS Symp. Ser.* **1988**, 484.

(122) Petukhov, A. V.; Akemann, W.; Friedrich, K. A.; Stimming, U. *Surf. Sci.* **1998**, *402-404*, 182.

(123) Watanabe, M.; Motoo, S. *Electroanal. Chem. Interfacial Electrochem.* **1975**, *60*, 267.

(124) Gasteiger, H. A.; Markovic, N.; Ross Jr., P. N.; Cairns, E. J. *J. Phys. Chem.* **1994**, *98*, 617.

(125) Ticanelli, E.; Beery, J. G.; Paffett, M. T.; Gottesfeld, S. *J. Electroanal. Chem. Interfacial Electrochem.* **1989**, *258*, 61.

(126) Scott, F. J.; Mukerjee, S.; Ramaker, D. E. *J. Phys. Chem. C* **2010**, *114*, 442.

(127) Hadzi-Jordanov, S.; Angerstein-Kozlowska, H.; Vukovic, M.; Conway, B. E. *J. Phys. Chem.* **1977**, *81*, 2271.

(128) Shao, M.; Odell, J. H.; Choi, S.-I.; Xia, Y. *Electrochem. commun.* **2013**, *31*, 46.

(129) Rolison, D. R.; Hagans, P. L.; Swider, K. E.; Long, J. W. *Langmuir* **1999**, *15*, 774.

(130) Hamel, C.; Garbarino, S.; Irissou, E.; Bichat, M.-P.; Guay, D. *J. Phys. Chem. C* **2010**, *114*, 18931.

(131) McKeown, D. A.; Hagans, P. L.; Carette, L. P. L.; Russell, A. E.; Swider, K. E.; Rolison, D. R. *J. Phys. Chem. B* **1999**, *103*, 4825.

(132) Stoupin, S.; Chung, E. H.; Chattopadhyay, S.; Segre, C. U.; Smotkin, E. S. *J. Phys. Chem. B* **2006**, *110*, 9932.

(133) Ma, J.-H.; Feng, Y.-Y.; Yu, J.; Zhao, D.; Wang, A.-J.; Xu, B.-Q. *J. Catal.* **2010**, *275*, 34.

(134) Godoi, D. R.; Perez, J.; Villullas, H. M. *J. Phys. Chem. C* **2009**, *113*, 8518.

(135) Park, Y.-K.; Kim, T.-H.; Park, S. *J. Mater. Chem.* **2010**, *20*, 3637.

(136) Rice, C.; Ha, S.; Masel, R. I.; Wieckowski, A. *J. Power Sources* **2003**, *115*, 229.

(137) Capon, A.; Parsons, R. *Electroanal. Chem. Interfacial Electrochem.* **1973**, *45*, 205.

(138) Peng, B.; Wang, H.-F.; Liu, Z.-P.; Cai, W.-B. *J. Phys. Chem. C* **2010**, *114*, 3102.

(139) Bauskar, A. S.; Rice, C. A. *Electrochim. Acta* **2013**, *93*, 152.

(140) Llorca, M. J.; Feliu, J. M.; Aldaz, A.; Clavilier, J. *J. Electroanal. Chem.* **1994**, *376*, 151.

(141) Babu, P. K.; Kim, H. S.; Chung, J. H.; Oldfield, E.; Wieckowski, A. *J. Phys. Chem. B* **2004**, *108*, 20228.

(142) Pan, Y.; Zhang, R.; Blair, S. L. *Electrochem. Solid-State Lett.* **2009**, *12*, B23.

(143) Perales-Rondón, J. V.; Herrero, E.; Feliu, J. M. *J. Electroanal. Chem.* **2015**, *742*, 90.

(144) Wang, X.; Tang, Y.; Gao, Y.; Lu, T. *J. Power Sources* **2008**, *175*, 784.

(145) Morales-Acosta, D.; Ledesma-Garcia, J.; Godinez, L. A.; Rodríguez, H. G.; Álvarez-Contreras, L.; Arriaga, L. G. *J. Power Sources* **2010**, *195*, 461.

(146) Mazumder, V.; Chi, M.; Mankin, M. N.; Liu, Y.; Metin, O.; Sun, D.; More, K. L.; Sun, S. *Nano Lett.* **2012**, *12*, 1102.

(147) Fae Ho, S.; Mendoza-Garcia, A.; Guo, S.; He, K.; Su, D.; Liu, S.; Metin, O.; Sun, S. *Nanoscale* **2014**, *6*, 6970.

(148) Ren, M.; Zhou, Y.; Tao, F.; Zou, Z.; Akins, D. L.; Yang, H. *J. Phys. Chem. C* **2014**, *118*, 12669.

(149) Matin, M. A.; Jang, J.-H.; Kwon, Y.-U. *J. Power Sources* **2014**, *262*, 356.

(150) Sun, D.; Si, L.; Fu, G.; Liu, C.; Sun, D.; Chen, Y.; Tang, Y.; Lu, T. *J. Power Sources* **2015**, *280*, 141.

(151) Leiva, E.; Iwasita, T.; Herrero, E.; Feliu, J. M. *Langmuir* **1997**, *7463*, 6287.

(152) Bauskar, A. S.; Rice, C. A. *Electrochim. Acta* **2013**, *107*, 562.

(153) Perales-Rondón, J. V.; Ferre-Vilaplana, A.; Feliu, J. M.; Herrero, E. *J. Am. Chem. Soc.* **2014**, *136*, 13110.

(154) Ferre-Vilaplana, A.; Perales-Rondón, J. V.; Feliu, J. M.; Herrero, E. *ACS Catal.* **2015**, *5*, 645.

(155) Busó-Rogero, C.; Perales-Rondón, J. V; Farias, M. J. S.; Vidal-Iglesias, F. J.; Solla-Gullon, J.; Herrero, E.; Feliu, J. M. *Phys. Chem. Chem. Phys.* **2014**, *16*, 13616.

(156) Cuesta, A. *ChemPhysChem* **2011**, *12*, 2375.

(157) Cuesta, A.; Escudero, M.; Lanova, B.; Baltruschat, H. *Langmuir* **2009**, *25*, 6500.

(158) Neurock, M.; Janik, M.; Wieckowski, A. *Faraday Discuss.* **2008**, *140*, 363.

(159) Neurock, M.; Janik, M.; Wieckowski, A. *Faraday Discuss.* **2009**, *140*, 363.

(160) Wang, H.-F.; Liu, Z.-P. *J. Phys. Chem. C* **2009**, *113*, 17502.

(161) Herron, J. A.; Scaranto, J.; Ferrin, P.; Li, S.; Mavrikakis, M. *ACS Catal.* **2014**, *4*, 4434.

(162) Steinmann, S. N.; Michel, C.; Schwiedernoch, R.; Filhol, J.-S.; Sautet, P. *ChemPhysChem* **2015**, DOI: 10.1002/cphc.201500187.

(163) Komanicky, V.; Chang, K. C.; Menzel, A.; Markovic, N. M.; You, H.; Wang, X.; Myers, D. *J. Electrochem. Soc.* **2006**, *153*, B446.

(164) Atkinson, III, R. W.; Unocic, R. R.; Unocic, K. A.; Veith, G. M.; Zawodzinski, Jr., T. A.; Papandrew, A. B. *ACS Appl. Mater. Interfaces* **2015**, *7*, 10115.

(165) Ravel, B. *EXAFS Analysis with FEFF and FEFFIT*; University of Washington, 2001; Vol. 2.

(166) Vidaković, T.; Christov, M.; Sundmacher, K. *Electrochim. Acta* **2007**, *52*, 5606.

(167) Clavilier, J.; Feliu, J. M.; Aldaz, A. *J. Electroanal. Chem. Interfacial Electrochem.* **1988**, *243*, 419.

(168) Rodríguez, P.; Solla-Gullón, J.; Vidal-Iglesias, F. J.; Herrero, E.; Aldaz, A.; Feliu, J. M. *Anal. Chem.* **2005**, *77*, 5317.

(169) Rodríguez, P.; Herrero, E.; Solla-Gullón, J.; Vidal-Iglesias, F. J.; Aldaz, A.; Feliu, J. M. *Electrochim. Acta* **2005**, *50*, 4308.

(170) Solla-Gullón, J.; Rodríguez, P.; Herrero, E.; Aldaz, A.; Feliu, J. M. *Phys. Chem. Chem. Phys.* **2008**, *10*, 1359.

(171) Ziemecki, S. B.; Jones, G. A.; Swartzfager, D. G.; Harlow, R. L.; Faber, Jr., J. *J. Am. Chem. Soc.* **1985**, *107*, 4547.

(172) McCaulley, J. A. *Phys. Rev. B* **1993**, *47*, 4873.

(173) McCaulley, J. A. *J. Phys. Chem.* **1993**, *97*, 10372.

(174) Papandrew, A. B.; Chisholm, C. R. I.; Zecevic, S. K.; Veith, G. M.; Zawodzinski, T. A. *J. Electrochem. Soc.* **2013**, *160*, F175.

(175) Harada, M.; Asakura, K.; Ueki, Y.; Toshima, N. *J. Phys. Chem.* **1992**, *96*, 9730.

(176) Urchaga, P.; Baranton, S.; Coutanceau, C.; Jerkiewicz, G. *Langmuir* **2012**, *28*, 3658.

(177) Tateishi, N.; Yahikozawa, K.; Nishimura, K.; Suzuki, M.; Iwanaga, Y.; Watanabe, M.; Enami, E.; Matsuda, Y.; Takasu, Y. *Electrochim. Acta* **1991**, *36*, 1235.

(178) Nag, N. K. *J. Phys. Chem. B* **2001**, *105*, 5945.

(179) Jerkiewicz, G.; Zolfaghari, A. *J. Electrochem. Soc.* **1996**, *143*, 1240.

(180) Grdeń, M.; Łukaszewski, M.; Jerkiewicz, G.; Czerwiński, A. *Electrochim. Acta* **2008**, *53*, 7583.

(181) Kim, B.-J.; Kwon, K.; Rhee, C. K.; Han, J.; Lim, T.-H. *Electrochim. Acta* **2008**, *53*, 7744.

(182) Parsons, R.; VanderNoot, T. *J. Electroanal. Chem. Interfacial Electrochem.* **1988**, *257*, 9.

(183) Vidal-Iglesias, F. J.; Arán-Ais, R. M.; Solla-Gullón, J.; Garnier, E.; Herrero, E.; Aldaz, A.; Feliu, J. M. *Phys. Chem. Chem. Phys.* **2012**, *14*, 10258.

(184) Figueiredo, M. C.; Solla-Gullón, J.; Vidal-Iglesias, F. J.; Nisula, M.; Feliu, J. M.; Kallio, T. *Electrochem. commun.* **2015**, *55*, 47.

(185) Bertin, E.; Garbarino, S.; Guay, D.; Solla-Gullón, J.; Vidal-Iglesias, F. J.; Feliu, J. M. *J. Power Sources* **2013**, *225*, 323.

(186) Miyake, H.; Hosono, E.; Osawa, M.; Okada, T. *Chem. Phys. Lett.* **2006**, *428*, 451.

(187) Capon, A.; Parsons, R. *Electroanal. Chem. Interfacial Electrochem.* **1973**, *44*, 239.

(188) Blizanac, B. B.; Ross, P. N.; Marković, N. M. *J. Phys. Chem. B* **2006**, *110*, 4735.

(189) St. John, S.; Atkinson III, R. W.; Unocic, R. R.; Papandrew, A. B.; Zawodzinski Jr., T. A. *J. Phys. Chem. C* **2015**.

(190) Strmcnik, D.; Uchimura, M.; Wang, C.; Subbaraman, R.; Danilovic, N.; van der Vliet, D.; Paulikas, A. P.; Stamenkovic, V. R.; Markovic, N. M. *Nat. Chem.* **2013**, *5*, 300.

(191) Durst, J.; Siebel, a; Simon, C.; Hasche, F.; Herranz, J.; Gasteiger, H. A. *Energy Environ. Sci.* **2014**, *7*, 2255.

(192) Krischer, K.; Savinova, E. R. In *Handbook of Heterogeneous Catalysis*; Wiley-VCH Verlag GmbH & Co. KGaA, 2008.

(193) Spendelow, J. S.; Lu, G. Q.; Kenis, P. J. A.; Wieckowski, A. *J. Electroanal. Chem.* **2004**, *568*, 215.

(194) Zhang, J.; Vukmirovic, M. B.; Sasaki, K.; Nilekar, A. U.; Mavrikakis, M.; Adzic, R. R. *J. Am. Chem. Soc.* **2005**, *127*, 12480.

(195) Zhang, J.; Mo, Y.; Vukmirovic, M. B.; Klie, R.; Sasaki, K.; Adzic, R. R. *J. Phys. Chem. B* **2004**, *108*, 10955.

(196) Duan, Z.; Wang, G. *J. Phys. Chem. C* **2013**.

(197) Greeley, J.; Jaramillo, T. F.; Bonde, J.; Chorkendorff, I.; Nørskov, J. K. *Nat. Mater.* **2006**, *5*, 909.

(198) Yamada, Y.; Miyamoto, K.; Hayashi, T.; Iijima, Y.; Todoroki, N.; Wadayama, T. *Surf. Sci.* **2013**, *607*, 54.

(199) Wadayama, T.; Yoshida, H.; Ogawa, K.; Todoroki, N.; Yamada, Y.; Miyamoto, K.; Iijima, Y.; Sugawara, T.; Arihara, K.; Sugawara, S.; Shinohara, K. *J. Phys. Chem. C* **2011**, *115*, 18589.

(200) Zhou, W. P.; Axnanda, S.; White, M. G.; Adzic, R. R.; Hrbek, J. *J. Phys. Chem. C* **2011**, *115*, 16467.

(201) Zheng, Q. W.; Fan, C. J.; Zhen, C. H.; Zhou, Z. Y.; Sun, S. G. *Electrochim. Acta* **2008**, *53*, 6081.

(202) Spendelow, J. S.; Babu, P. K.; Wieckowski, A. *Curr. Opin. Solid State Mater. Sci.* **2005**, *9*, 37.

(203) Zhang, J.; Lima, F. H. B.; Shao, M. H.; Sasaki, K.; Wang, J. X.; Hanson, J.; Adzic, R. R. *J. Phys. Chem. B* **2005**, *109*, 22701.

(204) Han, B.; Carlton, C. E.; Kongkanand, A.; Kukreja, R. S.; Theobald, B. R.; Gan, L.; O'Malley, R.; Strasser, P.; Wagner, F. T.; Shao-Horn, Y. *Energy Environ. Sci.* **2015**.

(205) St. John, S.; Boolchand, P.; Angelopoulos, A. P. *Langmuir* **2013**, *29*, 16150.

(206) Atkinson, III, R. W.; Papandrew, A. B.; Zawodzinski Jr., T. A. *ECS Meet. Abstr.* **2013**, Abstract #1246.

(207) Rehr, J. J.; Kas, J. J.; Vila, F. D.; Prange, M. P.; Jorissen, K. *Phys. Chem. Chem. Phys.* **2010**, *12*, 5503.

(208) Ravel, B. *Crystallography for the X-ray Absorption Spectroscopist*; University of Chicago, 2002.

(209) Gasteiger, H. A.; Ross Jr., P. N.; Cairns, E. J. *Surf. Sci.* **1993**, *293*, 67.

(210) Strohl, J. K.; King, T. S. *J. Catal.* **1989**, *118*, 53.

(211) Tyson, W. R.; Miller, W. A. *Surf. Sci.* **1977**, *62*, 267.

(212) Gelatt, C. D.; Ehrenreich, H.; Weiss, J. A. *Phys. Rev. B* **1978**, *17*, 1940.

(213) Mansour, A. N.; Cook Jr, J. W.; Sayers, D. E. *J. Phys. Chem.* **1984**, *88*, 2330.

(214) Mansour, A. N.; Cook, J. W.; Sayers, D. E.; Emrich, R. J.; Katzer, J. R. *J. Catal.* **1984**, *89*, 462.

(215) Shao, M. H.; Huang, T.; Liu, P.; Zhang, J.; Sasaki, K.; Vukmirovic, M. B.; Adzic, R. R. *Langmuir* **2006**, *22*, 10409.

(216) Frenkel, A. I.; Small, M. W.; Smith, J. G.; Nuzzo, R. G.; Kvashnina, K. O.; Tromp, M. *J. Phys. Chem. C* **2013**, *117*, 23286.

(217) Wanjala, B. N.; Loukrakpam, R.; Luo, J.; Njoki, P. N.; Mott, D.; Zhong, C.-J.; Shao, M.; Protsailo, L.; Kawamura, T. *J. Phys. Chem. C* **2010**, *114*, 17580.

(218) Sasaki, K.; Mo, Y.; Wang, J. X.; Balasubramanian, M.; Uribe, F.; McBreen, J.; Adzic, R. R. *Electrochim. Acta* **2003**, *48*, 3841.

(219) Sheng, W.; Myint, M.; Chen, J. G.; Yan, Y. *Energy Environ. Sci.* **2013**, *6*, 1509.

(220) Bard, A. J.; Faulkner, L. R. *Electrochemical methods: fundamentals and applications*; Wiley: New York, NY, 2006.

(221) Skulason, E.; Tripkovic, V.; Bjorketun, M. E.; Gudmundsdottir, S.; Karlberg, G.; Rossmeisl, J.; Bligaard, T.; Jonsson, H.; Norskov, J. K.; Skúlason, E.; Tripkovic, V.; Björketun, M. E.; Gudmundsdóttir, S.; Karlberg, G.; Rossmeisl, J.; Bligaard, T.; Jónsson, H.; Nørskov, J. K. *J. Phys. Chem. C* **2010**, *114*, 18182.

(222) Shao, M.; Liu, P.; Zhang, J.; Adzic, R. *J. Phys. Chem. B* **2007**, *111*, 6772.

(223) Jiang, L.; Hsu, A.; Chu, D.; Chen, R. *J. Electrochem. Soc.* **2009**, *156*, B370.

(224) Stamenkovic, V.; Mun, B. S.; Mayrhofer, K. J. J.; Ross, P. N.; Markovic, N. M.; Rossmeisl, J.; Greeley, J.; Nørskov, J. K. *Angew. Chemie - Int. Ed.* **2006**, *45*, 2897.

(225) Lima, F. H. B.; Zhang, J.; Shao, M. H.; Sasaki, K.; Vukmirovic, M. B.; Ticianelli, E. A.; Adzic, R. R. *J. Phys. Chem. C* **2006**, *111*, 404.

(226) Ruban, A.; Hammer, B.; Stoltze, P.; Skriver, H. L.; Nørskov, J. K. *J. Mol. Catal. A Chem.* **1997**, *115*, 421.

(227) Hammer, B.; Nørskov, J. K. *Surf. Sci.* **1995**, *343*, 211.

(228) Subbaraman, R.; Zawodzinski Jr., T.; Mann Jr., J. A. *Langmuir* **2008**, *24*, 8245.

(229) Rajter, R.; French, R. H. *Int. J. Mater. Res.* **2010**, *101*, 27.

(230) Parsegian, V. A.; Weiss, G. H. *J. Colloid Interface Sci.* **1981**, *81*, 285.

(231) Parsegian, V. A. *van der Waals Forces: a handbook for biologists, chemists, engineers, and physicists*; Cambridge University Press: New York, 2006.

(232) Lucarini, V.; Saarinen, J. J.; Peiponen, K.-E.; Vartiainen, E. M. Kramers-Kronig relations in optical materials research, 2005.

(233) Rajter, R. F.; French, R. H.; Ching, W. Y.; Carter, W. C.; Chiang, Y. M. *J. Appl. Phys.* **2007**, *101*, 17.

(234) Ordal, M. A.; Long, L. L.; Bell, R. J. R.; Bell, S. E.; Bell, R. J. R.; Alexander, R. W.; Ward, C. A. *Appl. Opt.* **1983**, *22*, 1099.

(235) Lide, D. R. CRC Handbook of Chemistry and Physics, 2002.

(236) Montgomery, S. W.; Franchek, M. A.; Goldschmidt, V. W. *J. Colloid Interface Sci.* **2000**, *227*, 567.

(237) Langbein, D. *Phys. der Kondens. Mater.* **1972**, *15*, 61.

(238) Ackler, H. D.; French, R. H.; Chiang, Y. M. *J. Colloid Interface Sci.* **1996**, *179*, 460.

(239) Dagastine, R. R.; Prieve, D. C.; White, L. R. *J. Colloid Interface Sci.* **2000**, *231*, 351.

(240) Garsany, Y.; Singer, I. L.; Swider-Lyons, K. E. *J. Electroanal. Chem.* **2011**, *662*, 396.

(241) Gasteiger, H. A.; Kocha, S. S.; Sompalli, B.; Wagner, F. T. *Appl. Catal. B Environ.* **2005**, *56*, 9.

(242) Takahashi, I.; Kocha, S. S. *J. Power Sources* **2010**, *195*, 6312.

(243) Galbiati, S.; Morin, A.; Pauc, N. *Electrochim. Acta* **2014**, *125*, 107.

(244) Debe, M. K. *ECS Trans.* **2013**, *160*, F522.

(245) Sharma, S.; Pollet, B. G. *J. Power Sources* **2012**, *208*, 96.

APPENDIX

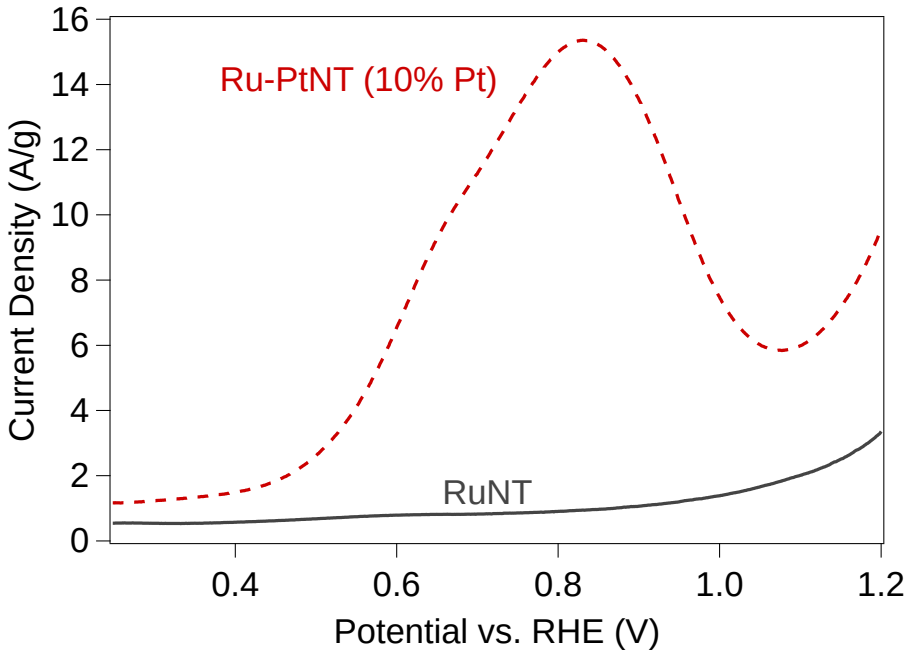

Figure A.1. Linear sweep voltammograms recorded in 0.5 M CH_3OH and 0.1 M H_2SO_4 at 20 mV s^{-1}.

Pure RuNTs (black) are not active for methanol oxidation but adding small amounts of Pt to the interior of these annealed, metallic RuNTs (Ru-PtNT, 10% Pt) leads to a considerable improvement in MOR activity. The Ru-PtNTs were prepared by annealing RuNTs at 500°C before depositing Pt and dissolving the templates without annealing. This allows for the synthesis of non-alloyed, discretely layered, bi-metallic nanotubes with Ru at the exteriors and Pt at the interiors. The increase in methanol oxidation activity demonstrated in Figure A1 for the nanotubes with Pt only at the interior indicates that there is sufficient reactant diffusion to the nanotube interior and that the nanotube interiors provide active sites for catalysis.

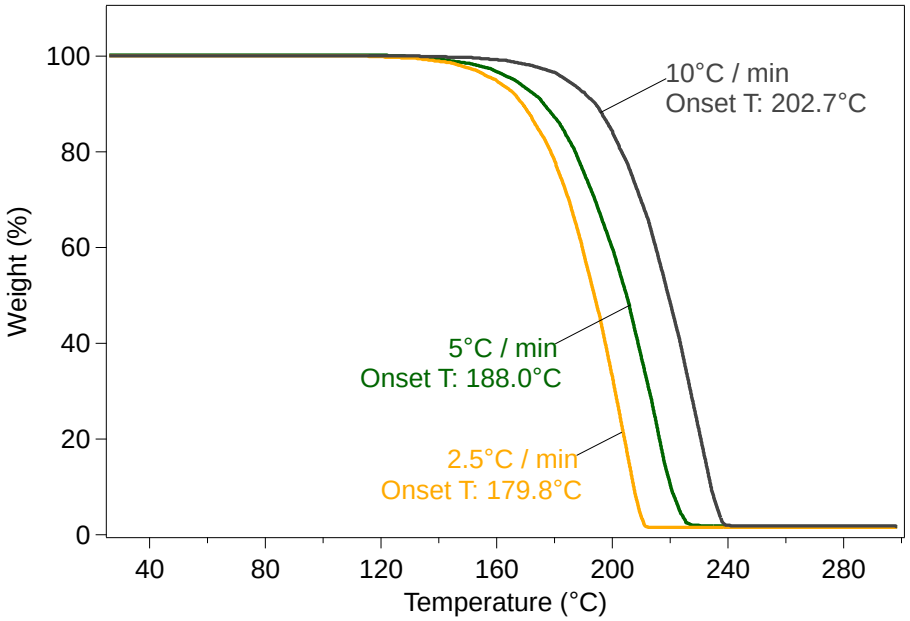

Figure A.2. TGA profiles as a function of temperature ramp rate of platinum(II)-2,4-pentanedionate, Pt-$(acac)_2$.

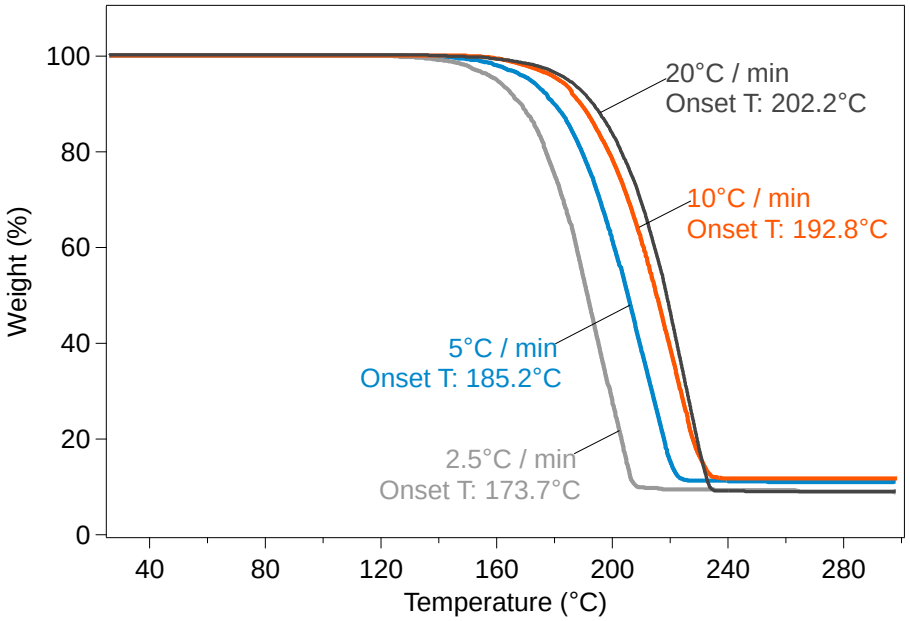

Figure A.3. TGA profiles as a function of temperature ramp rate of palladium(II)-2,4-pentanedionate, Pd-$(acac)_2$.

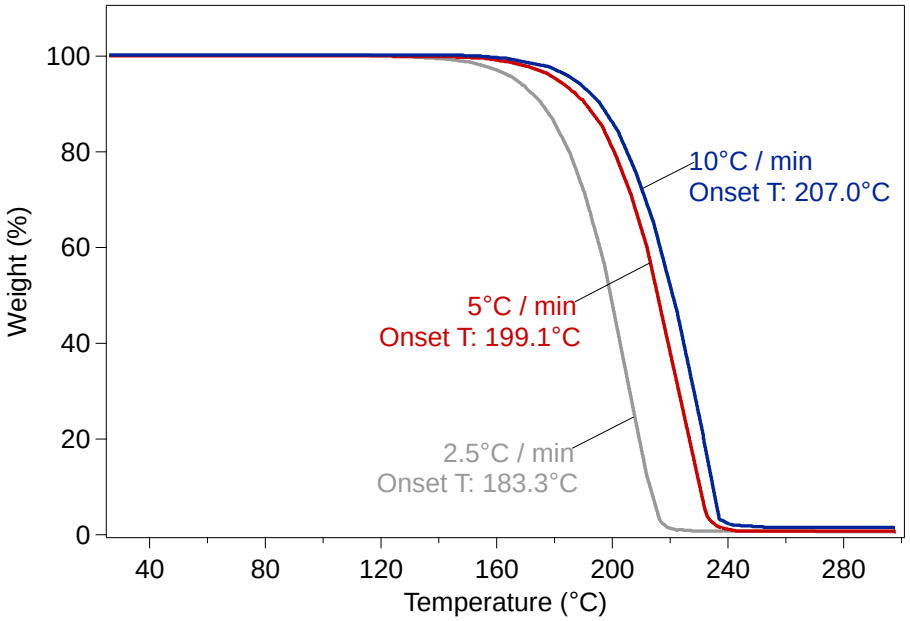

Figure A.4. TGA profiles as a function of temperature ramp rate of ruthenium(III)-2,4-pentanedionate, Ru-(acac)$_3$.

VITA

Robert W. Atkinson III grew up in Manteo, North Carolina. He enrolled at Wake Forest University in Winston-Salem, NC in 2006. As an undergraduate student, Rob conducted research with Professor Timo Thonhauser before graduating with a Bachelor of Science degree in Chemistry in 2010. That year Rob joined the Department of Chemical and Biomolecular Engineering at The University of Tennessee, Knoxville as a graduate student. He worked in the research group of Governor's Chair Professor Thomas Zawodzinski, where he was co-advised by Professor Alexander Papandrew.